Facile synthesis of Ag/AgCl/BiOCl composite Z-scheme photocatalyst for visible – light – driven pollutant removal

Dorcas Oluyemisi Adenuga

Facile synthesis of Ag/AgCl/BiOCl composite Z-scheme photocatalyst for visible – light – driven pollutant removal

By

Dorcas Oluyemisi Adenuga

Submitted in partial fulfilment of the requirements for the degree

Master of Engineering (Chemical Engineering)

In the

Department of Chemical Engineering
Faculty of Engineering, Built Environment and Information Technology

University of Pretoria

2019

ABSTRACT

Title: **Facile synthesis of Ag/AgCl/BiOCl composite Z-scheme photocatalyst for visible – light – driven pollutant removal**

Author: Dorcas Oluyemisi Adenuga
Supervisor: Professor Evans M.N. Chirwa
Co-supervisor: Dr Shepherd M. Tichapondwa
Department: Chemical Engineering
University: University of Pretoria
Degree: Master of Engineering (Chemical Engineering)

Degradation of organic contaminants in wastewaters emanating from industrial processing plants could render the water streams reusable for the purpose of reducing water consumption while protecting the environment from harmful pollutants. Organic pollutants can be removed from water using biological processes that mineralise the organics to H_2O and CO_2. However, mineralisation by biological processes take a long time and in many cases, total mineralisation is impossible to achieve. Alternatively, organics can be completely degraded and mineralised rapidly using chemical and/or photocatalytic advanced oxidation processes (AOP). Both systems have some short comings. In chemical AOP such as Fenton and photo-Fenton reagents, the chemical agents used remain in the water as pollutants requiring further removal. In photocatalytic oxidation processes, most current technologies use UV light as an energy source. The chemical processes are environmentally incompatible, whereas, the “green” photocatalysis is extremely expensive due to the consumption of electricity by high pressure UV light.

Forerunner investigators of photocatalysis utilised TiO_2 as the photocatalyst of choice. It has major drawbacks of which the most important one is that it is only activated under ultraviolet (UV) light irradiation. This high energy consumption made the process practically unfeasible. Solar energy (natural light and heat from sun) has great prospects with regards to acting as a substitute for UV since it is a renewable and

cheaper energy source. This work therefore investigated the development of a heterogeneous all-solid-state Z-scheme silver/ silver chloride/ bismuth oxychloride (Ag/AgCl/BiOCl) photocatalyst that is able to utilise natural light through being activated by visible light irradiation. This will successfully serve as a green alternative in the use of renewable energy for pollution reduction while saving energy.

The synthesised photocatalysts were characterised using various techniques. The purity and crystallinity of the synthesised photocatalysts were determined using x-ray diffraction (XRD) while x-ray photoelectron spectroscopy (XPS) was used to determine the elemental composition and chemical states present in the synthesised catalysts as well as confirm the presence of elemental Ag. Fourier-transform infrared spectroscopy (FTIR) specified the functional groups present while the morphology and chemical composition were determined on a scanning electron microscopy (SEM)/ energy dispersive x-ray spectroscopy (EDS). The surface area and pore size were measured on a Brunauer-Emmett-Teller (BET) and thermogravimetric analysis (TGA) was done to determine the thermal degradation of synthesised particles. Ultraviolet-visible spectroscopy (UV-VIS) was done to determine the photoabsorption range and bandgap of the particles as efficiency of photocatalysis is dependent on the properties and morphology of the semiconductor material.

Degradation studies were carried out under both visible and UV light irradiation in a batch reactor. The activity of the synthesised Ag/AgCl/BiOCl photocatalyst was compared to that of commonly used TiO_2. Specifically, while 60% degradation was achieved under UV light irradiation by both TiO_2 and Ag/AgCl/BiOCl photocatalyst, in visible light irradiation, TiO_2 measures only 14% in 4 h while Ag/AgCl/BiOCl measures a photodegradation efficiency of 53%. Other factors such as initial organic contaminants concentration, initial catalyst concentration, pH effects and individual compounds effect were also investigated. The reusability of the catalyst was also reported showing stability of the synthesised catalyst as after a total irradiation time of 48 h, 65% phenol degradation was measured. The phenol degradation kinetics were found to fit the widely used first-order Langmuir-Hinshelwood model.

The result from the current study proves the feasibility of a novel process for mineralisation of organic compounds in water under cost effective visible light irradiation for the removal of recalcitrant and refractory organics from water.

Keywords: degradation, organic, phenol, photocatalysis, pollutants, visible light.

DECLARATION

I, Dorcas Oluyemisi Adenuga, hereby declare that all the work provided in this dissertation is to the best of my knowledge original and that neither the whole work nor any part of it has been, or is to be submitted for another degree at this or any other University or tertiary education institution or examining body.

Signature: …… DATE: …….

DEDICATION

To my parents

Kayode and Olusola Adenuga

For their sacrifice of love and support

and

To my siblings

Adeniyi, Oluwatosin and Oluwaseyi

For always believing in me and being my biggest cheerleaders.

ACKNOWLEDGEMENT

I am of immense gratitude to my supervisor, Prof Evans Chirwa for accepting me into his research group and giving me the opportunity to carry out my research under his expertise. His words of encouragement, his absolute faith in my capabilities and supervision enabled me to achieve this milestone and I am grateful. I also want to thank him for securing the Sedibeng funding which enabled me to carry out my work. I am grateful to Dr Tichapondwa for co-supervising this project, always opening his door every time I came knocking. I appreciate his efforts, guidance and dedication to my project and ensuring good quality work is done.

I would like to appreciate the National Research Foundation South Africa for my Masters Innovation scholarship. Thanks to the staff and colleagues of the Water Utilization Division at the University of Pretoria for ensuring an enabling environment to work while always willing to give a helping hand. Special mention to Mrs Alette Devega and Mrs Elmerie Otto for always helping out.

I am thankful to Dr Zakhele Khuzwayo and Mr John Njalamanno for the HPLC training given to me for my phenol analysis. I appreciate the staff at the SEM, and XRD units at the University of Pretoria. Thanks to Titus for the TGA analysis, Zhonga and Leila for the BET analysis, NMISA for the XPS analysis and Anya for the FTIR and UV-VIS analysis. I also fully acknowledge my vacation work students, Andries and Lindie for the good work.

I am of utmost gratitude to my friends who walked this journey with me, a difficult journey but the load was made lighter with their presence. To the community and family that surrounds me, thank you. I acknowledge the village of people that has contributed to my studies and have enabled me to reach this potential, I am grateful for your labour of love and prayers.

Finally, I will like to thank the Lord Almighty, my unwavering beacon of hope in the midst of life storms, for giving me this opportunity.

Table of Contents

LIST OF FIGURES

LIST OF TABLES

LIST OF SCHEMES

LIST OF NOMENCLATURE

ADP	Adenosine diphosphate
ATP	Adenosine triphosphate
AOP	Advanced Oxidation Processes
BET	Brunauer-Emmett-Teller
BiOCl	Bismuth oxychloride
CB	Conduction band
CTAC	Cetyltrimethylammonium chloride
EDC	Endocrine disrupting chemical
EDS	Energy dispersive X-ray spectroscopy
E_g	Bandgap energy
FTIR	Fourier-transform infrared spectroscopy
GC	Gas chromatography
h_{vb+}	Valence band hole
HDD	Hydrodynamic diameter
HPLC	High Pressure Liquid Chromatography
$NADP^+$	Nicotinamide adenine dinucleotide phosphate
NADPH	Reduced nicotinamide adenine dinucleotide phosphate
PPM	Parts per million
SEM	Scanning electron microscope
SPR	Surface plasmon resonance
TEM	Transmission electron microscope
TiO_2	Titanium dioxide
TGA	Thermogravimetric analysis
TOC	Total Organic Carbon
USEPA	United States Environmental Protection Agency
UV	Ultraviolet
UV-Vis	Ultraviolet-visible spectrometry
VB	Valence band
WHO	World Health Organisation
XRD	X-ray powder diffraction
XRF	X-ray fluorescence
XPS	X-ray photoelectron spectroscopy

a	absorption coefficient
Ct	Concentration of phenol at time t
C_0	Initial phenol concentration
h	Plank constant
t	Reaction time
v	Light frequency
e^-	Valence band electron
h^+	Conduction band hole
eV	Electron volt
nm	Nanometers
mg/L	Milligrams per litre
K_{Phenol}	Absorption coefficient of phenol
K_{app}	Apparent rate constant (min^{-1})
r	Rate of reaction

RESEARCH OUTPUTS

Journal articles

1. Adenuga, D. O., Tichapondwa, S. M., & Chirwa, E. M. N. Bismuth and Silver-based Visible Light Activated Photocatalysts for Aromatic Compound Degradation: Synthesis, Characterisation and Efficacy. *Journal of Cleaner Production PRES'19 Special Issue* [Submitted]

2. Adenuga, D., Tichapondwa, S., & Chirwa, E. (2019). Synthesis and Characterization of Potential Visible-light Photocatalyst and Its Photocatalytic Activity in the Decomposition of Phenol. *Chemical Engineering Transactions*, *74*, 1087-1092. https://doi.org/10.3303/CET1974182

3. Adenuga, D. O., Tichapondwa, S. M., & Chirwa, E. M. N. (2019). Ternary Ag/AgCl/BiOCl Synthesis and the Effects of its Constituents on Phenol Degradation. *Chemical Engineering Transactions*, *76*, 127-132. https://doi.org/10.3303/CET1976022

4. Farai F. Masinire, Dorcas O. Adenuga, Shepherd M. Tichapondwa, Evans M.N. Chirwa. Remediation of Chromium(VI) Containing Wastewater using *Chrysopogon zizanioides* (vetiver grass). *Chemical Engineering Transactions* [Accepted]

Conference presentations

5. Synthesis and Characterisation of Ag/AgCl/BiOCl and its Photocatalytic Activity in Phenol Degradation. 14th International Congress on Chemical and Process Engineering. 25th - 27th May 2019, Bologna, Italy. (oral presentation)

6. Ternary Ag/AgCl/BiOCl Synthesis and the Effects of its Constituents on Phenol Degradation. 22nd conference on Process Integration, Modelling and Optimisation for Energy Saving and Pollution Reduction. 20th -23rd October 2019, Agios Nikolaos, Greece. (oral presentation)

CHAPTER 1

INTRODUCTION

1.1. Background

Semiconductor photocatalysis, a version of advanced oxidation process (AOP), has shown potential for treatment of contaminants in water especially where the water is contaminated with micropollutants and complex organic materials (Mohammed, 2007). Due to its ability to completely mineralise organic pollutants leaving no traces of the compound, photocatalysis has been referred to a “Clean” technology. Potentially, photocatalysis can also be classified as a “Green or fossil energy free” technology if solar radiation is used with the catalysts. Photocatalysis has been tested in the destruction of bacteria and virus, cancer cells inactivation, odour mitigation, water photo splitting and oil spillage clean-ups (Hoffmann et al., 1995). Photocatalysis involves the use of a semiconductor catalysts suspended in aqueous medium which when illuminated results in the production of photogenerated holes and electrons on the surface of the catalyst. This enables toxic pollutants to be degraded into non-toxic and non-hazardous compounds such as water, carbon dioxide and other small molecules (Li et al., 2017b).

Titanium based photocatalysts have been widely used due to their relatively low cost, stability and inertness in aquatic systems (Xiao et al., 2016). However, titanium based photocatalysts are characterised by their high electron-hole recombination rates, low quantum yields and wide band-gap energy which makes them unsuitable for visible light activation and only viable for activation and usage in the ultraviolet light region (Chen et al., 2016b).

Other semiconductor catalysts grouped as oxides, sulphides, oxysulfides, nitrides and oxynitrides have gained attention due to their potential application for solar energy conversion and their ability to degrade environmental pollutants (Wang et al., 2014). This is advantageous because visible light represents 45% of the solar spectrum and

a visible light activated catalyst will enable the use of solar energy for photocatalysis (Manassero et al., 2013; Niu et al., 2014).

Examples of catalyst being investigated in recent years are bismuth-based oxyhalides. This is due to their uncommon properties of layered structures and their demonstrated potential for activation in a wide electromagnetic band including the visible light range. The bismuth-based oxyhalides has been tested in catalysis, nanodevice and nanosensor development and its eco-friendly pigments (Wang et al., 2014; Chen et al. 2016b). The layered structure of bismuth oxyhalides provides a large enough space for the atoms and orbitals to be polarised thereby separating the electron-hole pair effectively and reducing recombination of the generated electron-hole pairs (Wang et al., 2014). Bismuth oxychloride (BIOCl) is one of the bismuth oxyhalides which has attracted vast attention due to its high photocatalytic activity in the degradation of cationic dyes such as methylene blue and rhodamine blue (Zhao et al. 2018a).

Different synthesis techniques are used to produce BiOCl. Depending on the process used, different crystalline structures and macroparticles are produced, such as, nanoflowers, nanorods, nanosheets, nanobelts, thin films which all have different morphology and surface area, consequently affecting the band gaps and photodegradation potential (Kumar et al., 2018; Cheng et al. 2014). BiOCl, just like TiO_2, exhibits a wide band gap and therefore, is mainly activated within the UV range (Cai, 2015). This has led to research into improving the visible light responsiveness of BiOCl. Some good materials were discovered for this purpose, one of which is the AgX (X = Cl, Br, I). AgX has a wide band-gap and therefore cannot be photo-excited under visible light irradiation (Mytych and Stasicka, 2004), however, it improves the visible light responsiveness of some large band-gap semiconductors (Ao et al., 2014).

It is also known that upon light illumination, AgX can form a Ag/AgX composite as a result of decomposition of AgX to Ag metal nanoparticles. Previous work has shown that Ag/AgX/BiOX has shown good photodegradation activity in the degradation of dyes and organism sterilization (Chen et al., 2016b). Herein, we attempt the synthesis of flower-like Z-scheme Ag/AgCl/BiOCl composite particles for potential visible light degradation. The constituent compounds, AgCl, BiOCl and AgCl/BiOCl were also synthesised. The obtained particles were fully characterised through various

techniques and their photodegradation efficacy for phenol degradation under UV and visible light irradiation was investigated.

1.2. Z-scheme photocatalysis

Z-scheme photocatalysis is inspired by natural photosynthesis which involves two cascaded excitation steps for the conversion of CO_2 to sugars. Wang et al. (2018) explains the process using Figure 1.1 where P680 and P700 are photosystems present in plants. They contain chlorophyll that enables them to collect light energy. When light is illuminated on the chlorophyll in photosystem II (PSII), there is separation of electrons and holes. The holes oxidise water to form protons, oxygen and electrons. The protons support the formation of adenosine triphosphate (ATP) from adenosine diphosphate (ADP) while in photosystem I, the holes are quenched by the electrons formed in PS II and the electrons formed in PS I reduces $NADP^+$ (nicotinamide adenine dinucleotide phosphate) to NADPH. The free energy power from ATP and NADPH reducing agent are responsible for CO_2 conversion to carbohydrate where oxygen and hydrogen (water splitting) is produced as a side reaction.

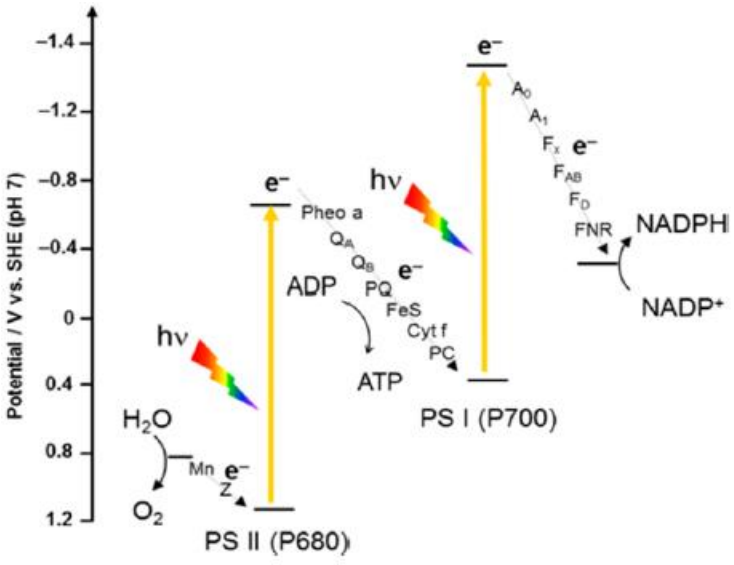

Figure 1.1: Natural photosynthesis double excitation process on P680 and P700 (Wang et al., 2018)

It was noticed that this natural occurring two-step photoexcitation photosynthesis can be adopted for the degradation of organic contaminants through the Z-scheme

heterojunction system. The heterojunction of composite photocatalysts aids photocatalysis because it possesses high reduction and oxidation potential while simultaneously ensuring high electron-hole separation which consequently widens its light absorption range. This makes it viable for visible light activation. These characteristics makes it superior as it is difficult for a single photocatalyst component to embody all these special attributes (Zhou et al., 2018). This photocatalytic system used in the fabrication of photocatalysts in this study, contributes to solving the general environmental and energy problems as lower energy i.e. visible light is required to drive the system.

1.3. Aims and objectives

The aim of this study was to achieve photocatalysis under visible light irradiation in the degradation of organic contaminants. The aim was achieved by carrying out the following specific objectives:

- To synthesise and characterise photocatalyst Ag/AgCl/BiOCl and its constituent compounds i.e. AgCl and BiOCl and AgCl/BiOCl.
- To investigate the photocatalytic activity of the synthesised materials in the degradation of phenol under both ultraviolet and visible light irradiation. This activity was compared to commonly used TiO_2 under both light sources.
- To optimise and model kinetic parameters of the phenol degradation using the synthesised photocatalyst in visible light irradiation.

Scheme 1 shows the schematics for the flow of experiments and analysis carried out in this study.

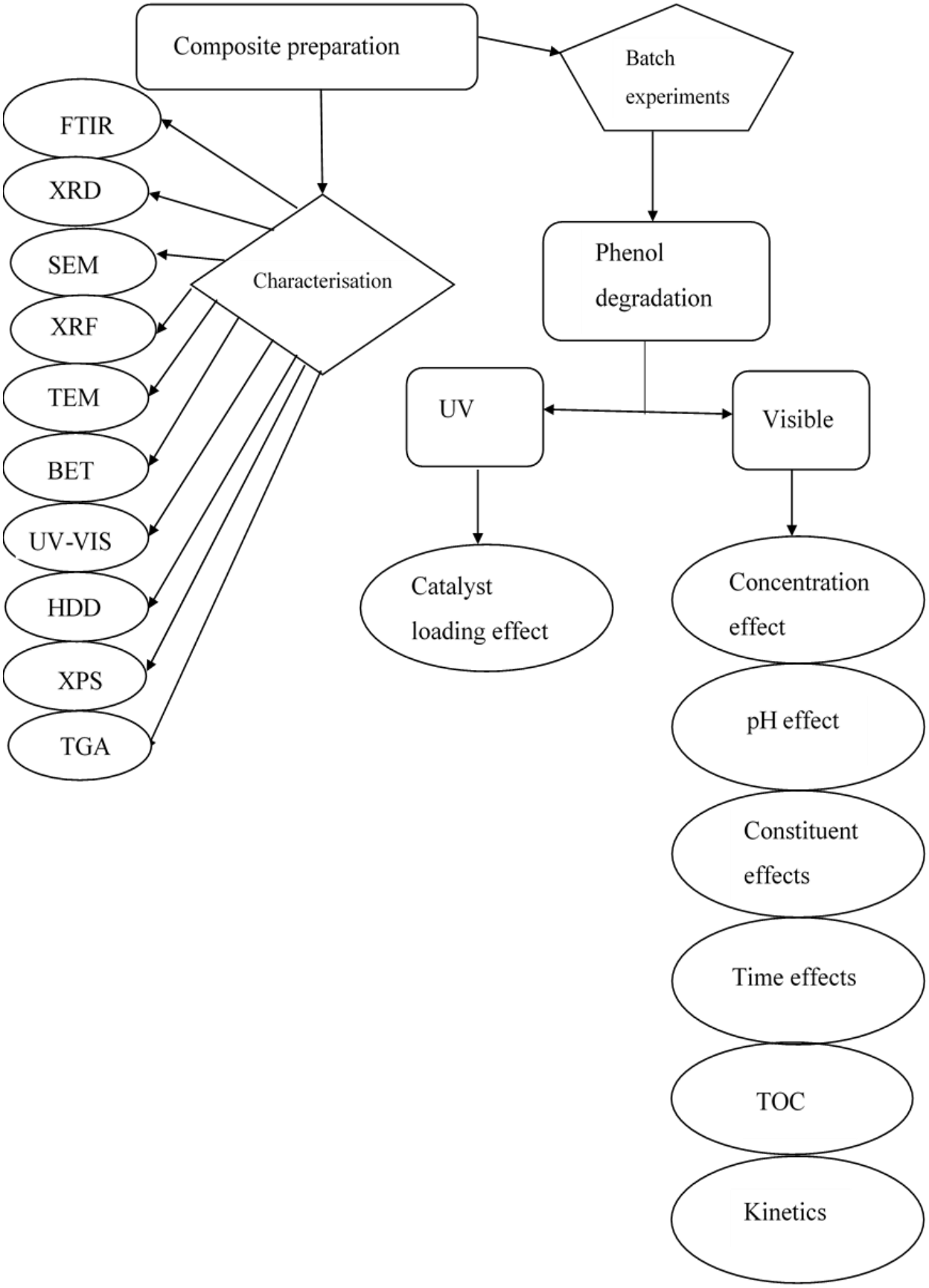

Scheme 1: Summary of material characterisation and experiment conducted using the synthesised catalysts

1.4. Thesis scope

Chapter 1: Introduction;

This chapter describes the background information, motivation for this study, aims and specific objectives.

Chapter 2: Literature review;

This chapter reviews the current and previous trends in photocatalysis, materials development and combinations and removal of organic contaminants such as phenol.

Chapter 3: Materials and methods;

This chapter describes the materials and methods used in this study with regards to the synthesis, characterisation, analytical and degradation studies.

Chapter 4: Catalyst characterisation;

This chapter describes the characterisation of the synthesised photocatalysts to determine their physicochemical properties.

Chapter 5: Degradation studies;

This chapter assesses the degradation potential of all synthesised catalysts in the degradation of phenol under both ultraviolet and visible light degradation. The chapter assess various variables such as the effects of the initial photocatalyst concentration, initial phenol concentration, pH, catalyst constituent, catalyst reuse, degradation kinetics and mineralisation analysis.

Chapter 6: Conclusions and recommendations;

This chapter presents the conclusions based on this study, the limitations experienced and recommend future work.

CHAPTER 2

LITERATURE REVIEW

2.1. Advanced oxidation processes (AOPs)

Advanced oxidation processes (AOPs) are a class of water treatment processes whose common factor is the utilisation of reactive oxygen species such as superoxide ($O^{\bullet}$) and hydroxyl radical ($OH^{\bullet}$) to oxidise complex organic compounds to their simplest entropic forms CO_2 and H_2O. The generation of oxygen reactive species is achieved either chemically using oxidising reagents such as the Fenton and Photo-Fenton reagents, or by use of semiconductor particle photocatalysts that can be activated by light sources such as UV lamps or solar radiation. Oxidation of organic compounds using reactive oxygen species generated from collapsing microscopic bubbles under ultrasonic pressure (ultrasonic cavitation) has also been attempted (Wang et al., 2008). AOPs have been used in wastewater treatment in the degradation of a wide range of recalcitrant organic contaminants and microbes (Byrne et al., 2018). Processes using AOP have the ability to degrade recalcitrant organic compounds while leaving no trace of toxic intermediates in the wake of the degradation of the parent compounds (Bethi et al., 2016). Organic compounds react with the hydroxyl radical to form another radical that is carbon-centred. This carbon-centred radical reacts with molecular oxygen to form peroxyl radical which again undergoes reactions to produce a host of other oxidation products such as ketones, aldehydes and alcohols. These products tend to be less toxic than the original contaminant and more responsive mineralisation using cheaper, environmental friendly biological processes (Makgato and Chirwa, 2015; O'Shea and Dionysiou, 2012).

Hydroxyl radicals are known to be very reactive and non-selective and can mineralise hazardous compounds completely to CO_2 and inorganic ions. This is as a result of its high standard potential of 2.8 V in acidic media and 1.55 V in basic media (Wang and Xu, 2012). The most common photochemical AOPs are TiO_2 photocatalysis and photo-Fenton (Byrne et al., 2018) process while other known processes are ozonation, sonolysis, Fenton and photolysis.

2.1.1. Ozonation

Ozone (O_3) is a selective oxidant that undergoes two oxidation mechanisms which involves an indirect attack through the formation of a hydroxyl radical or through a direct electrophilic attack by molecular ozone (Deng and Zhao, 2015). Ozonation in the presence of ultraviolet irradiation (UV) results in the generation of hydrogen peroxide (Liu et al., 2013). Previous research has shown that mineralisation of organic contaminant through ozonation is very limited as a result of the relatively low solubility and stability of ozone in water and its slow reaction with some organic compounds (Wang and Xu, 2012). Also, due to the instability of ozone, only an ozone generator can be operated practically and stably (Wei et al., 2016).

2.1.2. Sonolysis

Sonolysis involves the formation $OH^{\bullet}$ radical under ultrasound irradiation through oxidative techniques involving the use of ultrasonic waves with frequencies above the hearing range of an average person (>16 kHz) (Wang and Xu, 2012). The hydroxyl radical formed is localized at a near or near a gas-liquid interface (O'Shea and Dionysiou, 2012). Its principle of operation is based on cavitation which includes the forming, growth, and breakdown of bubbles in a liquid. The use of sonolysis can be used in addition to ozonation or hydrogen peroxide. This will result in an increase in the rate at which free radicals is generated, more free radicals will be available for the reaction and thereby increasing the rate of the reaction. An increase in the extent of degradation is noticed because of the turbulence generated by the cavitation (Wang and Xu, 2012). The use of ultrasound in the treatment of wastewater has been extensively investigated as having potential in the removal of emerging pollutants, wastewater disinfection, solid waste treatment prior to digestion, landfill pre-treatment and air-purification, it utilises high energy consumption while still lacking the capacity of removing organic pollutants (Naddeo et al., 2014).

2.1.3. Fenton process

Fenton's reagent is a type of oxidation process that makes use of a mixture of hydrogen peroxide (H_2O_2) and iron II ions for the generation of hydroxyl radicals capable of oxidizing contaminants in wastewater (El Haddad et al., 2014). This process is illustrated using the following Equations: (Deng and Zhao, 2015)

$$Fe^{2+} + H_2O_2 \rightarrow Fe^{3+} + OH\cdot + OH^- \quad (1)$$

$$Fe^{3+} + H_2O_2 \rightarrow Fe^{2+} + HO^{\cdot}_2 + H^+ \quad (2)$$

$$OH\cdot + H_2O_2 \rightarrow HO^{\cdot}_2 + H_2O \quad (3)$$

$$OH\cdot + Fe^{2+} \rightarrow Fe^{3+} + OH^- \quad (4)$$

$$Fe^{3+} + HO^{\cdot}_2 \rightarrow Fe^{2+} + O_2H^+ \quad (5)$$

$$Fe^{2+} + HO^{\cdot}_2 + H^+ \rightarrow Fe^{3+} + H_2O_2 \quad (6)$$

$$2HO^{\cdot}_2 \rightarrow H_2O_2 + O_2 \quad (7)$$

The OH· produced through electron transfer in Equation 1 is scavenged in Equation 2 and Equation 3 respectively. Photo-Fenton process is just like the Fenton process except that UV light is being applied in order to enhance the reduction of the dissolved Fe^{3+} to Fe^{2} (Deng and Zhao, 2015). Environmentally friendly reactant like H_2O_2 is easy to use because it does not require special equipment for its use and does not require energy for its activation. Fenton and Photo-Fenton processes are disadvantageous in that they consume Fe^{2+} at a faster rate than its regeneration rate. Highly toxic by-products are formed and this therefore increases the cost due to the need for the treatment and processing of the sludge produced (Ribeiro et al., 2015). The Fenton process is only efficient at pH levels within 3 and 4. Therefore, continuous pH adjustments need to be included in the setup increasing the risks of transportation and storage.

2.1.4. Photolysis

Photolysis of water involves the production of strong oxidising species (hydroxyl radical) and reducing species (hydrogen radical) that aids in the degradation of contaminant as a result of high energy released due to UV irradiation (Wang and Xu, 2012). This can be achieved in water at a wavelength that is less than 242 nm according to Equation 8:

$$H_2O + hv \rightarrow OH\cdot + H\cdot \quad (8)$$

Although, various research has been done and the use of UV and vacuum ultraviolet irradiation in the treatment of wastewater has been investigated, it has been noted that photolysis is effective in water disinfection under ultraviolet light irradiation but cannot degrade organic pollutants especially that of aromatic compounds such as phenols in visible light (Alapi and Dombi, 2007).

2.1.5. Photocatalysis

Photocatalysis is a reduction-oxidation technology for environmental applications because of its ability to degrade and detoxify toxicants. Photocatalysis is defined as a light driven process that occurs over the surface of a catalyst that is illuminated (Zhu and Wang, 2017). These photons cause excitement of electrons and formation of holes. These electrons react with oxygen to produce superoxide radical or hydroperoxide radicals. The formed reactive species are able to degrade pollutants into water and carbon dioxide (Bryne et al., 2018). Semiconductor materials such as TiO_2, ZnO, Fe_2O_3, CdS and ZnS can be used to propagate photocatalysis (He et al., 2018) through light-reduced redox reactions due to their electronic structures comprising of a filled valence band and an empty conduction band. Photocatalysis is very effective in the degrading of non-biodegradable organic contaminants in waste water (Hoffmann et al., 1995; Mahlambi et al., 2015).

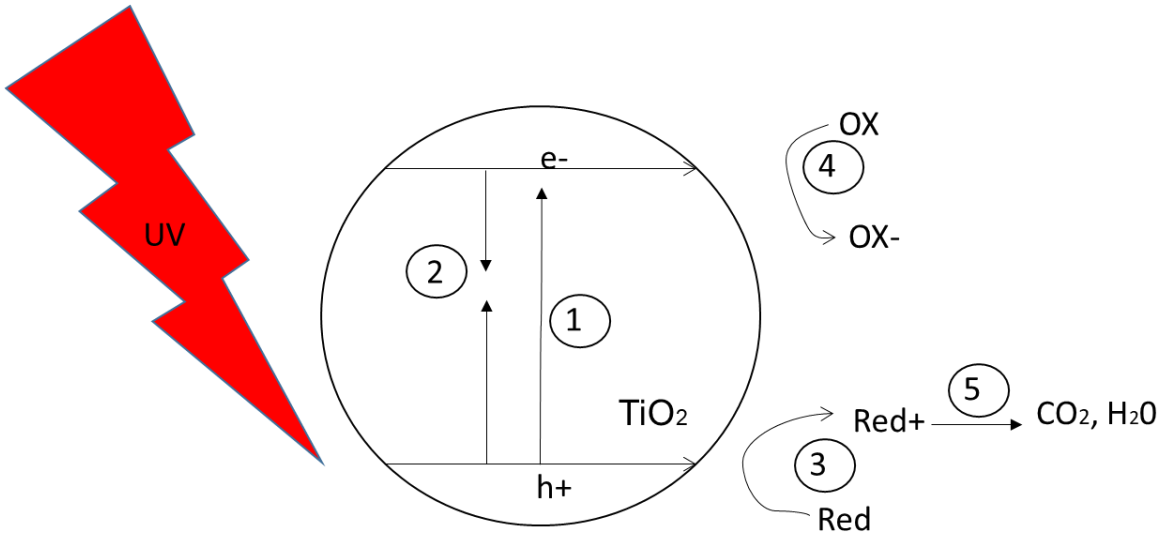

Figure 2.1: TiO_2 photocatalytic mechanism under UV light irradiation

The general photocatalytic mechanism is described such that, a photon with an energy of *hv* matches or exceed the bandgap energy E_g of the semiconductor. This results in an electron e_{cb} being promoted from the valence band *VB* into the conduction band *CB* leaving a hole, h_{vb}^+. These VB holes and excited CB electrons can recombine or be dissipated as heat in the absence of electron and hole scavengers, be trapped in metastable surface states, or react with electron donors and acceptors that have been adsorbed on the surface of the semiconductor or within the surrounding of the charged particles (Ibhadon and Fitzpatrick et al., 2015).

Figure 2.1 illustrates the steps in the photo electrochemical mechanism using TiO_2 as semiconductor and step 1 – 5 is explained as follows:\

1. Excitation of the electron from the valence band to the conduction band creating a hole in the valence band.
2. Shows the recombination of holes and electrons. This can be prevented in the presence of electron scavengers or suitable surface defects that trap electrons.
3. Illustrates a reductive pathway as a result of a VB hole.
4. Illustrates an oxidative pathway by a CB electron.
5. Yields the mineralisation products as a result continued photocatalytic reactions.

2.2. Catalyst materials

There has been continuous development and manipulation of matter to form new and advanced structures and systems that shows different chemical, physical and biological properties. These materials exhibit different characteristics in optical, electrical and magnetic properties (Kumar et al., 2014). Bethi et al. (2016) grouped these materials for the degradation of wastewater into four categories namely (1) dendritic polymers, (2) zeolites, (3) carbon-based and (4) metal/metal oxide. This study focus on metal/metal oxides in the degradation of organic contaminants.

2.2.1. Semiconductor photocatalysts: Titanium dioxide (TiO_2)

Titanium oxide based photocatalytic oxidation is the most widely used technology due to the stability of TiO_2. It is a cheap, non-toxic catalyst that is used in the form of a nanoparticle with very high surface area. TiO_2 was first discovered about 90 years but was not utilised as a photocatalyst until it was discovered by Fujishima and Honda (1972) that it has photocatalytic water splitting abilities (Byrne et al., 2018). A major disadvantge in the use of TiO_2 for photocatalysis is that it has a relatively wide band-gap of between 3 eV and 3.2 eV which can only be activated by the UV range. This means that TiO_2 use as a photocatalyst in sunlight is limited as sunlight consists of 5% UV, 43% visible and 52% infrared (Ji et al., 2012). In order to improve the photocatalytic properties of TiO_2 and shift its adsorption from the UV to visible lights region, a modification is done by doping of TiO_2 or deposing metal or non-metal elements into the TiO_2 lattice (Byrne et al., 2018).

The limitations faced in the use of TiO_2 as a semiconductor photocatalyst is illustrated in Scheme 2.

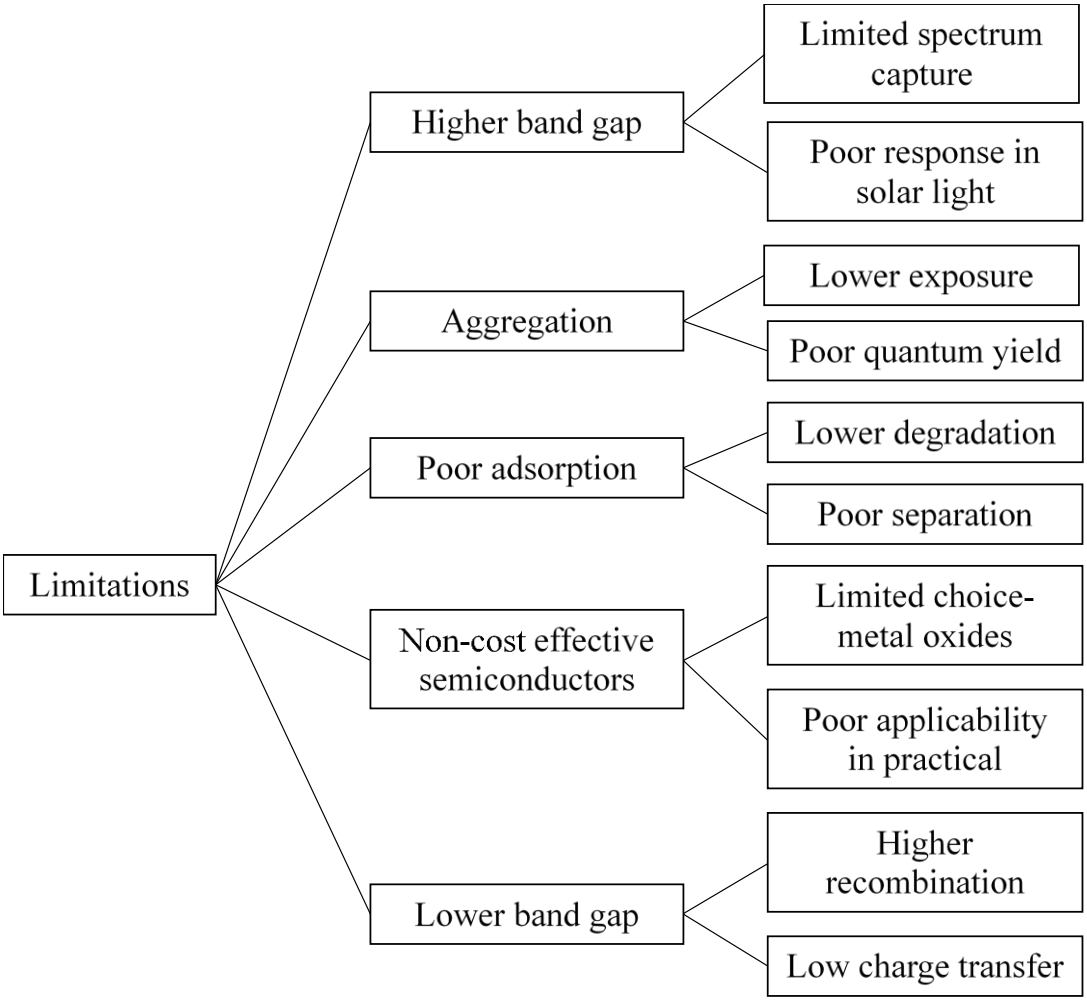

Scheme 2: Limitations of conventional TiO_2 photocatalysis (Kumar et al., 2018)

Its high band-gap means it is unable to be activated under solar light irradiation and therefore has a limited spectrum capture. Aggregation of catalysts and poor absorption causes lower degradation, poor exposure on the surface of the catalyst and consequently leads to poor separation of the electron and holes. This hinders the catalyst from being applicable in the real world.

2.2.2. Catalyst combinations

Metal oxides such as TiO_2 are the most utilised photocatalysts in wastewater remediation but only responds to ultraviolet (UV) ($\lambda < 380$ nm) lights. This serves as a disadvantage due to the fact that the component of UV light in sunlight energy is just 4%. Visible light is known to occupy about 49% of sunlight energy therefore;

photocatalysts that can explore this characteristic to its full potential should be explored (Lin et al., 2018).

To improve the visible light responsiveness of various photocatalysts, various interventions such as doping, p-n junction formations, alloying and sensitisation have been employed to shift the bandgap of photocatalysts into visible light regions (Bhachu et al., 2016). These method of heterogeneous coupling have improved photocatalytic activity by reducing the rate of recombination of photogenerated carriers (Liu et al., 2017) since a component of the coupled photocatalyst will possess a good light absorption range absorption while the other will have good redox ability thereby enhancing the visible light photocatalytic activity of the semiconductor photocatalyst (Du et al., 2019).

A major strategy has been to utilise materials that are not usually used as photoelectrodes such as bismuth oxyhalides. Oxyhalides are known to be indirect band gap semiconductors (Ran et al., 2018) that are characterised by a relatively slow recombination rate for photogenerated electrons and holes. Bismuth oxyhalides, (BiOX) (X = Cl, Br, I) are known to be of great importance due to their optical properties and potential for industrial applications such as catalysts, pharmaceuticals, nanodevice and nanosensors (Li et al., 2017b), environmentally friendly pigments and ferroelectric materials. Bismuth oxychlorides possess high anisotropic properties due to the presence of a weak inter-layer Van der Waals force coexisting with a strong intra-layer bonding (Tien et al., 2013). The layered {X-Bi-O-Bi-X} bonding are stacked together in a tetragonal matlockite structure (Bhachu et al., 2016).

Orbitals of some p-block metals such as Ag 4d in Ag(I), Sn 5s in Sn(II) and Bi 6s in Bi(III) have been noticed to hybridize O 2p levels to form a new preferred hybridized VB thereby narrowing the bad gap to harvest visible light (Chen et al., 2017). Bismuth-based materials are characterised by low toxicity and are abundant on earth while bismuth-based semiconductors such as Bi_2O_3, $CaBi_2O_4$, Bi_2WO_6, $BiVO_4$, $Bi_4Ti_3O_{12}$, $Bi_2O_2CO_3$ and $BiOIO_3$ have shown to have efficient photocatalytic performances in the purification of wastewater and the removal of harmful pollutants (Cheng et al., 2014).

It has been noted that the band gaps for BiOX (X = Cl, Br, I) becomes narrower as we go down group 7 on the periodic table – BiOCl (~3.3 eV), BiOBr (~2.7 eV) and BiOI (~1.8 eV) (Bhachu et al., 2016). Due to the characteristic wide band-gap possessed by BiOCl, this semiconductor absorbs only UV light and therefore in theory, cannot degrade environmental pollutants under visible light (Lin et al., 2018). As a result of this characteristic, research was done in order to make a BiOCl based photocatalysts that are functional under visible light irradiation. This can be achieved by incorporating metal ions or coupling with other semiconductors. Although theoretically, BiOCl has a high bandgap that is similar to TiO_2, its unique structure, morphology and physiochemical property makes it a good candidate for coupling with other materials (Liu et al., 2017).

One dimensional (1D) nanostructured semiconductors are materials characterised by their thickness and width in the nanoscale range with their length at several micrometres. This high aspect ratio promotes fast separation of photo-induced electrons and holes consequently resulting in highly efficient photocatalytic reactions. Two dimensional (2D) nanomaterials are known to arise from lamellar structures built from weak Van der Waals forces or electrostatic forces. This layered structure and the formed intra-electric field could accelerate the transfer of the photo-induced carriers and enhance the photocatalytic activity. Three dimensional (3D) nanostructures or microstructures are known to be more attractive for conversion and storage of solar energy due to their 3D architecture. This 3D architecture equips the BiOX (X = Cl, Br, I) semiconductors with better light harvesting, shortened diffusion pathways, faster interfacial charge separation and more reactive sites which results in enhancing their photocatalytic efficiencies (Cheng et al., 2014). Economically, BiOCl is known to be a cheap material because it is chemically inert, corrosion resistant and requires little to no post-processing (Sarwan et al., 2012).

Ag/AgCl materials have been reported to have a surface plasmon resonance (SPR) effect that is activated by both UV and visible photons and therefore results in excellent photocatalytic activity (Wang et al., 2008). SPR is defined as the resonant photon-induced oscillation of valence electron when the frequency of photons matches the natural frequency of surface electrons oscillating against the restoring force of positive nuclei (Meng and Zhang, 2016). The SPR redox ability and light absorption range

extension is achieved in three ways, namely: direct electron transfer, enhancement of local electromagnetic field or transfer of resonant energy (Zhang et al., 2019)

Silver/silver halide based (Ag/AgX, X = Br, Cl) nanomaterials have been reported to have excellent photocatalytic performances in the degradation of pollutants under visible light irradiation (Wang et al., 2017). Although, metal halides such as AgCl and AgBr have been noted to have a higher degradation potential as compared to metal oxides, however, they cannot be used as individual photocatalyst as they are characterised by poor photostability (Lin et al., 2018). A loss of photocatalytic activity is registered due to the low surface area of pure Ag/AgX and the recombination of plasmon induced electron lone pairs before arriving at the surface. Therefore, a material to be used as a suitable photocatalyst should have a high surface area, high thermal and chemical stability and possess excellent carrier charge mobility (Wang et al., 2017). Previous studies have showed that TiO_2 doped with AgCl illustrates an improved photocatalytic activity (Ye et al., 2012).

Ag/AgCl has been doped with other materials to form photocatalyst composites which have been used in the degradation of dyes and other organic compounds as shown in Table 2.1. This heterogenous system involves various heterojunction structures of photocatalytic coupling. Figure 2.2a shows a Type-II hererojunction whereby two semiconductors with unaligned bandgap structures are assembled. When light with photon energy greater than the bandgap of both photocatalyst illuminates the surfaces, electron-hole pairs are generated and the electrons in photocatalyst 1(PC 1) migrate to the conduction band of photocatalyst 2 (PC 2). The photogenerated holes in the valence band (VB) PC 2 moves to the VB of PC 1 ensuring enough space between the photogenerated electron holes and electrons consequently inhibiting recombination (Zhou et al., 2014).

Meanwhile, in the Direct Z-scheme illustrated in Figure 2.2b, the strong oxidizing electron in PC 1 and the strong reducing hole in PC 2 is retained, while the weak electron in the CB of PC 2 and hole in the VB of PC 1 recombines. This also results in enhanced photocatalytic activity because special separation of the reducing and the oxidative sites (Xu et al., 2018a).

In the all-solid-state Z-scheme photocatalytic system illustrated in Figure 2.2c, in conjunction with PC 1 and PC 2, a third element, conductor (C) is employed to act as an electron mediator which forms a Ohmic contact between PC 1 and PC 2 (Zhou et al., 2014).

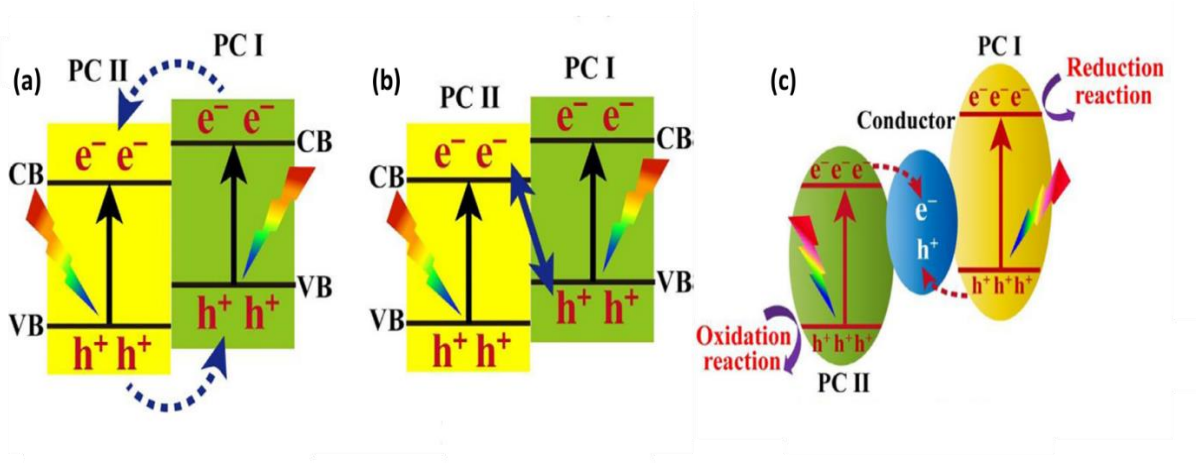

Figure 2.2: (a) Schematic illustration of type-II heterojunction, (b) Schematic illustration of Direct Z-scheme and (c) Schematic illustration of All-solid-state-Z scheme (Xu et al., 2018a)

Examples of noble metals commonly used as conductors are Au, Ag and Cu. This is because they excellent electron mediators, an important characteristic important for the transfer of photogenerated carriers while improving the stability of photocatalysts (Xu et al., 2018a). The generated electrons from the conduction band of PC 2 combines with the photogenerated holes from PC 1 on the surface of the Ohmmic conductor. This ensures that the electrons on the conduction band of PC 1 are solely available for the reduction reactions while the holes in the valence band of PC 2 are reserved for the oxidation reaction. Ag nanoparticles formed on the surface of the AgCl as a result of photoreduction of Ag^{+} to Ag^{0} has an advantage of being used as an electron mediator enhancing the solar energy activity of the photocatalyst composite as a result of its SPR effects (Li et al., 2019a).

For this reason, this study aims to synthesise an all-solid state Z-scheme Ag/AgCl/BiOCl composite photocatalyst with a flower-like morphology and investigate its photocatalytic activity under both UV and visible light irradiation in the degradation of phenol.

Table 2.1: Ag/AgCl composite particles as synthesised in previous studies

Photocatalyst	Pollutant	Investigation	Remarks	Reference
Hollow Ag/AgCl/BiOCl	Methyl orange (MO)	Ag/AgCl/BiOCl synthesis, characterisation and photodegradation of MO using a 5W Led visible light.	20% Ag/AgCl/BiOCl showed high photocatalytic activity for MO under LED irradiation. h^+ and $\cdot O^-$ plays significant role in MO degradation.	Chen et al. (2016b)
Flower-like Ag/AgCl/BiOCl	RhodamineB, Tetracycline	Synthesis through a solvothermal method, characterisation, visible light degradation of pollutants using a 500 W Xe lamp. Recycling of catalysts.	Followed first-order kinetics. Ag/AgCl/BiOCl shows a higher photocatalytic activity in visible light than pure BiOCl.	Zhao et al. (2018b)
Ag/AgCl/BiOCl nanosheets	S. aureus	Synthesis, characterisation, photocatalytic inactivation of bacteria using a 500 W Xe lamp, inactivation mechanism proposed.	Ag/AgCl/BiOCl showed higher photocatalytic activity in comparison to Ag/BiOCl, AgCl/BiOCl and Ag/AgCl/TiO_2.	Wei et al. (2016)
AgCl nanotubes/BiOCl nanosheets	Methyl orange	Synthesis, characterisation, degradation, catalyst recyle and nanosheet/nanotubes degradation mechanism.	Followed pseudo-first-order kinetics. Strong visible light response and improved separation of photogenerated electron holes.	Zhao et al. (2019)

Ag/AgCl/WO_3-nanoflakes	4-Aminobenzoic acid (4-ABA)	Synthesis in geothermal water (chlorine source), visible light degradation of pollutant using a 300 W xenon lamp, stability test and degradation mechanism.	The 50 wt% Ag/AgCl/WO_3 showed a higher photocatalytic activity under visible light irradiation in comparison to Ag/AgCl and WO_3.	Li et al. (2018a)
Poly(N-hexadecyl pyridine acetylenic alchohols bromide)-Ag/AgCl (Pp-16@Ag/AgCl)	Rhodamine B and fast green dyes	Synthesis, characterisation of photocatalyst, its degradation of pollutants and reusability tests.	The composite showed high photocatalyst activity in the degradation of RB and fast green dye under UV irradiation.	Xia et al. (2018)
Ag/AgCl dispersed on mesoporous Al_2O_3	Methylene orange and methylene blue	Synthesis, characterisation, and degradation of pollutants under a 300 W Xe arch lamp for visible light irradiation.	The photocatalysts exhibited high photocatalytic activity and stability in the degradation of the organic pollutants. Ag/AgCl(Ch_3COOAg)/Al_2O_3 showed the highest photocatalytic activity.	Feng et al. (2016)
Ag/AgCl/SnO_2	Rhodamine B	Synthesis, characaterisation, degradation of pollutants under simulated sunlight irradiation with	Successful synthesis of Ag/AgCl/SnO_2 and its different Ag/Sn molar ratios. Ag/Sn shows	Huang et al. (2017)

		a 500 W xe lamp used as light source.	that 7% shows the the best photocatalytic activity.	
Ag/AgCl/WO_3	Rhodamine B	Microwave assisted synthesis of Ag/AgCl/WO_3, photocatalyst characterisation and its photocatalytic activity under simulated solar light.	The photocatalyst activity of the synthesised photocatalyst in the degradation of dye is noticed to be higher in than WO_3.	Adhikari et al. (2013)
Cyclized polyacrylonitrile (CPAN)/Ag/AgCl	Methyl orange, rhodamine blue	Synthesis, characterisation and photocatalytic activity test of photocatalyst in the degradation of organic pollutants under visible light irradiation using a 300 W iodine tungsten lamp as a lamp source.	The synthesised catalyst showed great activity and stability in the degradation of MO.	Li et al. (2017a)
Ag/AgCl-$CdWO_4$	Rhodamine blue, Methylene blue, methylene orange, phenol	Catalyst synthesis through photoreduction process, characterisation and degradation under visible light with a 300 W xenon lamp as light source.	Complete degradation of RhB, MB and MO using synthesised catalyst in 30 mins. 95% Phenol degradation in 90 mins.	Wen et al. (2017)

Cu_2O/Ag/AgCl microcubes	Methyl orange	Synthesis, characterisation and visible light activated degradation of MO using a 500 W Xe lamp.	93% methyl orange degradation in 16 min. High stability of synthesised catalyst.	Lou et al. (2019)
TiO_2 hollow nanofibers grafted Ag/AgCl (Ag/AgCl-ElTiO_2)	Methyl orange	Synthesis through electrospinning and coprecipitation, characterisation and degradation of MO under visible light (300 W Xe arc lamp) degradation.	Ag/AgCl-ELTiO_2 showed a higher photocatalytic activity in comparison to Ag/AgCl-SGTiO_2, Ag/AgCl, ELTiO_2 and SGTiO_2.	Xu et al. (2018b)
AgCl@Sn-TiO_2 microspheres	Rhodamine blue, 3-aminophenol	Simple hydrothermal synthesis, characterisation and photodegradation of contaminants under visible light.	The synthesised catalyst showed great photocatalytic activity in the degradation of the pollutants and it is noted that the photocatalytic activity is based on the amount of AgCl present in the composite.	Ganeshraja et al. (2018)
Ag-AgCl in porous polyvinyl alcohol (PVA)	Methyl orange	Three–step synthesis, characterisation, visible light degradation under visible light (xenon lamp) and photostability tests.	Ag/AgX has a photoactivity dependence on Cl. The synthesised AgCl/PVA showed week photoactivity under acidic conditions.	Chen et al. (2016a)
AgCl/Ag-cellulose paper	E. coli, S. aureus, S. epidermidis, P.	Synthesis through a facile ultra-sound agitation process,	Successful fabrication of AgCl/Ag hybrid cellulose paper as	Dai et al. (2017)

	aeruginosa, Methyl blue	degradation of organic pollutant under direct sunlight, antibacterial and biocompatibility tests.	confirmed by characterisation. Synthesised catalyst showed superior photoactivity in the inactivation of bacteria and degradation of organic pollutant.	
Ag/AgCl@TiO_2	4-chlorophenol, Cr(VI)	Synthesis through a deposition, precipitation and reduction method. Characterisation of synthesised catalyst and degradation of 4-chlorophenol and photoreduction of Cr(VI) under visible light irradiation.	Successful one-pot synthesis of photocatalyst. Efficient photodegradation of 4-CB and Cr(VI) under visible light. Ag to AgCl ratio discovered to be key component in photoactivity.	Guo et al. (2012)
Ag/AgCl-glass	Methyl orange	Synthesis through a one-step ion exchange method. Visible light (300 W xenon lamp) degradation of MO, stability and reuseability experiments.	Complete degradation of MO in 120 min.	Li et al. (2019b)

2.3. Toxic hydrocarbons

Effluents from pharmaceuticals, coke ovens, steel plants, chemical industries, petroleum refineries, fertilizer and dye plants consist of hazardous organic and inorganic wastes. These toxic organic and inorganic compounds have a tendency to seep into aquatic sources thereby contaminating ground water. Examples of hazardous wastes that have been reported in wastewater sites are phenolic compounds. Phenolic compounds are a group of organic compounds which consists of an aromatic ring that is attached to one or more hydroxyl groups of which the simplest is phenol (Lin et al., 2016).

Phenol

Phenol is the simplest monatomic phenol that is characterised as a crystalline colourless-to-white toxic solid which has a characteristic sweet tarry odour (Duan et al., 2018). Its structure is illustrated in Figure 2.3. Some of its physical properties include a molecular formula of C_6H_5OH, with molar mass 94.11 g/mol with melting and boiling points of 43^0C and 182^0C.

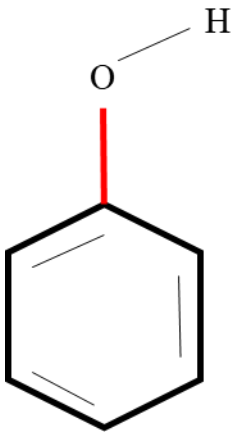

Figure 2.3: Phenol 2D structure

The presence of phenols in natural soil has been linked to the exhaustive use of insecticides, fungicides or herbicides (Xiong et al., 2013). Phenol is produced in large volume as an industrial chemical and also used as an intermediate for the preparation of other chemicals which includes synthetic polymers such as phenolic resins,

chlorinated and alkylated phenols, bis-phenol and caprolactam plastics intermediates (USEPA).

The concentration of phenolic compounds that have been noticed in wastewater ranges from about 200 mg/L to 2000 mg/L while the required standard limit established for release into any aquatic environment is less than 0.5 mg/L. The World Health Organisation (WHO) tags the permissible amount of phenolic components in portable water at 1 µg L^{-1}. This is because phenols have a high solubility in water of 8.28 g/100 mL (Duan et al., 2018). Phenols have been classified as priority pollutants because they are harmful to organisms even at low concentrations they are potentially hazardous to human health and accumulate in the environment. Chronic exposure of phenols to human could lead to vomiting, headache, kidney and liver damage, fainting and anorexia (Mytych and Stasicka, 2004).

Phenol is referred to as an endocrine disrupting chemical because of its ability to modulate the neuro-endocrine system thereby negatively impacting human and animal reproduction (Li et al., 2010). This is because it has a simple structure which is similar to estrogen therefore it is able to mimic and disrupt estrogen activities (Terasaka et al., 2006). When endocrine disrupting chemicals (EDCs) successfully disrupt and block natural hormones, they lead to various abnormalities. Examples of such abnormalities are testicular dysgenesis syndrome and low birth weight in male kids at birth, reoccurring miscarriage in pregnant women, breast and testicular cancer in females and males and could be passed on to future generations (Shekhar et al., 2017).

The criteria and standards division office of water planning and standards United States Environmental Protection Agency (USEPA) Washington D.C states that for freshwater aquatic life phenol concentration should be at 0.6 mg/L in a 24-hour average and should not exceed 3.4 mg/L at any given time. For human health, it states that for protection through ingested water and contaminated aquatic organisms, phenol concentration should not exceed 3.4 mg/L and to prevent adverse effects due to the organoleptic properties of chlorinated phenols formed during purification processes, the concentration should not exceed 0.001 mg/L.

2.4. Reactor configurations

There are various reactor configurations utilised during the photocatalytic degradation of organic pollutants in wastewater. Major factors considered in the design of a reactor are the mass transfer of pollutants, contaminant and photocatalyst distribution, and irradiation source (McCullagh et al., 2011). The distribution of light to a large surface area, light direction with respect to its opacity, light scattering and depth of light penetration influences the design of the reactor (Mukherjee and Ray, 1999). There are two major configurations of photocatalytic reactors which are suspended photocatalytic reactors and immobilised photocatalytic carriers.

2.4.1. Suspended photocatalytic reactors

This reactor configuration involves the dispersion of the semiconductor photocatalyst into the solution containing the pollutant. This type of reactor is also referred to as a slurry type reactor. Slurry photocatalytic reactors which involves the suspension of catalyst particles are the most commonly used reactor systems involving the application of solid catalysts in the liquid phase (Brandi et al., 2016). Srikanth et al., (2017) reports some advantages and disadvantages of slurry reactors. Slurry reactors are advantageous because the catalysts are uniformly distributed. There is potential for high photocatalytic illumination ratio to reactor volume, uniform mixing of suspended particles and little to no mass transfer constraints. There is also good contact between the pollutants and the catalyst in the aqueous solution (Van Gerven et al., 2007). The disadvantages of slurry photoreactors is that at high catalyst loading, aggregation of photocatalysts and light scattering occurs which reduces photocatalytic efficiency. It also requires post-treatment filtration as the photocatalysts materials are small in size and therefore, ordinary sedimentation is not enough to remove the particles to the bottom of the reactor. Mukherjee and Ray (1999) further grouped this configuration of photocatalytic reactor into categories based on the mode of light illumination. These are; immersion and external type reactors.

2.4.1.1. Immersion reactor

Immersion reactor is when the lamp is immersed and contained within the reactor as illustrated in Figure 2.4. These type of reactors are usually efficient because the lamps are surrounded by the solution to be irradiated. This type of reactor usually requires temperature control as an increase in the temperature of the sample solution could affect the photocatalytic reaction. Therefore, double jacket quartz reactor are usually used by circulating water through the outside circumference of the quartz sleeve.

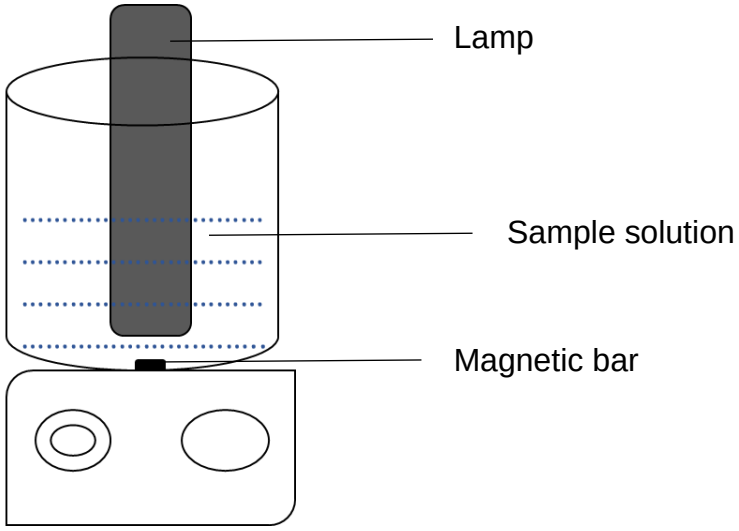

Figure 2.4: Schematic diagram of an immersion reactor

2.4.1.2. External reactor

External type reactor involves lamps outside the reactor with illumination, which could be from above, below or sides of the reactor as seen in Figure 2.5. External reactor illumination are more feasible in laboratory but possibility for scale-up in practice is almost impossible. This is due to the size of light illumination and specific design that will be required for varying industrial applications.

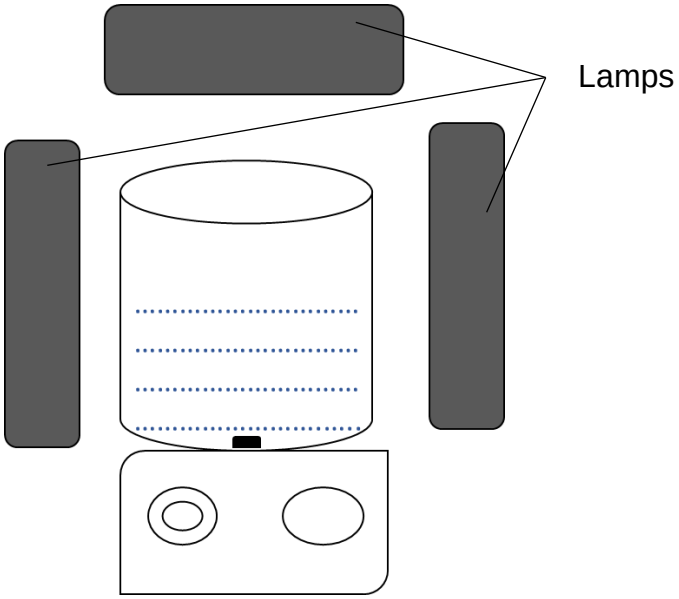

Figure 2.5: Schematic diagram of an external type reactor

2.4.2. Immobilised photocatalytic reactor

Immobilised reactors involve attaching photocatalysts on the surface of supports such as glass, organic polymers or ceramic plates (Miranda-García et al., 2014). Immobilised reactors are efficient for use in continuous reactors. Photoreactor vessels containing particles attached to surfaces (“fixed-film” reactor photocatalysis) has also been successfully implemented in laboratory bench-scale reactors (Khuzwayo and Chirwa, 2016). They are more effective in removal of organic pollutants from aqueous solution if the immobilising material also acts as an adsorbent and has easy separation of catalyst from treated effluent. Immobilised reactors are disadvantageous in that the photocatalyst has lower access to photons, high possibility of the catalyst to be washed out and deactivated, and significant mass transfer limitations of both the external and internal ones (Srikanth et al., 2017). Figure 2.6 shows the immobilised reactor by Ling et al. (2004) where TiO_2 is coated on a glass tube and immersed directly in the reactor for the degradation of phenol and methylene blue dye. The immobilised reactor is combined with the immersion lamp configuration.

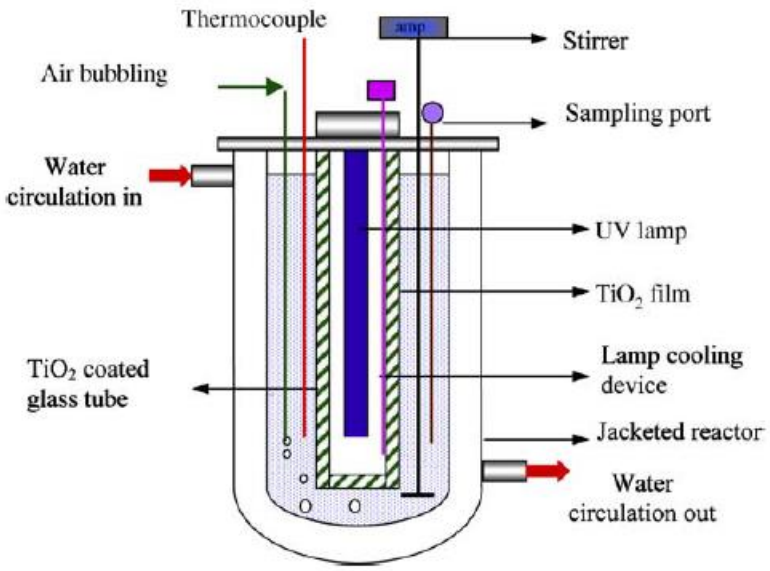

Figure 2.6: Schematic diagram of an immobilised batch reactor (Ling et al., 2004)

There are various advantages and disadvantages associated with reactor types. This includes trade-offs between the kinetics, transport processes and the absorption of light by catalysts (Ray and Beenackers, 1998). For this study, the commonly used laboratory scale slurry batch reactor with an external illumination was utilised with low wattage negating the need for temperature control. Although, it requires post treatment filtration, for scale-up studies, a continuous immobilised reactor will be considered.

2.5. Summary

Different techniques have been employed in the remediation of recalcitrant organic contaminant in wastewater. The limitation of most tested photocatalysis has been the requirement of high pressure UV lamps for catalytic activation and impact of turbidity on reaction rate in suspended particle photoreactors. TiO_2 is the most studied photocatalyst. Major limitations have been experienced in its use mainly due to the requirement of high pressure UV lamps to facilitate the activation of its wide bandgap of approximately 3.20 mV.

In an attempt to tap into solar energy in the photodegradation of organic pollutants, there has been various attempts at improving photocatalytic semi-conductor materials. Modifying their structures and bandgap improves their light spectrum capture,

electron-hole separation and consequently, improves their application under visible light irradiation. This attempts involves different semi-conductor combinations.

This work focuses on synthesising an all-solid-state Z-scheme photocatalyst which combines the properties of AgCl with that of BiOCl in a flower-like structure with photoreduction of Ag on the surface to act as an electron mediator in the ternary composite. Photodegradation experiments utilising the synthesised particles were then carried out under simulated low wattage visible light irradiation in the degradation of phenol.

CHAPTER 3

MATERIALS AND METHODS

3.1. Materials

Hexadecyl trimethyl ammonium chloride (CTAC), Bismuth (III) nitrate pentahydrate ($Bi(NO_3)_3.5H_2O$) and P-25 Degussa TiO_2 were purchased from Sigma-Aldrich Silver nitrate and glacial acetic acid (CH_3COOH) were purchased from Glassworld (Johannesburg, South Africa). All these were used as received and without any further purification. Ultrapure water from a Purelab Flex 3 water was used throughout the experiment. Phenol and HPLC grade acetonitrile was purchased from Merck, South Africa.

3.2. Catalyst synthesis

The preparation procedure for the synthesis of the Ag/AgCl/BiOCl composite photocatalyst was adapted from (Hong et al., 2017) and is as follows. A solution of CTAC was prepared by dissolving 6.4 g of CTAC in 30 mL ultrapure water. In a separate beaker, 30 mL of ultrapure water, 15 mL of glacial acetic acid and 9.7 g of $Bi(NO_3)_3.5H_2O$ were placed. A magnetic bar was placed and the solution was stirred until it became clear and transparent. The clear solution was then added to the prepared CTAC solution to form BiOCl particles. The mixture was labelled “BiOCl” and was stirred for an hour.

In a 1000 mL Erlenmeyer flask, 1.7 g of $AgNO_3$ was dissolved in 925 mL of ultrapure water. The labelled “BiOCl” solution was added to the aqueous $AgNO_3$ solution to form AgCl/BiOCl suspension and this was stirred for another 6 h. The precipitate was collected by centrifuging the solution at 9000 rpm for 10 min at 25℃. The collected precipitate was redispersed in 1 L of ultrapure water before being irradiated under artificial solar lights for 1 h to give an Ag/AgCl/BiOCl suspension.

The obtained particles were collected by centrifuging the suspension for 10 min at 9000 rpm and 25℃. The particles were then washed thoroughly three times with ethanol and then five times with ultrapure water. Each washing step was followed by a centrifuging step to collect the particles. The washed particles were collected and dried at 80℃ for 8 h to obtain the final products.

The synthesis procedure for Ag/AgCl/BiOCl can be summarised by the series of stoichiometric Equation 9 to Equation 12 as illustrated by (Li et al., 2017b).

$$Bi(NO_3) \rightarrow Bi^{3+} + 3NO^-_3 \quad (9)$$

$$Bi^{3+} + C_{16}H_{33}(CH_3)_3N\text{-}Cl \rightarrow C_{16}H_{33}(CH_3)_3N\text{-}Cl\text{-}Bi^{3+} \quad (10)$$

$$C_{16}H_{33}(CH_3)_3N\text{-}Cl\text{-}Bi^{3+} + H_2O \rightarrow BiOCl + C_{16}H_{33}(CH_3)_3N^+ + 2H^+ \quad (11)$$

$$BiOCl + Ag^+ \rightarrow AgCl \quad (12)$$

Equation 9 shows the dissociation of the Bismuth nitrate in solution. Equation 10 illustrates the reaction between the dissolved Bi^{3+} and CTAC to form a complex which consequently begins to nucleate and grow into BiOCl as seen in Equation 11 during stirring. Equation 12 illustrates the formation of AgCl with the reaction of silver ions with BiOCl in the solution. Other synthesis routes utilises NaCl, $BiCl_3$ etc. as chlorine source, but CTAC in this experiment serves as both the chlorine source and a surfactant (Zhang et al., 2013). This synthesis method is shown in Figure 3.1.

AgCl/BiOCl was synthesised using the same synthesis route to Ag/AgCl/BiOCl excluding the photoreduction through irradiation step of the Ag metal. BiOCl was formed through the chemical precipitation reaction of the CTAC solution and the bismuth nitrate solution at room temperature. The resulting BiOCl sample were collected by filtration, washed three times with ethanol and five times with water and dried at 80℃ for 8 h.

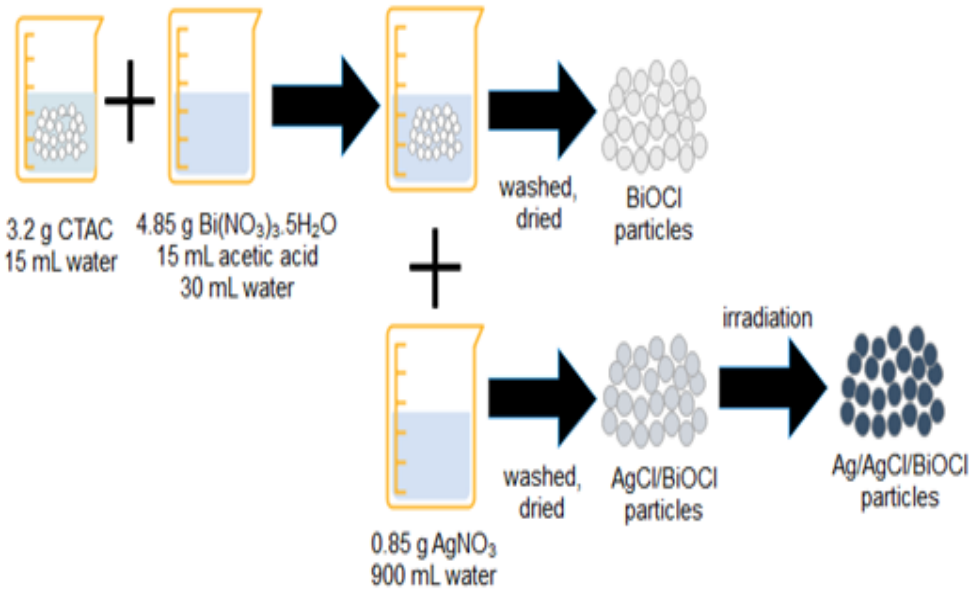

Figure 3.1: AgCl, BiOCl, AgCl/BiOCl and Ag/AgCl/BiOCl synthesis route

Silver chloride (AgCl) was prepared by a precipitation method using CTAC and $AgNO_3$. 3.2 g of CTAC was dissolved in 30 mL of ultrapure water in a beaker. 3.4 g of $AgNO_3$ was dissolved in 70 mL of water in a separate beaker. The CTAC solution was added to the $AgNO_3$ solution to form a suspension which was stirred for five hours followed by washing three times in ethanol and five times with water and dried at 80℃ for 8 h to obtain the final products. Special care was taken during this synthesis to ensure that it is carried out in a dark room to avoid any photoreduction of Ag metals on the surface of the synthesised materials.

3.3. Characterisation

3.3.1. X-ray diffraction (XRD)

The samples were prepared according to the standardized Panalytical backloading system, which provides nearly random distribution of the particles. The sample were analysed using a PANalytical X'Pert Pro powder diffractometer in θ–θ configuration with an X'Celerator detector and variable divergence- and fixed receiving slits with Fe filtered Co-Kα radiation (λ=1.789Å). The mineralogy was determined by selecting the

best–fitting pattern from the ICSD database to the measured diffraction pattern, using X'Pert Highscore plus software.

3.3.2. X-ray fluorescence (XRF)

The samples were prepared as pressed powders. 10-30g powdered sample, mixed with 20 drops Moviol (PVA), pressed to 10 tons. The Thermo Fisher ARL Perform'X Sequential XRF instrument with Uniquant software was used for analyses. The software analyse for all elements in the periodic table between Na and U, but only elements found above the detection limits were reported. The values were normalised, as no loss on ignition (LOI) was done to determine crystal water and oxidation state changes. A standard sample material was prepared and analysed in the same manner as the samples and is reported as such.

3.3.3. Fourier-transform infrared (FTIR)

Infrared spectra (FTIR) were recorded to determine the chemical structure and functional group present in the synthesised photocatalysts.This was done using a PerkinElmer 100 Spectrometer with a MIRacle ATR with Zn/Se. The spectra were obtained in the wavenumber range of 4,000 cm^{-1} to 550 cm^{-1} with a resolution of 2 cm^{-1} and 32 scans.

3.3.4. SEM/SEM-EDS

The morphology of the synthesised particles were captured on a Zeiss Ultra PLUS FEG SEM using the Oxford instruments detector and Aztec 3.0 software SP1. The samples were placed on a strip attached to an aluminium plate and were then coated three times with carbon using a SEM auto-coating unit E2500 (Polaron Equipment Ltd) sputter coater. The elemental analysis and mapping were done using SEM-EDS. The samples were embedded in an epoxy resin with no bubbles and left in the oven for 38 hours at 60 ℃ to polymerize. The samples were polished using sand paper with sizes 180 (30 seconds), 360 (1 min), 600 (2 min), 1200 (4 min) and 2400 (8 min). These were then coated with carbon.

3.3.5. TEM

The morphology and structure of the catalysts were captured using a transmission electron microscopy on a JOEL JEM 2100F TEM. Samples were placed on a TEM mesh grid and coated with a light layer of carbon for stabilisation.

3.3.6. Thermogravimetric analysis (TGA)

This analysis was performed to determine the thermal degradation of the synthesised particles. This was done at a heating rate of 10^0C min^{-1} using a TGA5500. Analysis was carried out at a temperature range of 25^0C – 1000^0C in inert nitrogen atmosphere. Samples were dried and ground to fine powders of which 5 mg samples were weighed on the hang-down pan.

3.3.7. Brunauer-Emmett-Teller (BET)

Specific surface area and pore size was determined using a BET surface area system with a liquid nitrogen temperature of 77.350 K on Micrometrics Tristar II. The sample was dried overnight prior to the BET analysis under pure nitrogen flow at 100^0C so as to eliminate all water molecules.

3.3.8. Ultraviolet-visible spectrophotometer (UV-Vis)

The optical absorption spectra of the synthesised particles were recorded with a UV-vis spectrophotometer Hitachi U-3900 in the range of 191 – 600 nm at a scan speed of 600 nm/min and lamp change wavelength at 340 nm. Dried samples were ground and dissolved in ultra-pure water before measured using a clean and dry cuvette. Prior to analysis, a cuvette was filled with ultrapure water to serve as a blank. This ensures that light losses due to absorption and scattering by the solvent is accounted for.

3.3.9. X-ray photoelectron spectroscopy (XPS)

The elemental composition and chemical state were measured using the XPS. XPS data of the synthesised catalysts were collected using a Thermo ESCALAB 250Xi and using a monochromatic Al Kα X-ray source (1486.7 eV) operated at 300 W. X-ray photoelectron spectroscopy (XPS) consists of irradiating a surface with X-rays in order to extract photo-electrons. Knowing the energy of the X-ray photons and measuring

the kinetic energy of the extracted electrons, one can determine the binding energy of the extracted electrons. This quantity is unique and can be used to identify the elements from which the electrons were extracted. The technique can detect all of the elements (except hydrogen and helium) as well as compounds, because the binding energy of an element differs from compound to compound. It is primarily a surface technique, as the escape depth of the photo-electrons ranges from 2 to 10 nm. The detection limit of XPS is approximately 0.1at%.

3.3.10. Zeta potential and hydrodynamic diameter

The zeta potential and hydrodynamic diameter sizes were determined using a Malvern Zetasizer Nano series (ZEN 3600, UK). pH solutions of between 2 and 12 were prepared using hydrochloric acid (HCl) and sodium hydroxide (NaOH) for adjustment.

3.4. Degradation studies

The efficiency of the synthesised materials as photocatalysts was determined by degrading phenol under both UV and visible light irradiation. Phenol was chosen as the pollutant of study instead of anionic or cationic dyes because it is a known priority pollutant and is also the simplest aromatic compound that forms the binding block of other aromatic pollutants such as dyes, pesticides, antibiotics etc. (Xie et al., 2017). The reactor set up consisted of a light source and a 400 mL glass beaker placed on a magnetic stirrer as depicted in Figure 3.2. Volume of solution in beaker was 300 mL at all times. All these were contained in a box which prevented the effect of natural light. The UV light had a power rating of 36 W and light intensity of 30.66 Wm^{-2} (measured using a Goldilux radiometer/photometer GRP-1 with a UVB probe). The experimental sequence involved continuous stirring for 30 min in the dark to reach adsorption-desorption equilibrium followed by 4 h with irradiation.

Due to low wattage of the light, there was no significant increase in temperature of the experiments, therefore temperature was kept at room temperature. The visible light setup consists of six Osram L 36W 77 G13 Fluora lamps arranged with two lamps at the top, two lamps to the left and two lamps to the right of the beaker (the intensity was 6860 lux measured by a RS PRO ILM01 light meter). Aliquots of 2 mL samples

were taken at time intervals, centrifuged then filtered with a 0.45 µm syringe filter (Millipore) before analysis. Experiments were carried out in triplicates and the average results are reported herein.

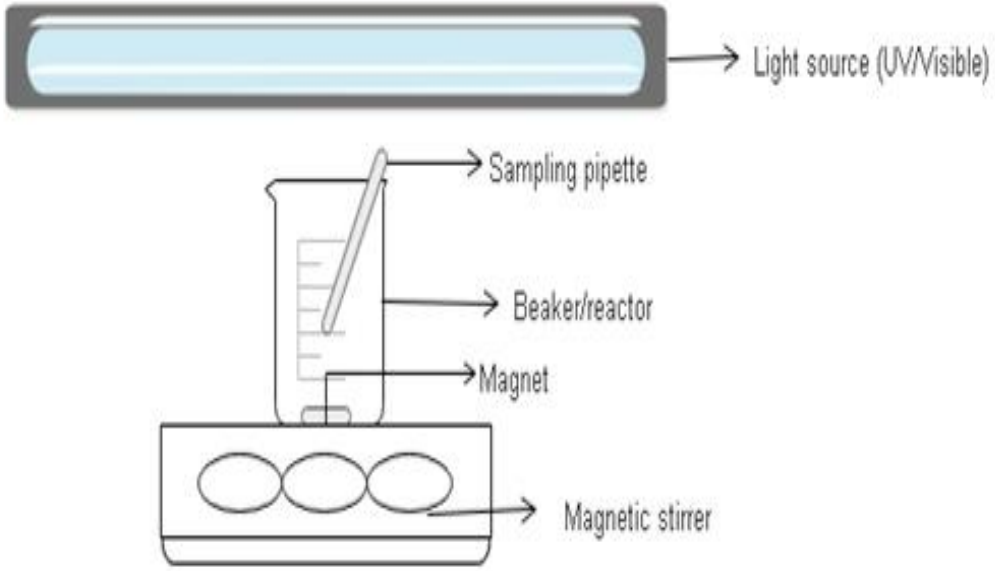

Figure 3.2: Batch experimental setup

3.5. Analytical methods

3.5.1. High pressure liquid chromatography (HPLC)

Phenol concentration before and after degradation were monitored on a Waters HPLC (Waters 2695 separation module) with a photo diode array – Waters 2998 PDA detector. Phenol was separated on a Waters PAH C18 (4.6 ×250 mm, 5 µm) column and Empower software for data analysis. Mobile phase consisted of two solvents A and B where A consists of 1% acetic acid in water and B consists of 1% acetic acid in acetonitrile. Phenol elution was done at 30% A and 70% B with operating conditions listed in Table 3.1. Phenol concentration was determined from calibration curves of prepared standards.

Table 3.1: HPLC operating conditions

Flow rate	1.2 mL/min
Injection volume	5 µL
Column temperature	30^0C
Wavelength	280 nm

Prior to HPLC analysis, the column was conditioned for 10 min, purged for 6.5 min and equilibrated for 10 min before sample sets were analysed. This was done to ensure that the column is primed and ready for analysis and has no contaminants. HPLC vials were washed thoroughly, rinsed with ultra-pure water and oven dried before use.

3.5.2. Total organic Carbon (TOC)

The extent of mineralisation was followed by determining the TOC before and after exposure of the phenol solution to photocatalytic conditions. The rate of removal of TOC was measured using a Shimadzu TOC-V analyser to determine the extent of mineralisation. The mobile phases include a persulfate oxidizer solution and a phosphoric acid solution. TOC analysis requires more sample volume in comparison to the HPLC analysis. 35 mL of samples were taken before and after irradiation. This samples were centrifuged and filtered with a 0.45 µm syringe filter (Millipore) before analysis. A blank ultra-pure water vial was always scheduled to run first before the samples were analysed to ensure that no contaminants in the TOC injectors and tubes.

CHAPTER 4

CHARACTERISATION OF PHOTOTCATALYSTS

The successfully synthesised photocatalyts were characterised using various techniques. This was done to validate the synthesis route and study the physicochemical properties of the synthesised materials. In this chapter, a general and in-depth material characteristics investigation was done which includes x-ray diffraction (XRD), X-ray photoelectron spectroscopy (XPS), Fourier-transform infrared (FTIR) spectroscopy, scanning electron microscopy (SEM), thermogravimetric analysis (TGA), zeta potential and hydrodynamic diameter measurements, ultraviolet-visible spectroscopy and band gap measurements.

4.1. X-ray diffraction (XRD)

The purity and crystallinity of the synthesised particles were investigated by XRD analysis. Figure 4.1 shows the diffraction peaks for BiOCl, AgCl/BiOCl and Ag/AgCl/BiOCl. No other diffraction peaks were detected which points to the high purity of prepared samples. The XRD patterns did not suggest the presence of metallic Ag in the ternary Ag/AgCl/BiOCl photocatalyst as the spectra for AgCl/BiOCl and Ag/AgCl/BiOCl are exactly the same. The XRD beam is known to have a sample penetration depth of ~ 2 to 3 µm (Xu et al., 2019). This is larger than the typical size of silver nanoparticles (2 nm – 100 nm) (Zhang et al., 2016) that were expected to form on the catalyst surface. Therefore, XRD could not be able to establish the presence of Ag^0 especially at very low concentrations of Ag^0. Additionally, high disparity of metallic Ag and low crystalline composition of the Ag^0 are other reasons why Ag^0 was not detected. Peaks at 2θ = 32.2˚, 55.2˚ and 67.8˚ are indexed to the AgCl pattern and corresponds to (200), (311) and (222) khl planes (Al Aboody, 2019). This shows the coexistence of both AgCl and BiOCl phases.

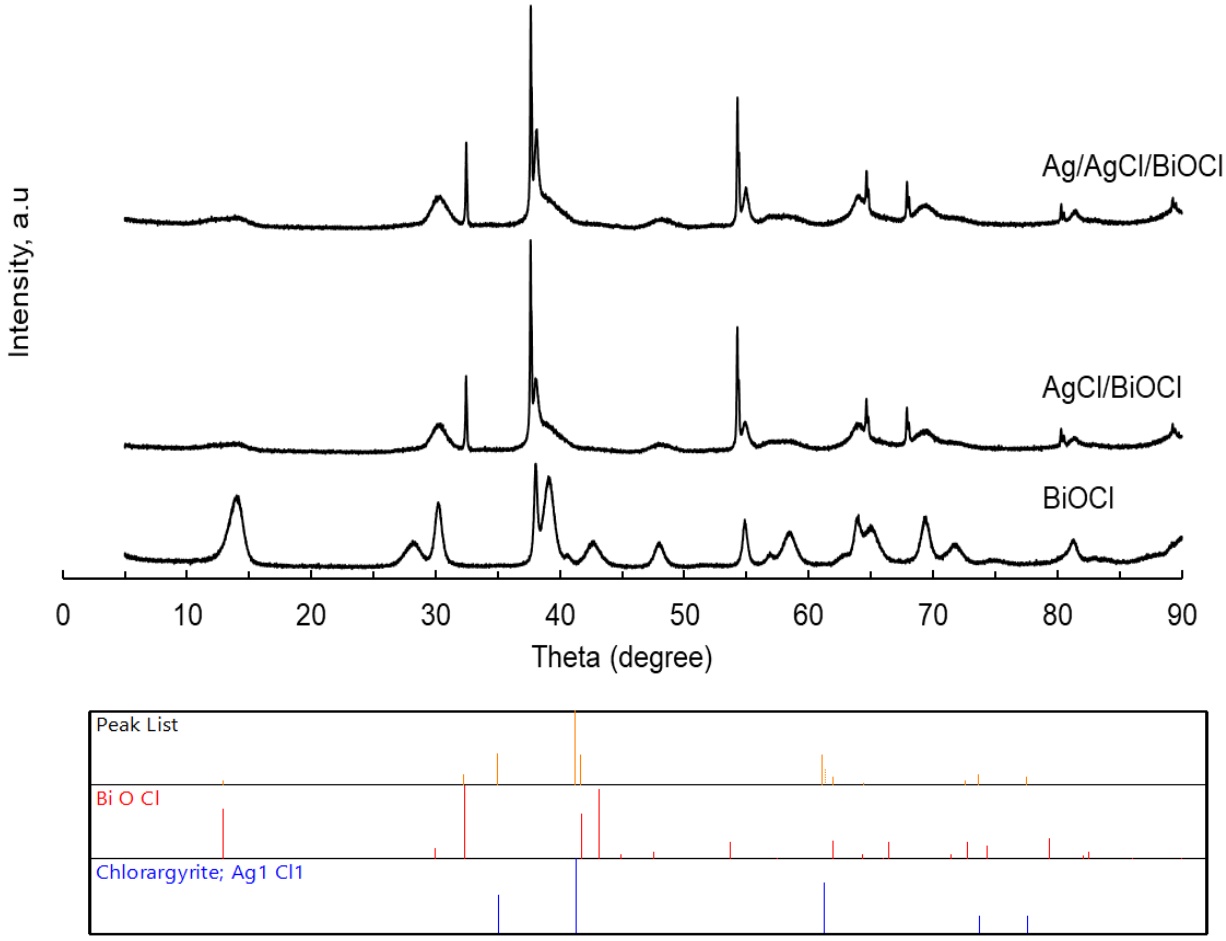

Figure 4.1: XRD spectra for synthesised BiOCl, AgCl/BiOCl and Ag/AgCl/BiOCl

During the synthesis process, a colour change was noticed from white to purple after irradiation as seen in Figure 4.2. This colour change confirms the presence of Ag in the composite catalyst (Hong et al., 2017) which can be attributed to the surface plasmon resonance (SPR) of Ag^0 nanoparticles (Ao et al., 2014).

Figure 4.2: AgCl/BiOCl (before irradiation) and after Ag/AgCl/BiOCl (irradiation)

4.2. X-ray photoelectron spectroscopy (XPS)

XPS measurements were carried out to determine the chemical compositions and specify the chemical states of elements present in the synthesised catalysts. This was accomplished by measuring the kinetic energy of electrons deflected from the surface of the catalyst. Figure 4.3 shows the XPS spectra of Ag/AgCl/BiOCl while Figure 4.4 shows the peaks of the different elements present. Two strong peaks at 158.3 eV and 164 eV in the ternary Ag/AgCl/BiOCl composite can be ascribed to the Bi $4f_{7/2}$ and Bi $4f_{5/2}$ of Bi^{3+} which is a symbol of the Bi^{3+} in BiOCl. The peak at 367.1 eV corresponds to Ag $3d_{5/2}$. Cui et al. (2017) suggests that the peaks at 367.1 eV is attributed to Ag^{+} in AgCl and the peak just beside it at 374 eV is assigned to metallic Ag which is as a result of photoreduction of Ag^{+} to Ag^{0}. This confirms that elemental silver was indeed present after irradiation. The peak at 530.4 eV corresponds to O 1s which is the Bi-O in BiOCl and peak at 197.8 eV corresponds to Cl $2p_{3/2}$. The carbon peak present at 284.9 eV is C 1s which is ascribed to the presence of accidental/adventitious carbon species.

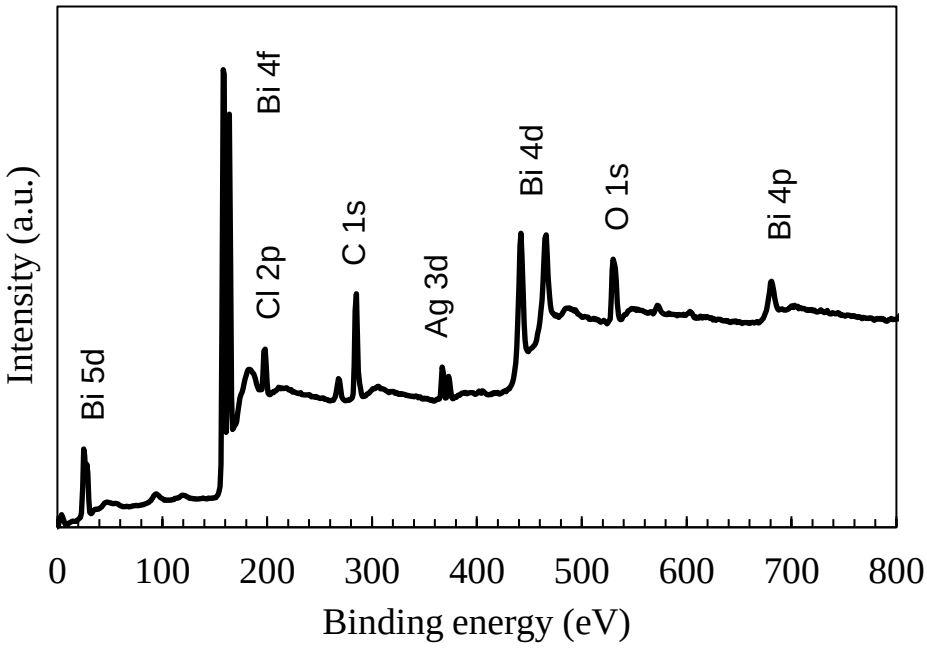

Figure 4.3: XPS spectra of Ag/AgCl/BiOCl ternary composites

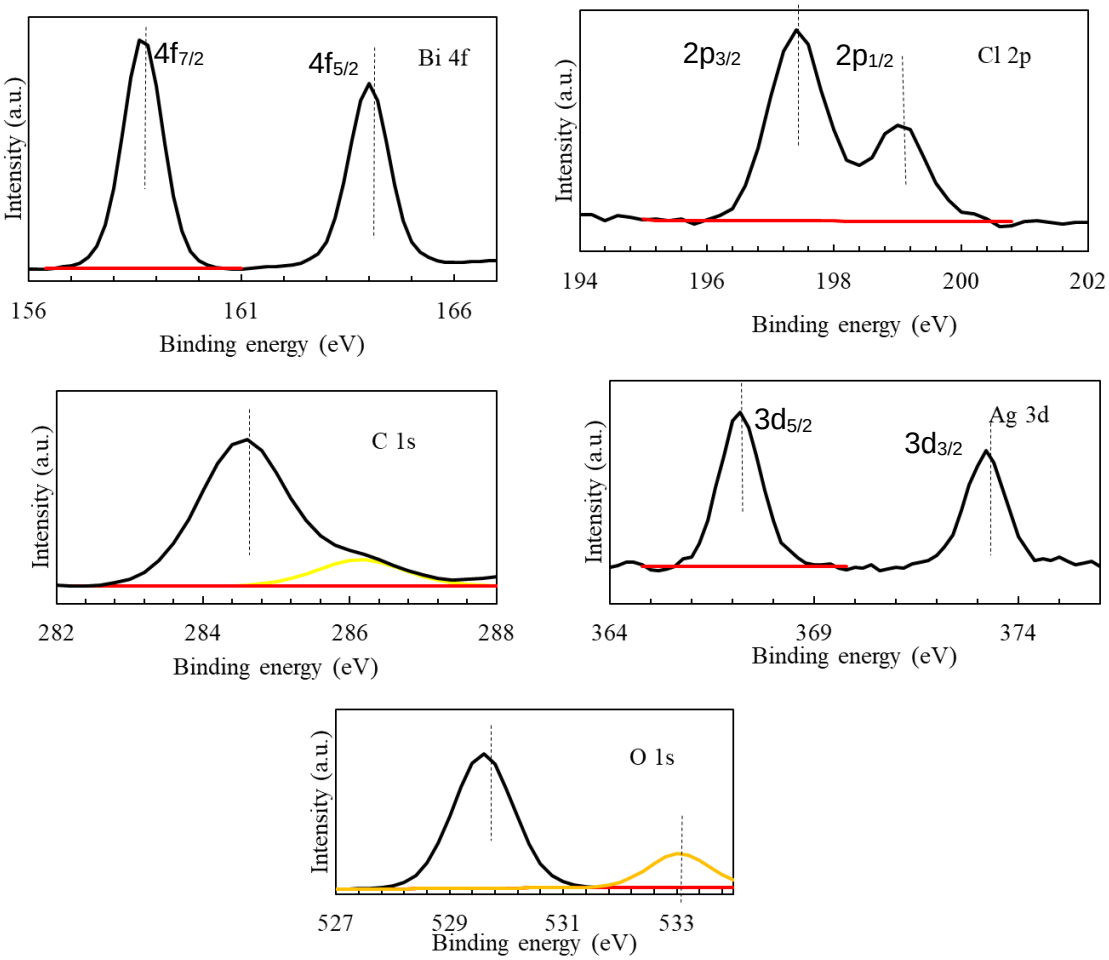

Figure 4.4: Bi 4f, Cl 2p, C 1s, Ag 3d and O 1s in Ag/AgCl/BiOCl XPS spectra

The XPS spectra for the binary composite AgCl/BiOCl is shown in Figure 4.5 while the XPS of the elemental components are shown in Figure 4.6. The catalyst contains the same elements as found in the ternary composite. The peak at 367.3 eV is ascribed to Ag 3d, peak at 198 eV to Cl 2p, peak at 158.8 eV to Bi 4f, peak at 530.4 eV to O 1s and peak at 285 eV to C 1s.

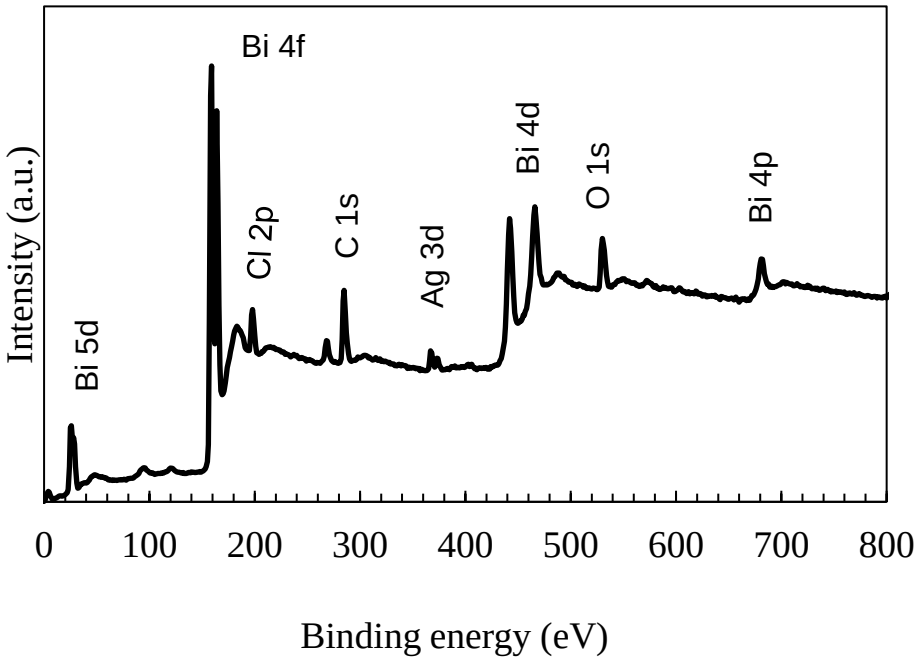

Figure 4.5: XPS spectra of AgCl/BiOCl

The intensity of the Ag peaks present in Ag/AgCl/BiOCl and AgCl/BiOCl were compared and shown in Figure 4.7 and show that the synthesised Ag/AgCl/BiOCl shows high intensity peaks at both $3d_{5/2}$ and $3d_{3/2}$ pointing to the presence of metallic Ag on the surface of the catalyst in the ternary composite. The presence of elemental Ag^0 in the binary composite was most likely due to the unintended irradiation of the AgCl by visible light during sample preparation and transfer.

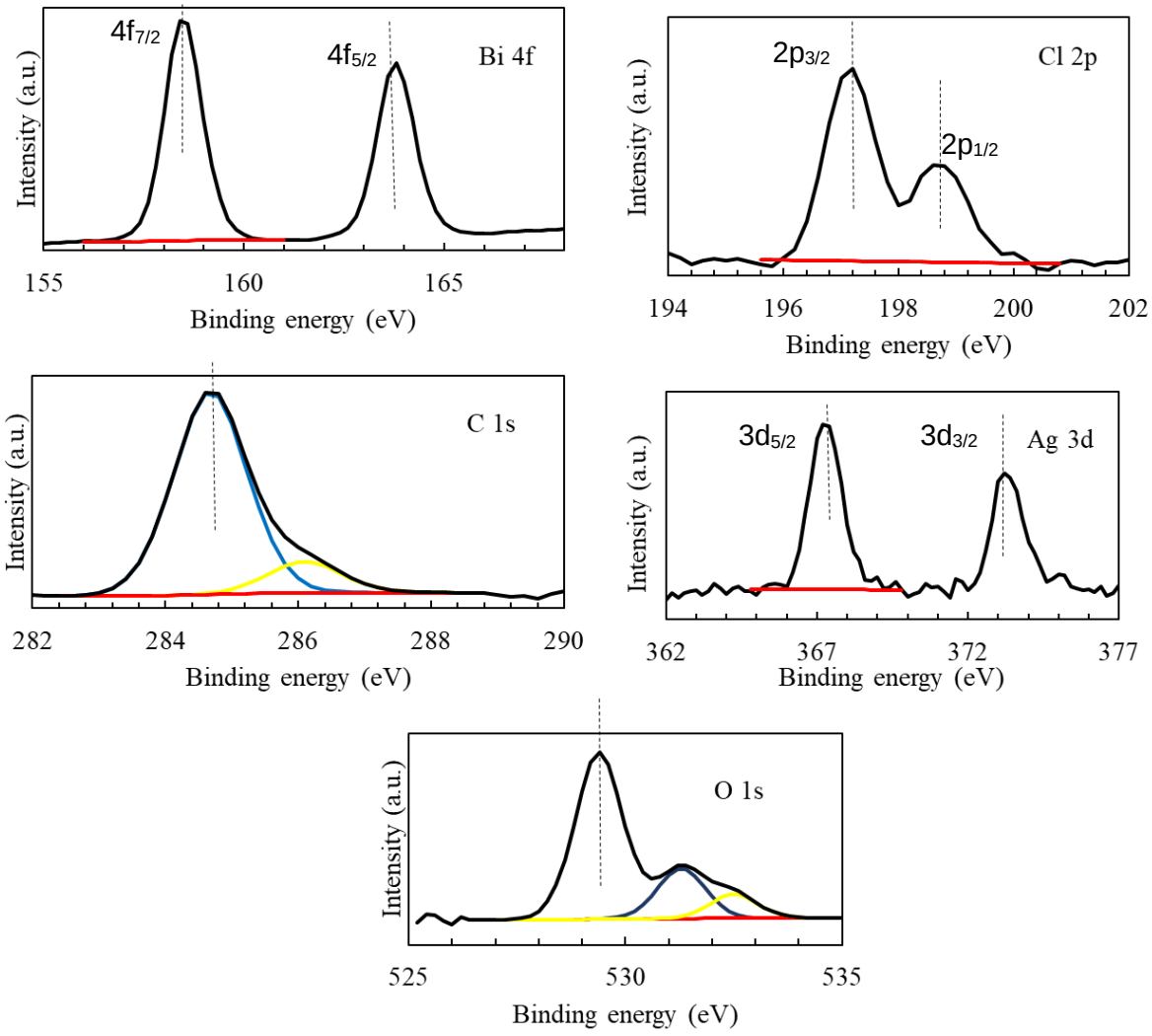

Figure 4.6: Bi 4f, Cl 2p, C 1s, Ag 3d and O 1s in AgCl/BiOCl XPS spectra

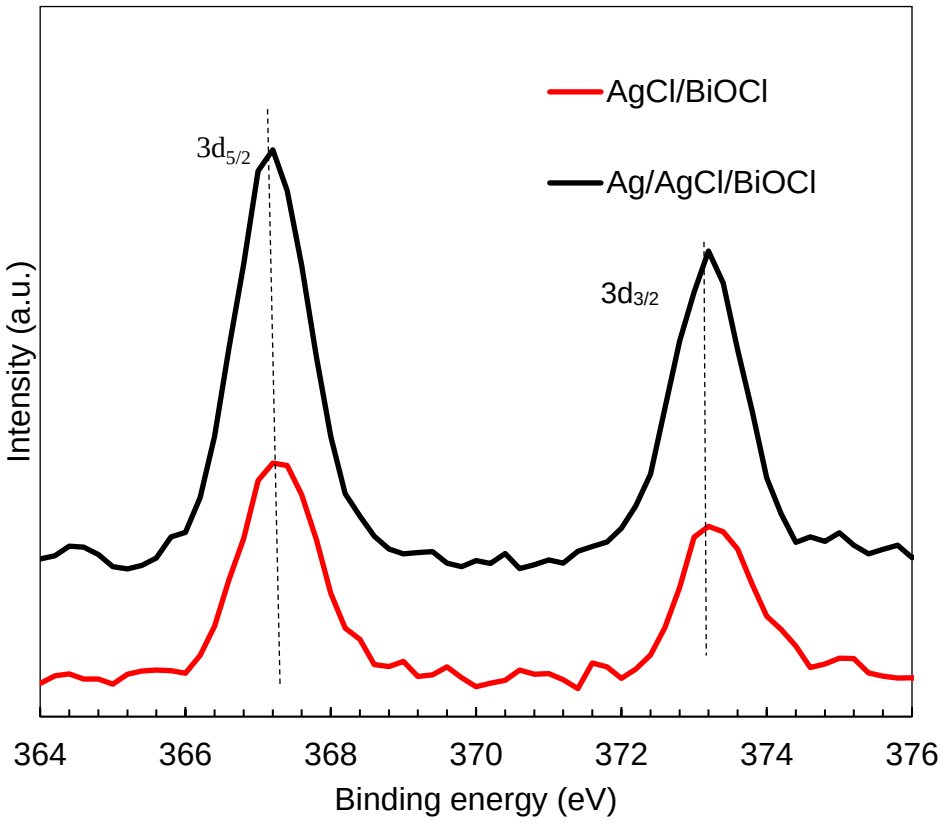

Figure 4.7: Ag 3d spectra for AgCl/BiOCl and Ag/AgCl/BiOCl

The XPS spectra for BiOCl are shown in Figure 4.8 and that of its elemental components is shown in Figure 4.9 and it shows the co-presence of Bi, O, C and Cl. The presence of the C peak is as a result of adventitious carbon found on the surface of the catalyst which comes from the CTAC during the synthesis process. The Bi 4f shows intense peaks at 158.3 eV and 164 eV which is assigned to Bi $4f_{7/2}$ and Bi $4f_{5/2}$ respectively. The Cl 2p peaks are located at 197.8 eV while the band at 530.1 eV is attributed to the coordination of oxygen (Cui et al., 2018).

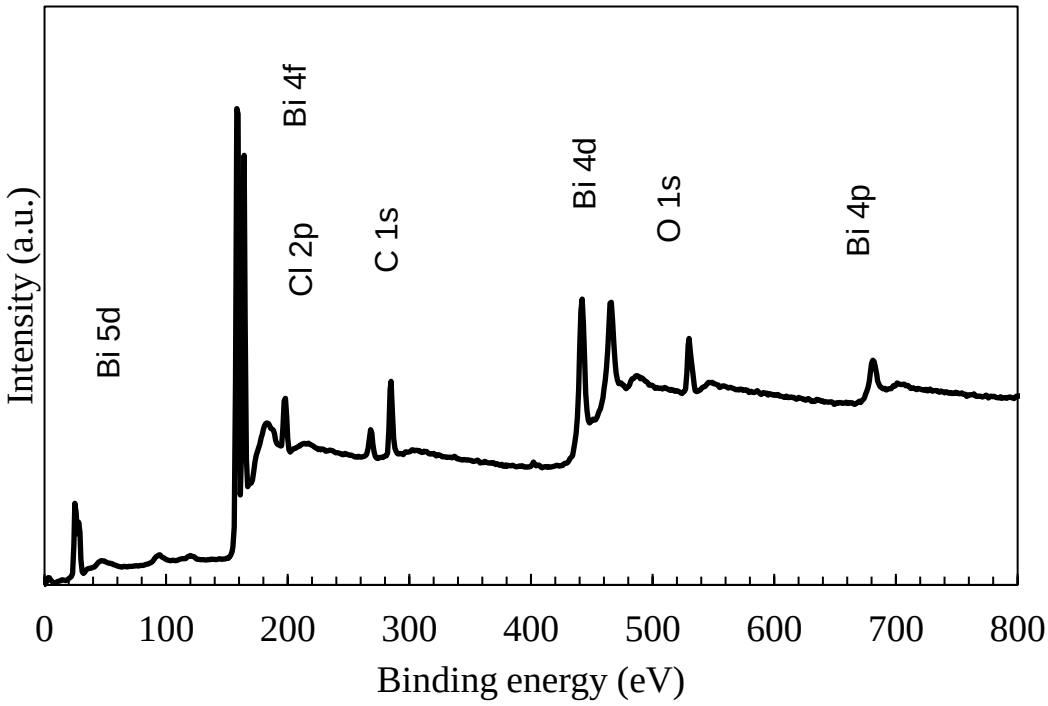

Figure 4.8: XPS spectra for BiOCl

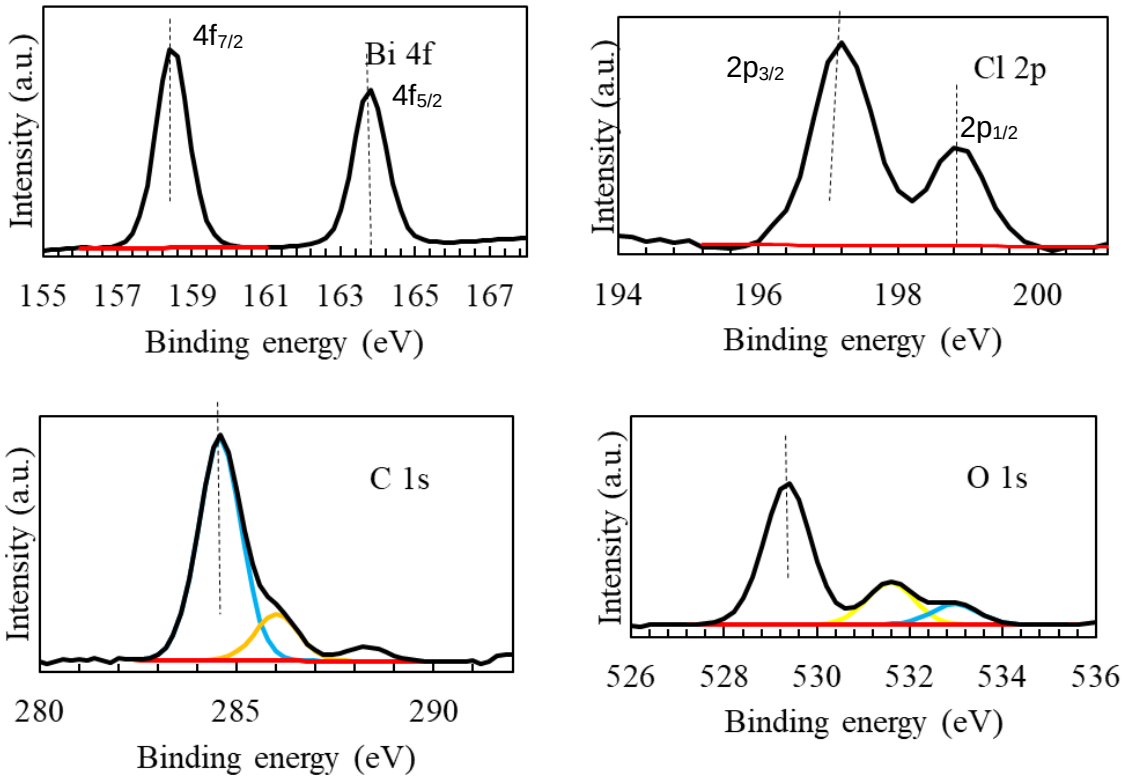

Figure 4.9: Bi 4f, Cl 2p, C 1s, and O 1s in BiOCl XPS spectra

Figure 4.10 shows the XPS spectrum of AgCl where the peaks of Ag, Cl, C and O can be detected and illustrated in Figure 4.11.The Ag bands at 367.1 eV and 373 eV corresponds to the Ag $3d_{5/2}$ and $3d_{3/2}$ binding energies respectively. The Cl 2p band is displayed at 197.9 eV.

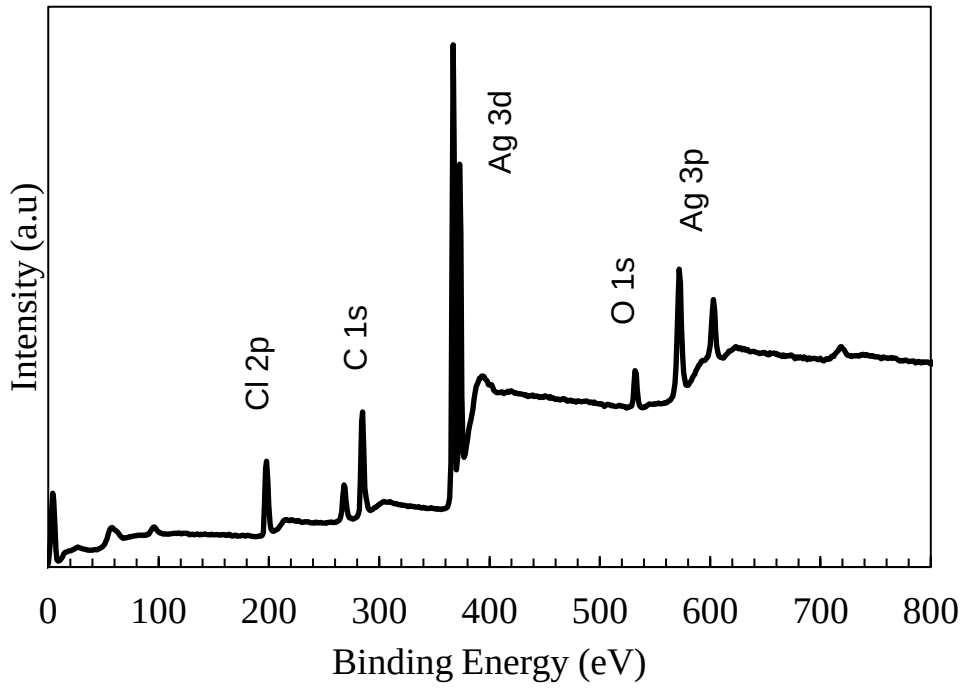

Figure 4.10: XPS spectra for AgCl

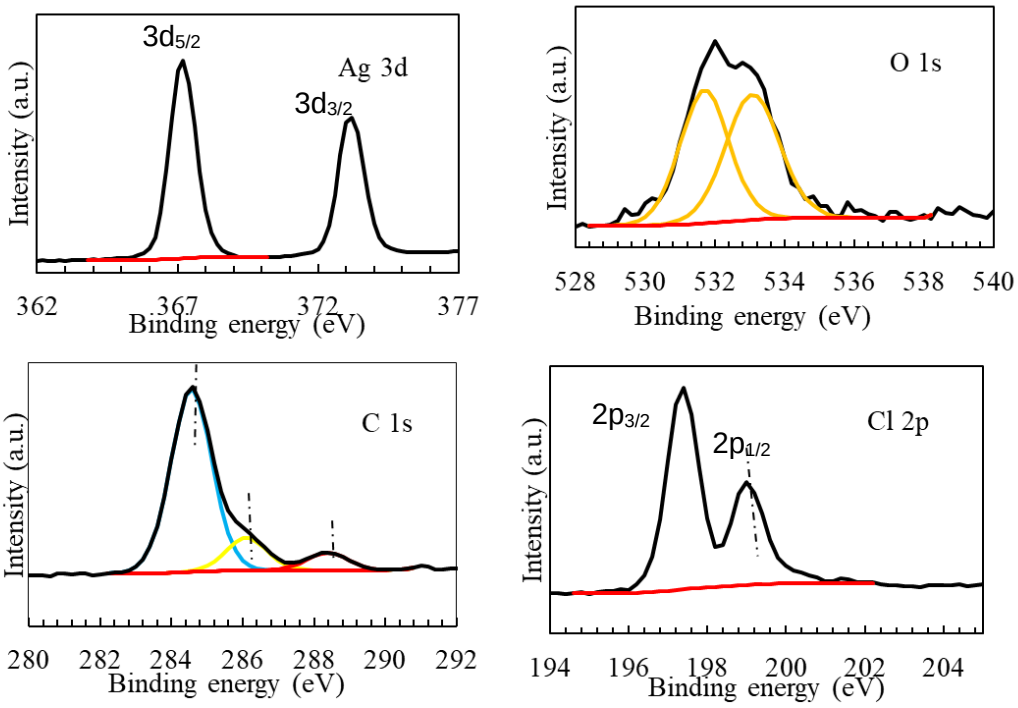

Figure 4.11: Cl 2p, C 1s, Ag 3d and O 1s in AgCl XPS spectra

4.3. Fourier-transform infrared (FTIR) spectroscopy

Fourier-transform infrared spectroscopy (FTIR) was carried out on the synthesised particles to determine the functional groups present. Figure 4.12 illustrates the FTIR spectra of AgCl, BiOCl, AgCl/BiOCl and Ag/AgCl/BiOCl. The signal at 3400 cm^{-1} – 3500 cm^{-1} points to O-H group which is as a result of the interactions with water. 2923 cm^{-1} and 1357 cm^{-1} are carboxyl and alkanes group signals which are as a result of remnants from the synthesis process such as CTAC and acetic acid (Singh et al., 2018). The band at 550 cm^{-1} is attributed to the Bi-O functional group which is a characteristic and present in BiOCl, AgCl/BiOCl and Ag/AgCl/BiOCl. This observation confirms the results that were obtained from the XPS results which also shows the presence of carbon on the particle surface.

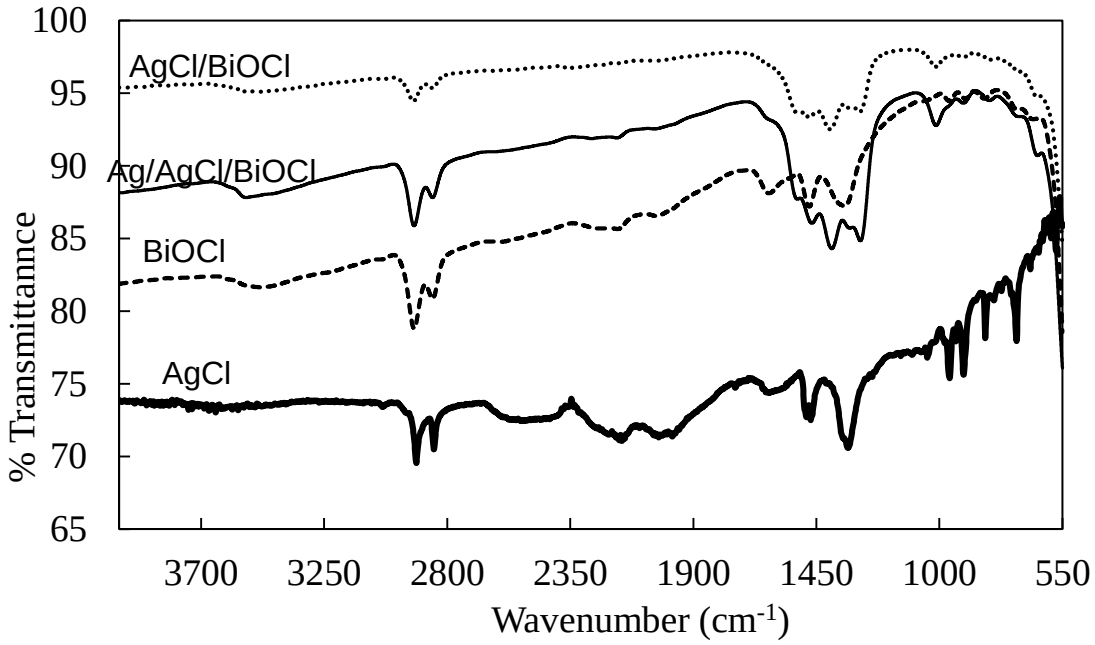

Figure 4.12: FTIR spectra of synthesised catalysts

4.4. X-ray fluorescences (XRF)

The elemental composition and purity of the synthesised catalysts were analysed and reported in Table 4.1. All components of the materials adds up to above 99.9% which shows highly pure materials were synthesised. All synthesised catalysts have similar

Cl composition while BiOCl differs from AgCl/BiOCl and Ag/AgCl/BiOCl with respect to the absence of Ag.

Table 4.1: X-ray florescence data for synthesised materials

	STANDARD					
	BHVO-1 STD	BHVO-1 Analysed	Ag/AgCl/BiOCl	AgCl/BiOCl	BiOCl	TiO_2
TiO_2	2.71	2.50	<0.01	<0.01	<0.01	99.04
Cl	-	-	19.70	19.97	19.04	0,12
Ag_2O	-	-	20.47	22.17	<0.01	<0.01
Bi_2O_3	-	-	58.66	56.49	79.75	0.04
TOTAL	100.69	99.90	99.98	99.95	99.94	99.97

4.5. Scanning electron microscopy/ energy dispersive x-ray spectroscopy (SEM/EDS)

SEM images of the obtained AgCl, BiOCl, AgCl/BiOCl and Ag/AgCl/BiOCl samples are shown in Figure 4.13. AgCl was observed to possess near-spherical particle morphology. Figure 4.14a shows a wide area view of the synthesised AgCl while Figure 4.14b shows a zoomed in image of the particles suggesting that the AgCl particles also showed a propensity to form agglomerates and the particle size varied from nanometer to the micro range.

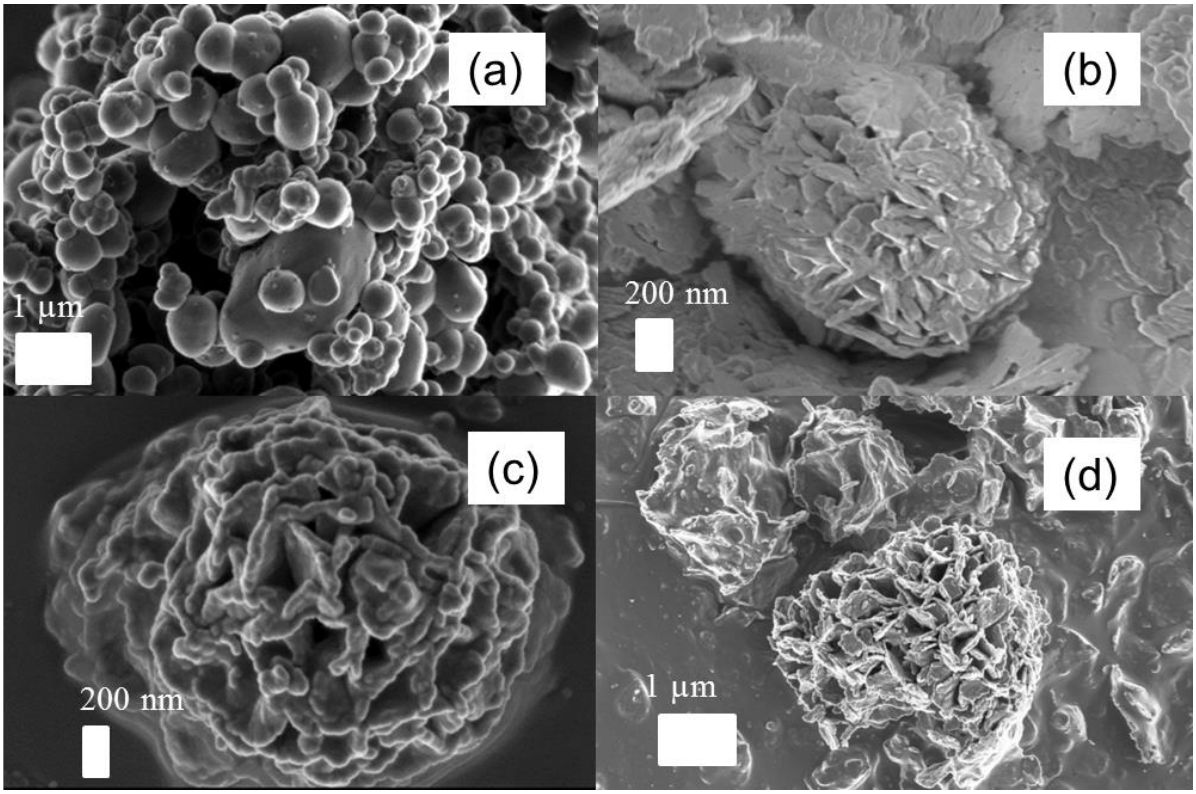

Figure 4.13: SEM (a) AgCl, (b) BiOCl (c) AgCl/BiOCl and (d) Ag/AgCl/BiOCl

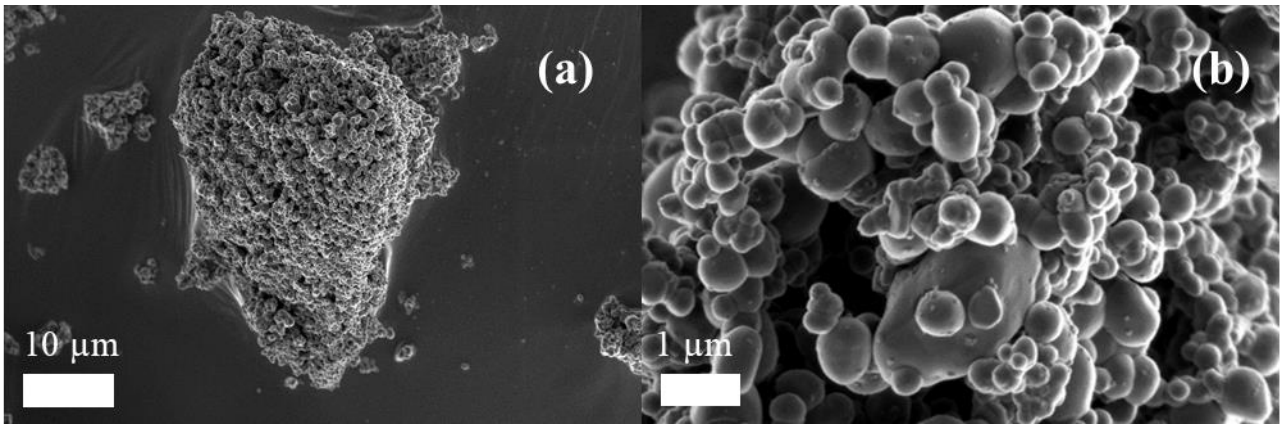

Figure 4.14: SEM images of AgCl

Figure 4.15 show the SEM image of the synthesised BiOCl particles consisting of many rod-like microspheres assembled to form flat two-dimentional (2D) nanosheets.

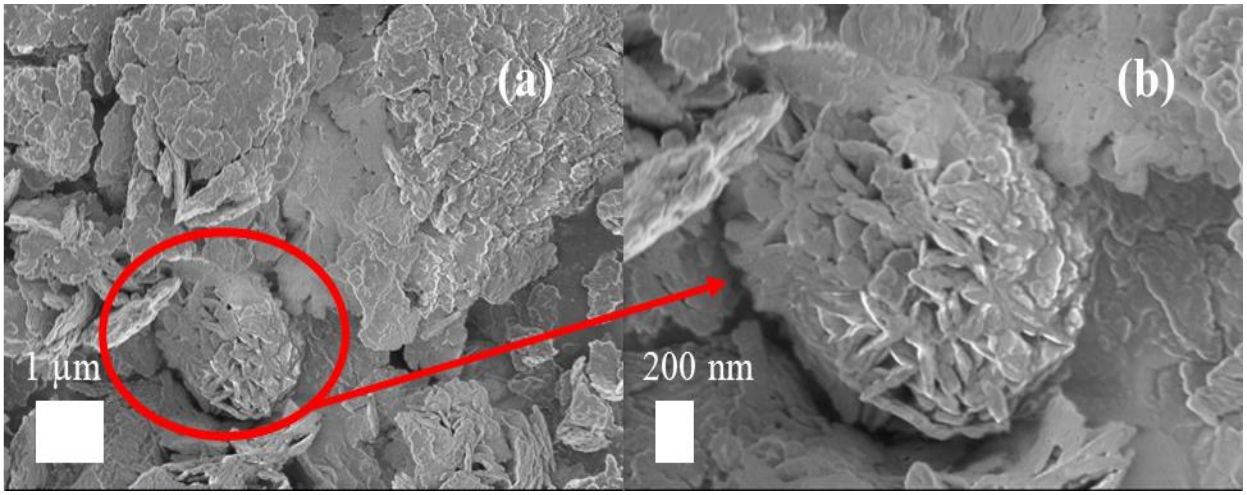

Figure 4.15: SEM images of BiOCl

SEM images for the synthesised AgCl/BiOCl illustrated in Figure 4.16 shows a three-dimentional (3D) microstructure of BiOCl with particle-like AgCl attached on the surface. The morphology and microstructure of the ternary phase Ag/AgCl/BiOCl remains the same before irradiation (Figure 4.16b) and after irradiation (Figure 4.17b) which shows that the synthesised particles are stable. Ag/AgCl/BiOCl consists of many flower-like structures (Figure 4.17b).

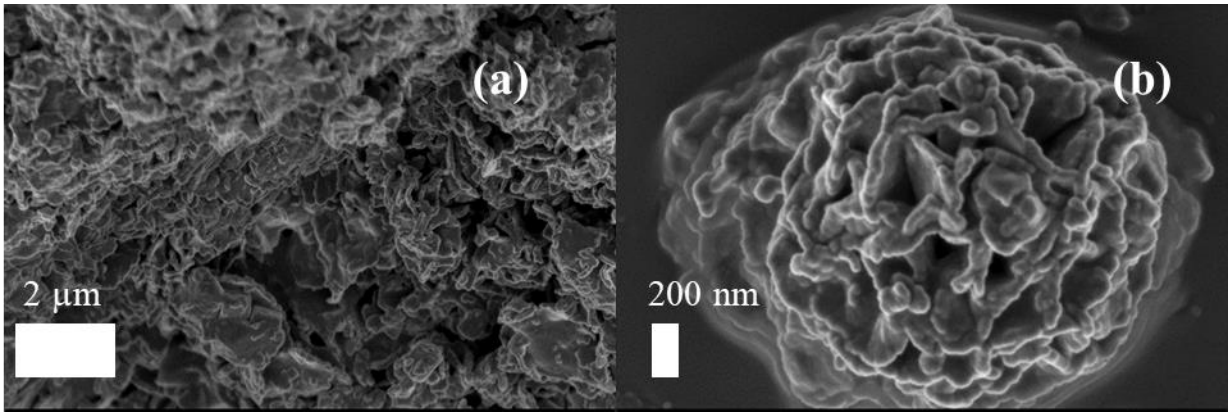

Figure 4.16: SEM images of AgCl/BiOCl

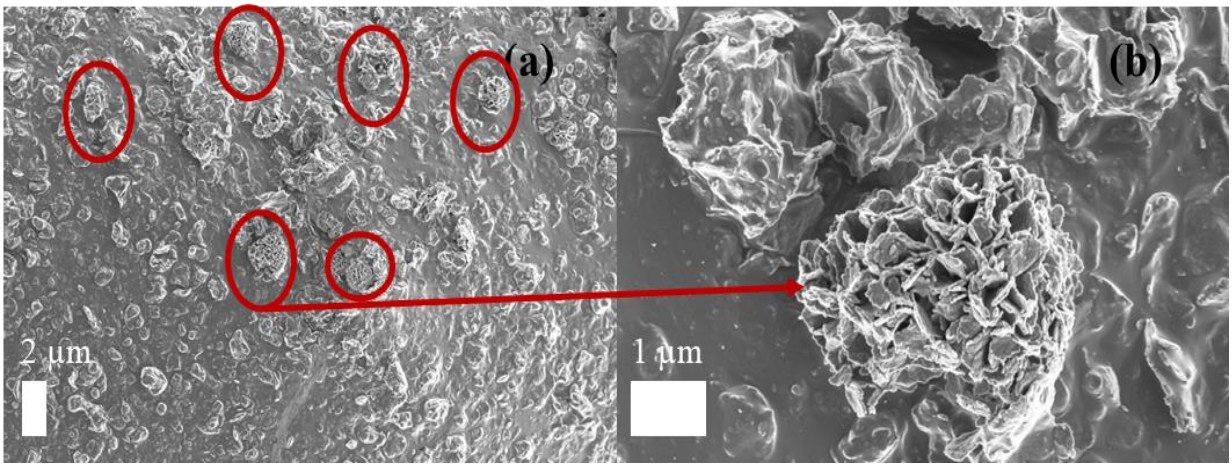

Figure 4.17: SEM image of Ag/AgCl/BiOCl

The layered structures of the synthesised catalysts also play a role in the photodegradation of organic pollutants. They provide enough space for polarisation of atoms and orbitals thereby effectively separating the photogenerated holes and electrons which enhance their photocatalytic activity (Sun et al., 2014).

The elemental compositions of the as-synthesised particles were estimated by an EDS analysis. The EDS spectra corresponding to these mappings are illustrated in Figure 4.18. The EDS spectra confirm the presence of Ag, Cl, Bi, and O in the synthesised photocatalyst composite materials.

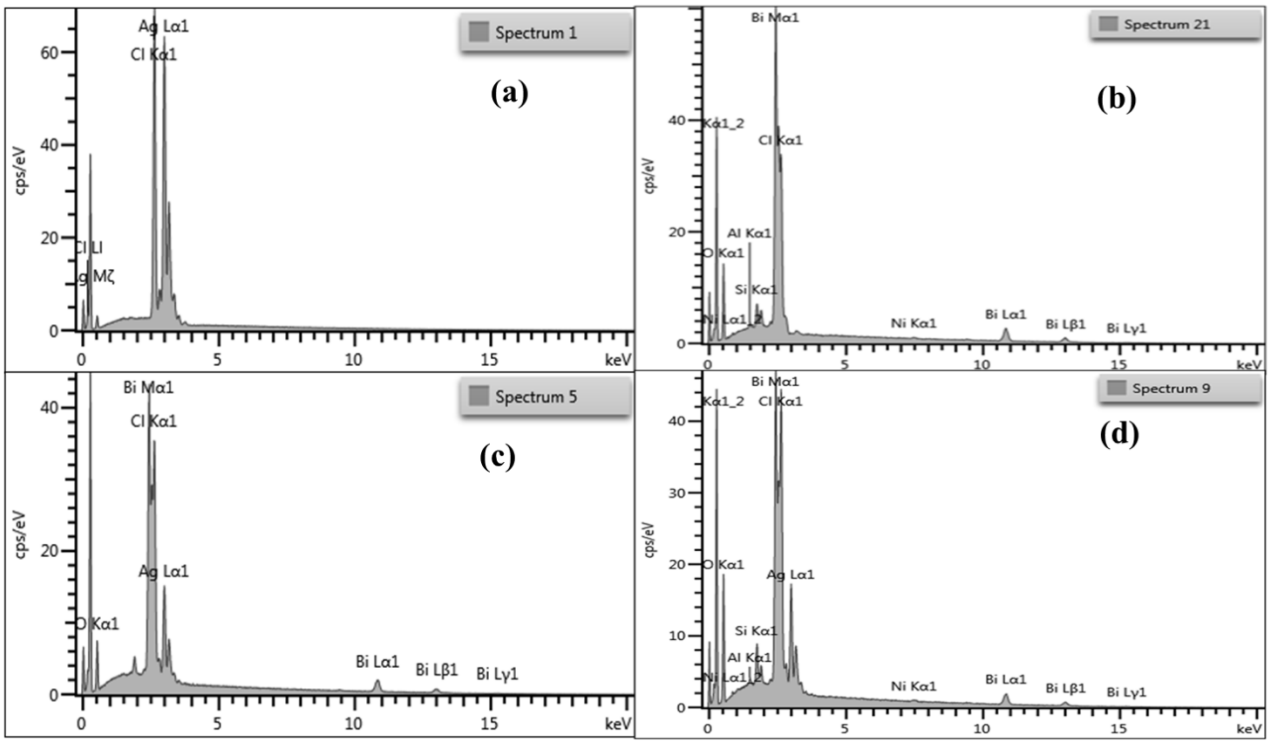

Figure 4.18: EDS mapping of (a) AgCl, (b) BiOCl, (c) AgCl/BiOCl, (d) Ag/AgCl/BiOCl

AgCl

Table 4.2 shows the percentages of individual elements Ag and Cl in the compound AgCl. The atomic percentage of Ag:Cl of 51.54:48.46 corresponds to an approximate 1:1. This shows that AgCl was indeed formed.

Table 4.2: AgCl atomic and weight composition

Element	Wt%	Wt% Sigma	Atomic %
Cl	23.60	0.10	48.46
Ag	76.40	0.10	51.54

BiOCl

The atomic and elemental composition of the synthesised BiOCl catalysts is shown in Table 4.3. The Bi to O ratio is an approximate 1:1 while a high percentage of oxygen atoms are present in the synthesised catalyst.

Table 4.3: BiOCl atomic and weight composition

Element	Wt%	Wt% Sigma	Atomic %
O	17.86	0.09	60.48
Cl	12.24	0.06	18.69
Bi	65.77	0.17	17.05

AgCl/BiOCl

Table 4.4 and Figure A4 shows the atomic and weight percentage and elemental mapping of the synthesised AgCl/BiOCl. The ratio of Ag:Bi:Cl are seen to be in the correct stoichiometric ratio of 1:1:2 while atomic oxygen is noticed to be in excess which is consistent with the synthesised BiOCl photocatalyst.

Table 4.4: AgCl/BiOCl atomic and weight composition

Element	Wt%	Wt% Sigma	Atomic %
O	15.95	0.14	54.01
Cl	14.91	0.08	22.79
Ag	21.74	0.14	10.92
Bi	47.40	0.18	12.29

Ag/AgCl/BiOCl

Ag/AgCl/BiOCl elemental, atomic and weight composition are reported in Table 4.5. The atomic ratio of Ag:Bi:Cl in the synthesised particles are in correct stoichiometric ratio while the amount of atomic oxygen present is still consistently high and was previously noticed in the synthesises BiOCl and AgCl/BiOCl. The high amounts of O-atoms in the synthesised BiOCl, AgCl/BiOCl and ternary- Ag/AgCl/BiOCl points to the presence of oxygen vacancies. These oxygen-vacancies in semiconductors have been proved to act as active sites which consequently enhance the rate of carrier separation while narrowing the bandgap which improves the efficiency of the photocatalytic activity (Zhao et al., 2018b).

Table 4.5: Ag/AgCl/BiOCl atomic and weight composition

Element	Wt%	Wt% Sigma	Atomic %
O	18.86	0.17	57.83
Cl	14.32	0.09	19.82
Ag	21.46	0.15	9.76
Bi	43.90	0.21	10.31

4.6. Thermogravimetric analysis (TGA)

The result of the thermal analysis for the synthesised photocatalysts AgCl, BIOCl, AgCl/BiOCl and Ag/AgCl/BiOCl were illustrated in Figure 4.19. For temperature up to 100 ℃, there is weight loss due to loss of adsorbed moisture and gases. In AgCl, the particles was stable and has negligible weight loss until 700ºC before thermal decomposition occurred. For BiOCl, decomposition occurred in various stages and between 25^0C – 270^0C, weight loss of approximately 10% due to the removal of residual and interlayer water molecules. Distinctive weight loss for BiOCl starts at 550^0C.

The TGA curves for AgCl/BiOCl and Ag/AgCl/BiOCl are super imposed on each other which points to a similar thermal degradation profile for both compounds. A weight loss of 10% was measured at 440ºC in both the binary and ternary catalyst which is associated with loss due to water molecules, a 14% weight loss was noticed between 440^0C and 550^0C. It can be noticed that at 1000^0C, while AgCl is completely decomposed, BiOCl has 80% thermal decomposition. The binary and ternary composite measures 62% decomposition. This shows that AgCl and BiOCl decomposes earlier in comparison to the synthesised AgCl/BiOCl and Ag/AgCl/BiOCl composites.

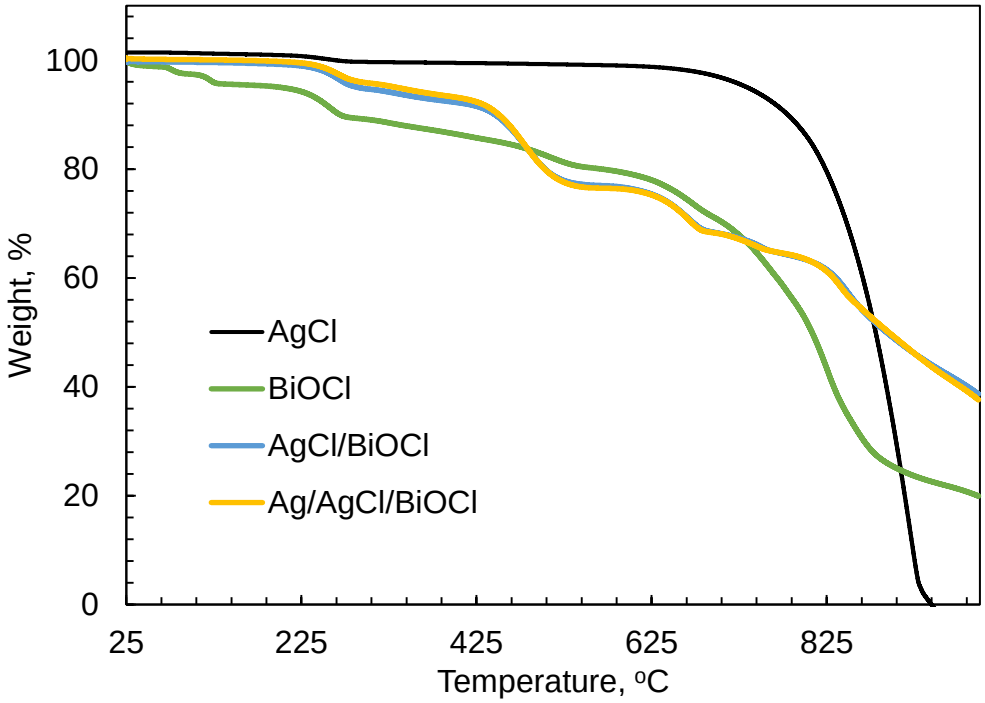

Figure 4.19: TGA curves of as-synthesised particles

4.7. Brunaer-Emmett-Teller method (BET)

The BET surface area and pore size distribution of the prepared Ag/AgCl/BiOCl were investigated using nitrogen adsorption desorption measurements. During photocatalysis, the surface area of the particle is an important factor that affects the efficiency of photodegradation process as an increase in surface area, improves the rate of the reaction due to the presence of more active sites. The N_2 desorption-desorption isotherm is shown in Figure 4.20

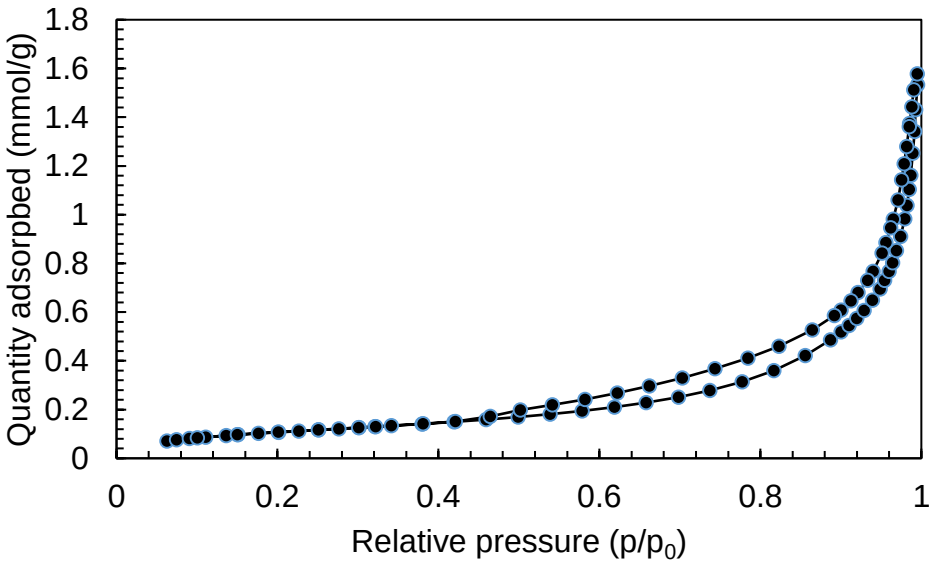

Figure 4.20: N_2 adsorption-desorption isotherm of Ag/AgCl/BiOCl

The BET surface area was measured to be 6.6448 m^2/g with a pore volume of 0.0187 cm^3/g and a pore size of 7.0457 nm. The nitrogen adsorption isotherm confirms a type IV isotherm (Cychosz and Thommes, 2018) which makes the ternary composite a mesoporous material with a type H3 hysteresis loop (Sing and Williams, 2004).

4.8. Zeta potential and Hydrodynamic diameter (HDD)

Zeta potential is measured to quantify the magnitude of the surface charge of particles dispersed in a solution (Zhao et al., 2018a). Figure 4.21 shows the zeta potential and HDD of synthesised ternary Ag/AgCl/BiOCl which was measured at different pH values ranging from 2 to 12.

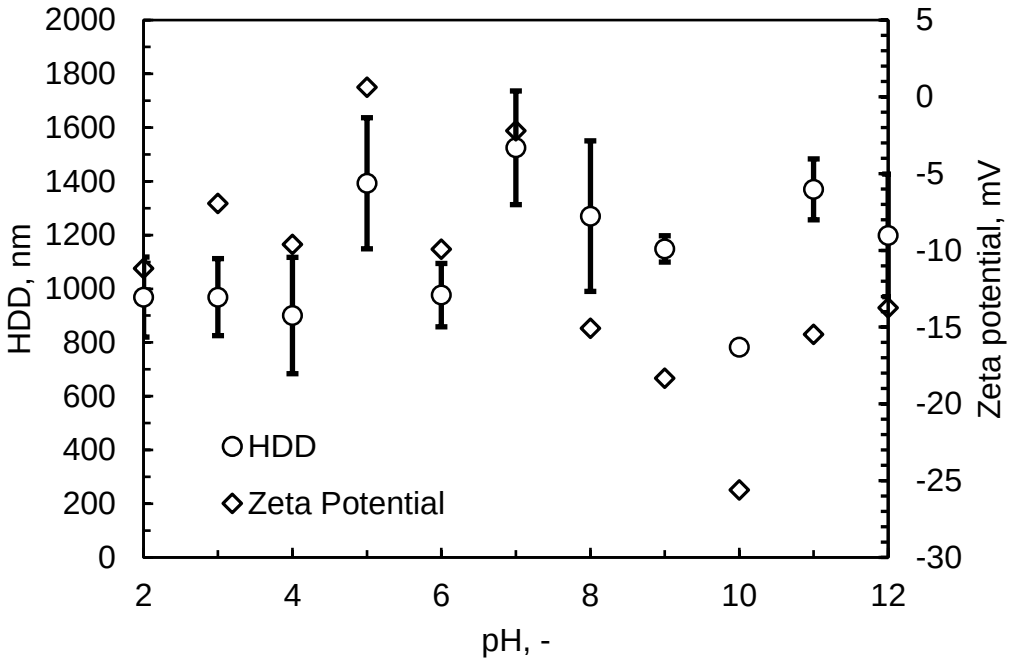

Figure 4.21: Ag/AgCl/BiOCl zeta potential and HDD measurements

The surface of Ag/AgCl/BiOCl is negatively charged all through the pH spectrum as the measured zeta potential is below 0 mV with a slightly positive zeta potential of 0.63 mV at pH 5. This point is noted to be the point of zero charge of the synthesised particles. At this point, the surface of the synthesised Ag/AgCl/BiOCl is at its neutral state. The hydrodynamic diameter measured for the ternary catalyst in different pH solutions varied slightly but averaged at about 1000 nm across the pH range.

4.9. Ultraviolet – visible spectroscopy and bandgap measurement

The UV-vis absorption spectra of the synthesised catalysts are shown in Figure 4.22. This was done to investigate the optical properties of the obtained particles. The band-gap and electronic state of semiconductor photocatalysts are of great importance in order to determine its catalytic efficiency and photoabsorption potential. All as-synthesised catalysts, AgCl, BiOCl, AgCl/BiOCl and Ag/AgCl/BiOCl exhibited absorption in the UV range. More importantly, the photoabsorption of AgCl/BiOCl is seen to be broadened in the visible light range in comparison to the other synthesised photocatalyst. This is closely followed by Ag/AgCl/BiOCl and BiOCl. AgCl did not show

good photoabsorption in the visible light range. This shows that coupling AgCl with BiOCl improves the photoabsorption of the composite in the visible light range in comparison with the individual compounds.

The absorption of a crystalline semiconductor near the band edge can be calculated by the Kubelka-Munk equation (Daupor and Wongnawa, 2014) shown in Equation 13:

$$(ahv) = A(hv - E_g)^{n/2} \quad (13)$$

The optical bandgap of the catalysts can then be evaluated on the Tauc plots which is a graph of $(ahv)^2$ vs hv where,

a = absorption coefficient
h = plank constant
v = light frequency
E_g = bandgap
A = constant
hv (photon energy) = 1240/ wavelength

For direct allowed transition, n = 1 (Li et al., 2017a). For BiOX, the value of n = 4 for indirect transition (Cheng et al., 2014). By extrapolating the linear portion for the Tauc plots to zero, the bandgap energy of the synthesised catalysts can be estimated (Liu et al., 2017) and is shown in Figure 4.23, Figure 4.24, Figure 4.25, and Figure 4.26. AgCl and BiOCl has a similar absorption edge at about 231 eV and while AgCl shows an absorption intensity in the UV range, this is absent in the visible light range. In comparison to the other synthesised catalysts, AgCl/BiOCl shows the highest absorption abilities in the visible light region which is followed by the ternary catalyst, Ag/AgCl/BiOCl. The estimated band gaps for the synthesised catalysts are 5.6 eV for AgCl, 5.4 eV for BiOCl, 3 eV for AgCl/BiOCl and 2.9 eV for Ag/AgCl/BiOCl. It is noticed that while AgCl and BiOCl has a high measured band-gap that points at its unsuitability for visible light activation, the coupled binary AgCl/BiOCl and ternary Ag/AgCl/BiOCl measures a significantly lower band-gap that makes it suitable for visible light activation.

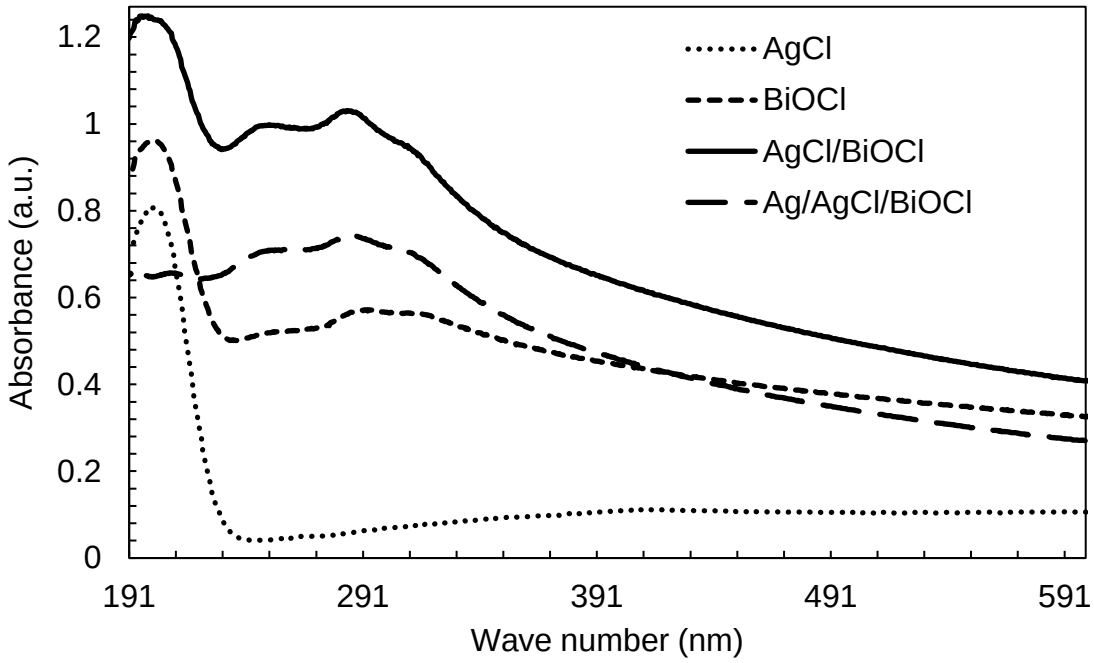

Figure 4.22: UV-vis spectra of synthesised particles

Previous researchers have measured the bandgaps of AgCl and BiOCl. Chen et al. (2017) measured a BiOCl band energy of 3.29 eV and 2.9 eV for their hollowed structured 30% Ag/AgCl/BiOCl microsphere. Ao et al. (2014) measures the absorption edge of BiOCl nanoplates and Ag@AgCl on BiOCl nanoplates to be at 365 nm. Although, this work measures a relatively higher bandgap for AgCl and BiOCl, it also shows a significant reduction in bandgap when both materials are coupled.

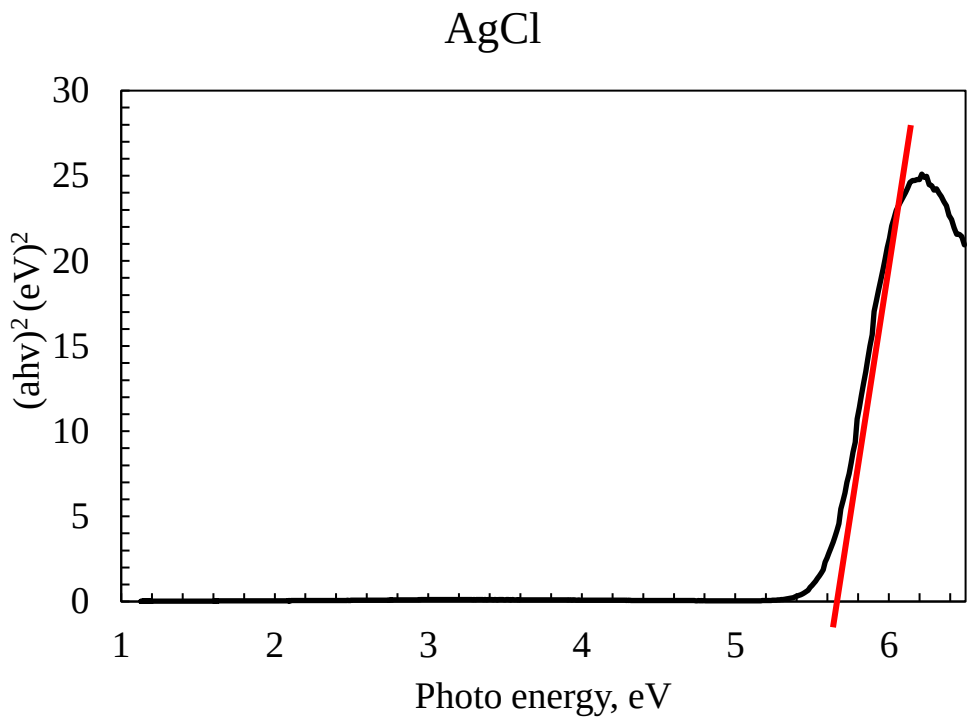

Figure 4.23: Tauc plot and estimated bandgap for AgCl

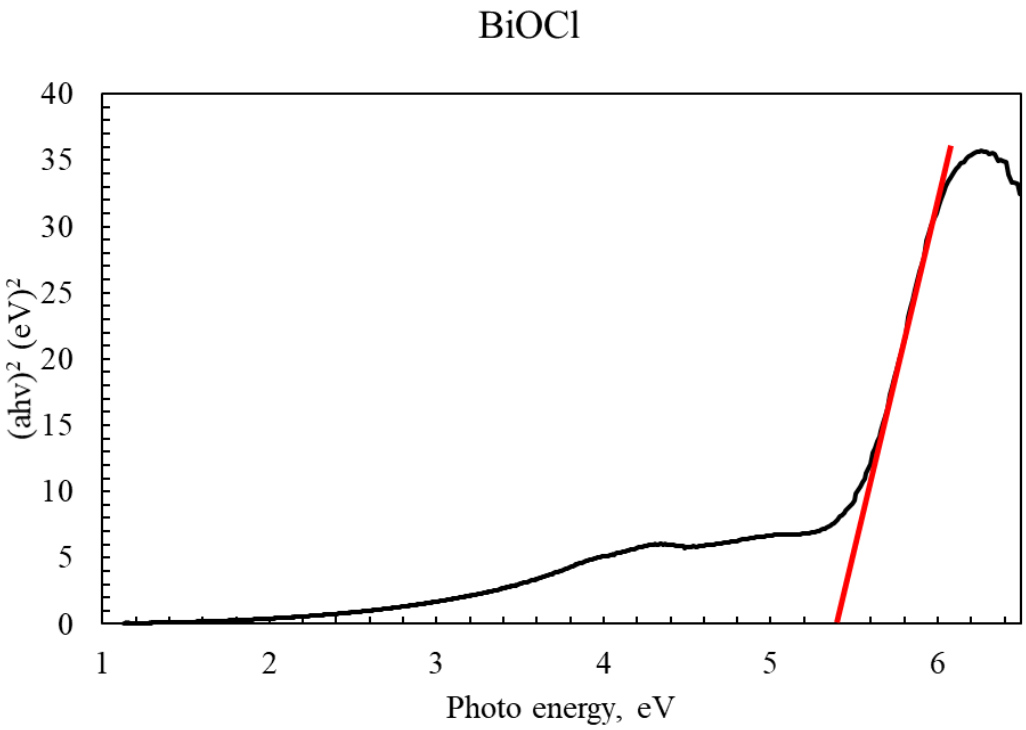

Figure 4.24: Tauc plot and estimated bandgap for BiOCl

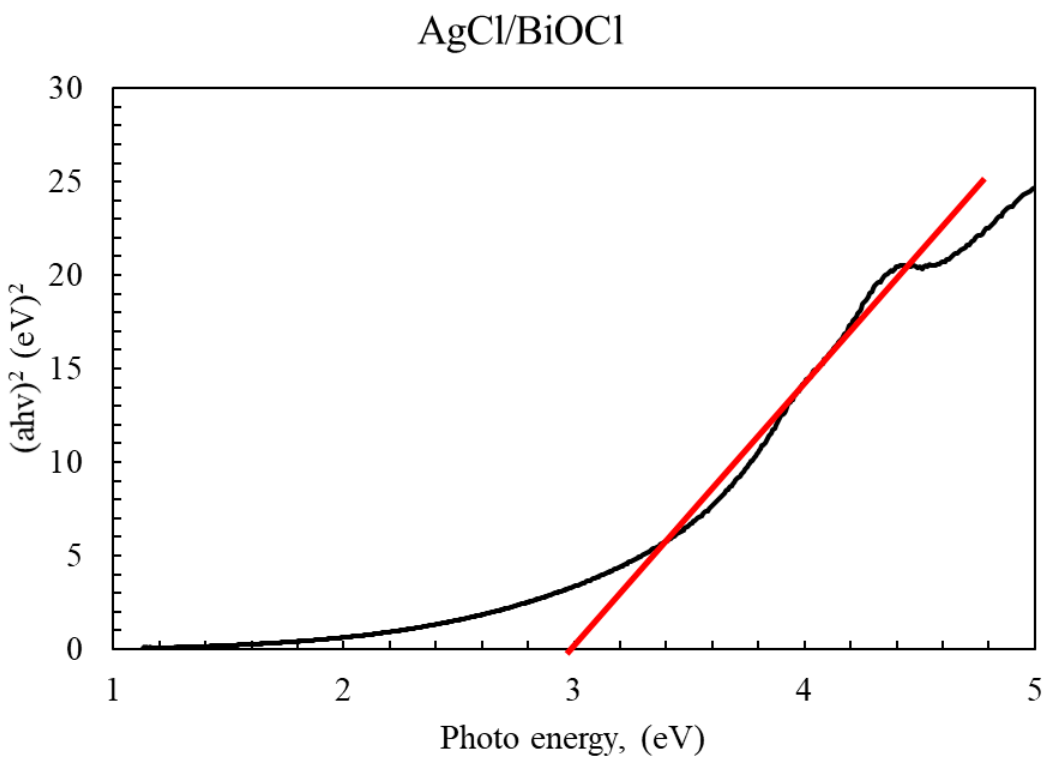

Figure 4.25: Tauc plot and estimated bandgap for AgCl/BiOCl

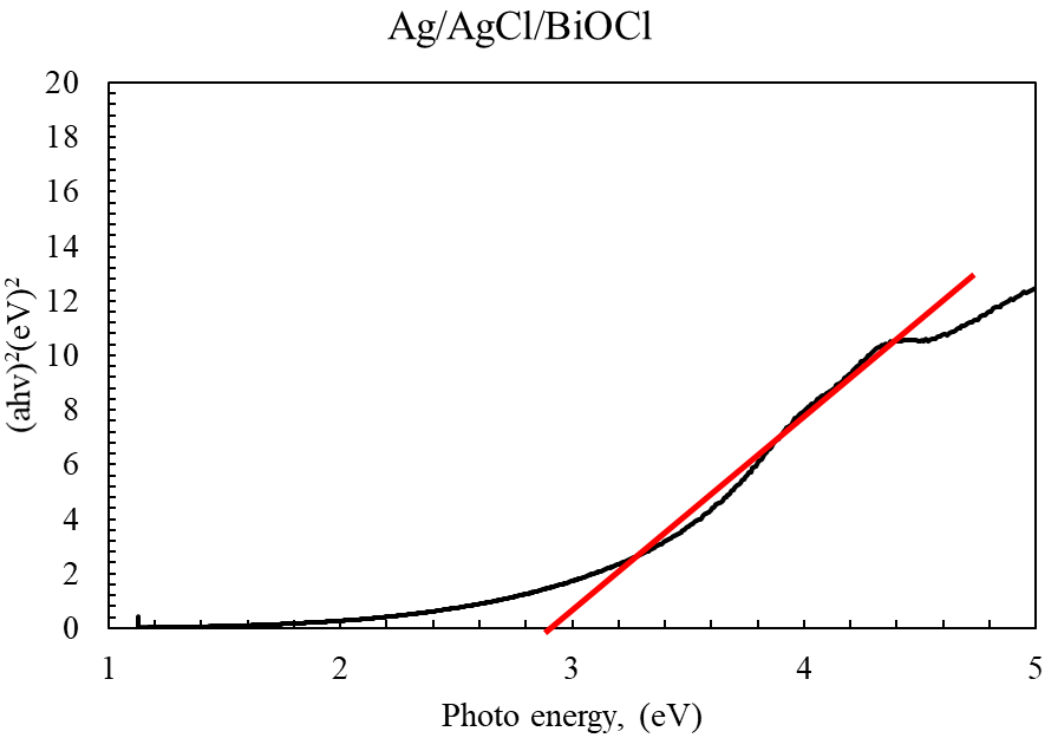

Figure 4.26: Tauc plot and estimated bandgap for Ag/AgCl/BiOCl

CHAPTER 5

DEGRADATION STUDIES

The photocatalytic activity of the synthesised photocatalysts were evaluated in the degradation of phenol. The series of degradation studies was carried out under ultraviolet and visible light irradiation. The experimental setup was carried out as described in Figure 3.2. The degradation efficiency was measured using Equation 14:

$$\text{Degradation \%} = (C_0 - C_t)/C_0 \times 100\ \% \quad (14)$$

where C is the concentration of the phenol solution at time t and C_0 is the initial phenol concentration.

5.1. UV degradation

5.1.1. Effect of initial catalyst loading

The first experiment carried out involved the degradation of phenol under ultraviolet light using the synthesised ternary catalyst to determine the optimum catalyst loading. Initial concentration (10 ppm) and volume (300 mL) of phenol was kept constant throughout the experiment while the mass of Ag/AgCl/BiOCl evaluated were 0 g, 0.1 g, 0.2 g, 0.25 g, 0.3 g, 0.45 g and 1 g and these is shown in Figure 5.1. The 0 g/300 mL experiment which involved UV light only after 30 min stirring in the dark and without the addition of any catalyst particles had a degradation efficiency of 30%. This is a photolysis reaction of phenol under ultraviolet light irradiation where bond cleavage occurs.

The catalyst concentration variation from 0.1 g/300 mL to 1 g/300 ml shows an increase in degradation efficiency as the mass of Ag/AgCl/BiOCl added to the solution increased until a certain point, beyond which the degradation efficiency decreases. This is because as a result of the aggregation of particles with increasing catalyst mass, there is increased turbidity and opacity of the solution which results in the

decreased light intensity striking the solution. This decreased light intensity causes light scattering which consequently reduces the formation of electrons and holes (Gnanaprakasam et al., 2015). The blocking of light from reaching the surface of the catalyst results in the inactivation of the particles.

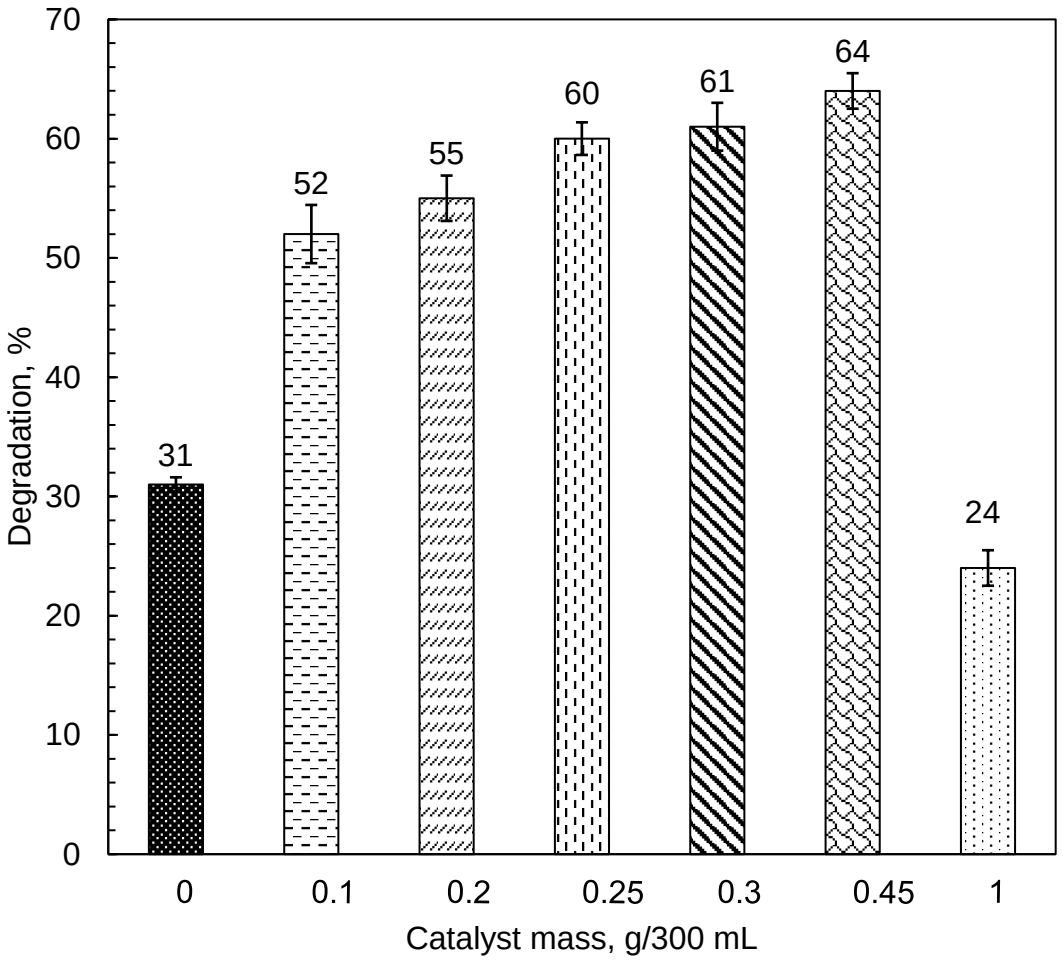

Figure 5.1*:* Phenol degradation under ultraviolet light at different Ag/AgCl/BiOCl loading

The optimum catalyst loading selected for the rest of the experimental procedure is 0.25 g which had a degradation efficiency of 60%. This is because the efficiencies at 0.3 g and 0.45 g were 61% and 64% and does not suggest an optimum loading in relation to the amount of catalyst used. This experiment shows that catalyst loading is an important factor in any photocatalytic process as it has a strong effect on the degradation efficiency as it affects the number of active sites. Therefore, the rate of

reaction will increase until an optimum point where the rate becomes independent of the concentration of catalyst (Wahab and Hussain, 2016).

5.1.2. Effect of photolysis and adsorption

Figure 5.2 shows the degradation of phenol under UV light using Ag/AgCl/BiOCl and titanium dioxide (TiO_2). Two control experiments, light only (photolysis) and catalyst only (adsorption) were also carried out to determine the effect of catalyst and light independently in the photocatalytic experiment under UV light. The catalyst concentration used is 0.25 g/300 mL as determined in the optimum catalyst loading experiment.

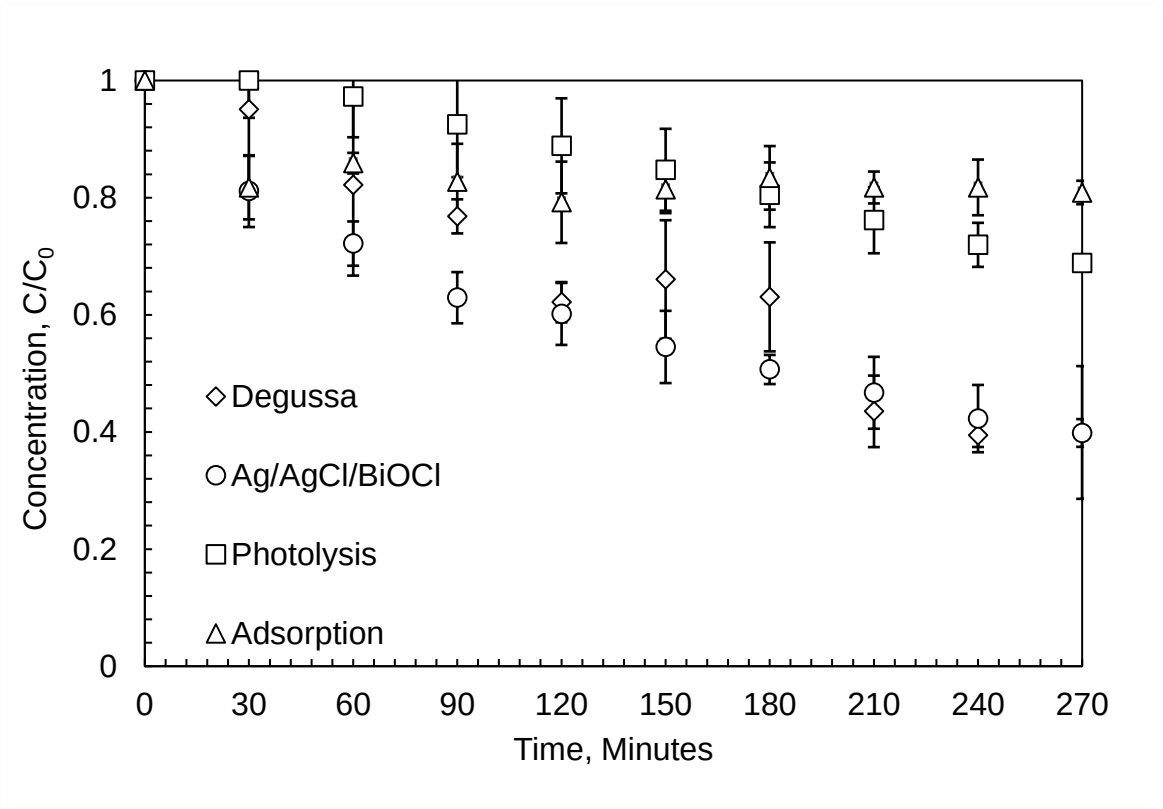

Figure 5.2: Phenol degradation under ultraviolet light using Ag/AgCl/BiOCl and TiO_2 (Degussa)

The result shows a 20% reduction in phenol concentration under the effect of Ag/AgCl/BiOCl only and without light. This was attributed to adsorption of phenol on the surface of the catalyst. The photolysis experiment maintains the photolytic

cleavage of phenol noticed under UV irradiation. Degussa and Ag/AgCl/BiOCl had a similar photocatalytic activity of 60% in the degradation of phenol. This shows that the synthesised Ag/AgCl/BiOCl can be activated in ultraviolet light and capable of degrading phenol. The experiment also confirms that, for substantial degradation of phenol under UV light irradiation, light and photocatalyst are required.

5.1.3. Effect of individual catalyst constituent

The effect and responsiveness of the constituents – AgCl, BiOCl, AgCl/BiOCl – in the ternary catalyst was investigated in the degradation of phenol under UV irradiation. The mass of each catalyst were kept constant at 0.25 g in 300 mL, 10 ppm phenol solution. The results in Figure 5.3 shows AgCl to have the maximum removal of phenol of 75%, BiOCl and AgCl/BiOCl showed a removal efficiency of 47% in comparison to the ternary catalyst, Ag/AgCl/BiOCl with a removal efficiency of 60% under the same conditions. These show that all synthesised catalysts are activated under UV light in the degradation of phenol.

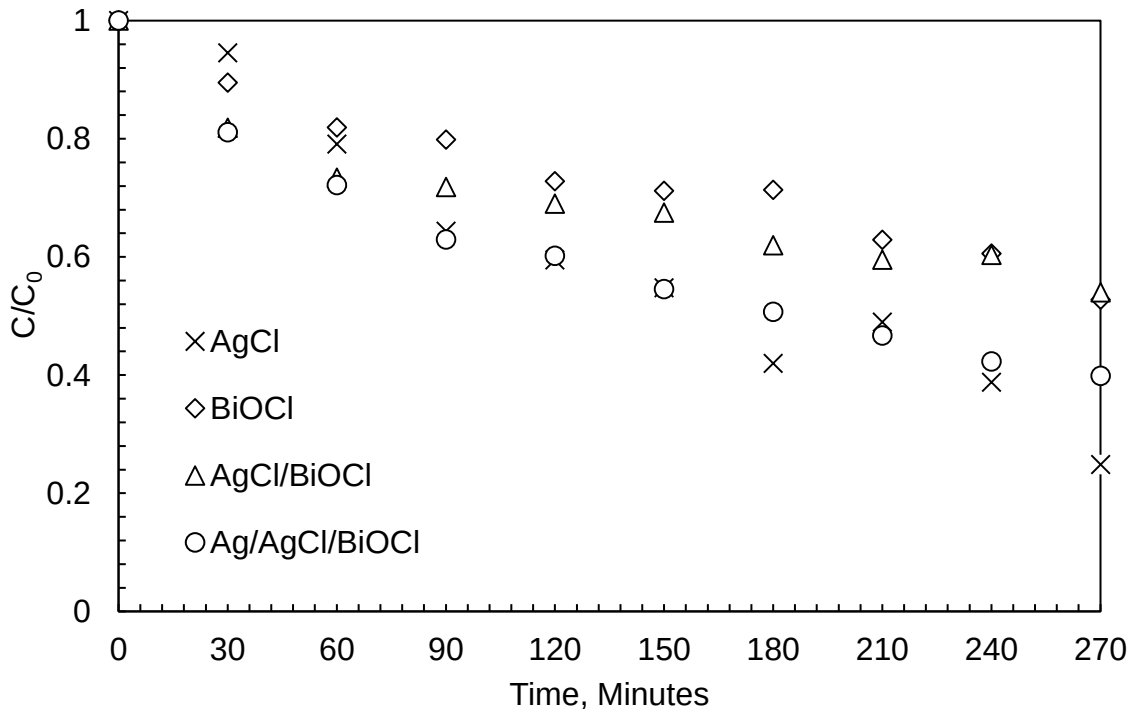

Figure 5.3: Effect of composite catalyst constituents on phenol degradation under UV irradiation

AgCl showed a higher degradation activity in comparison to the other as-synthesised catalysts due to its SPR effects. AgCl is known to be a photosensitive semiconductor therefore has a natural light response in the UV light region (Daupor and Wongnawa, 2014). It was also noticed that coupling metallic Ag on the AgCl/BiOCl improved its photocatalytic degradation efficiency under UV irradiation in comparison to just AgCl/BiOCl and BiOCl photocatalyst.

5.2. Visible light degradation

Although, all as-synthesised catalysts showed responsiveness in the degradation of phenol under ultraviolet irradiation, the primary task of this work is to make full use of sunlight as it contains approximately 5% UV light and 43% visible light (Xie et al., 2017). The next set of experiments then involves investigation into the photocatalytic activity of the as-synthesised catalysts in the degradation of phenol under visible light irradiation.

5.2.1. Effect of photolysis and adsorption

Figure 5.4 shows the results for the photocatalytic test investigating the effects of visible light and synthesised Ag/AgCl/BiOCl in comparison to TiO_2 in the degradation of phenol. The photolysis experiment which is a control experiment, is a visible light only experiment shows a zero degradation of phenol in four hours of irradiation. The photolytic degradation of phenol as a result of bond cleavage noticed under UV light irradiation is absent under visible light irradiation. The 20% degradation due to the adsorption of phenol on the surface of the catalysts is still noticed in the catalysis experiment while a 14% phenol reduction is measured in TiO_2 under photocatalytic conditions. The reduction due to titanium dioxide can be attributed to adsorption of phenol on its surface as it is not activated by visible light. The degradation of phenol under visible light using the as-synthesised ternary catalyst – Ag/AgCl/BiOCl – showed a removal efficiency of 52%. This shows that Ag/AgCl/BiOCl can be activated by visible light irradiation in the degradation of phenol. The photocatalytic experiments also proof that for photocatalysis to occur in the degradation of phenol under visible light irradiation, visible light and a visible light activated photocatalysts is required.

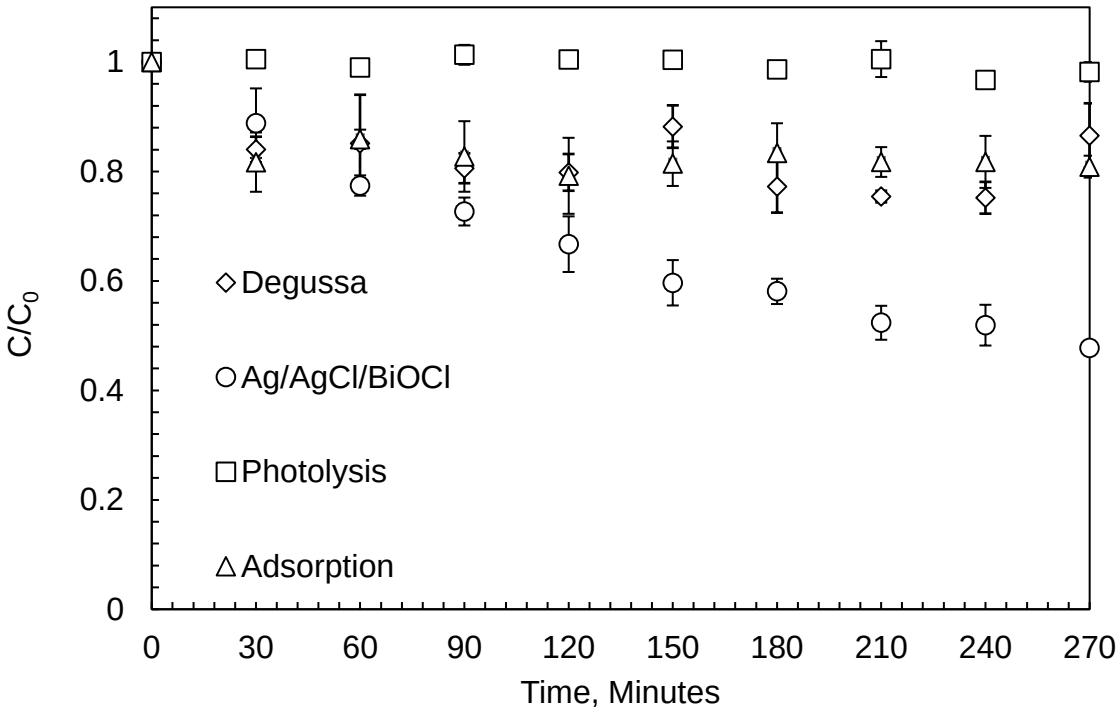

Figure 5.4: Phenol degradation under visible light using Ag/AgCl/BiOCl and TiO_2

5.2.2. Effect of individual catalyst constituent

The photocatalytic degradation experiments of phenol over AgCl, BiOCl, Ag/AgCl/BiOCl were also performed under identical conditions in visible light irradiation and the results are expressed in Figure 5.5. 14% and 15% reduction in phenol concentration was measured when using the synthesised AgCl and BiOCl catalysts. This shows that the synthesised AgCl and BiOCl as individual photocatalysts in the photodegradtion of phenol under visible light irradiation is not effective. While it is known that AgCl is naturally activated only under UV irradiation, the BiOCl result corresponds with the work done by Wang et al. (2014) where they investigated the degradation of 4-nitrophenol under both visible and UV irradiation. They found that in 120 min, 47.61% degradation was noticed using BiOCl in UV light and only 5% is observed under visible light irradiation. For excitation of electrons to occur, the energy of the illuminating light should be greater than the band gap energy of the particles. This experiment shows that while the UV light irradiation enabled photocatalysis on

the surface of AgCl and BiOCl, they were unable to be activated under the visible light irradiation.

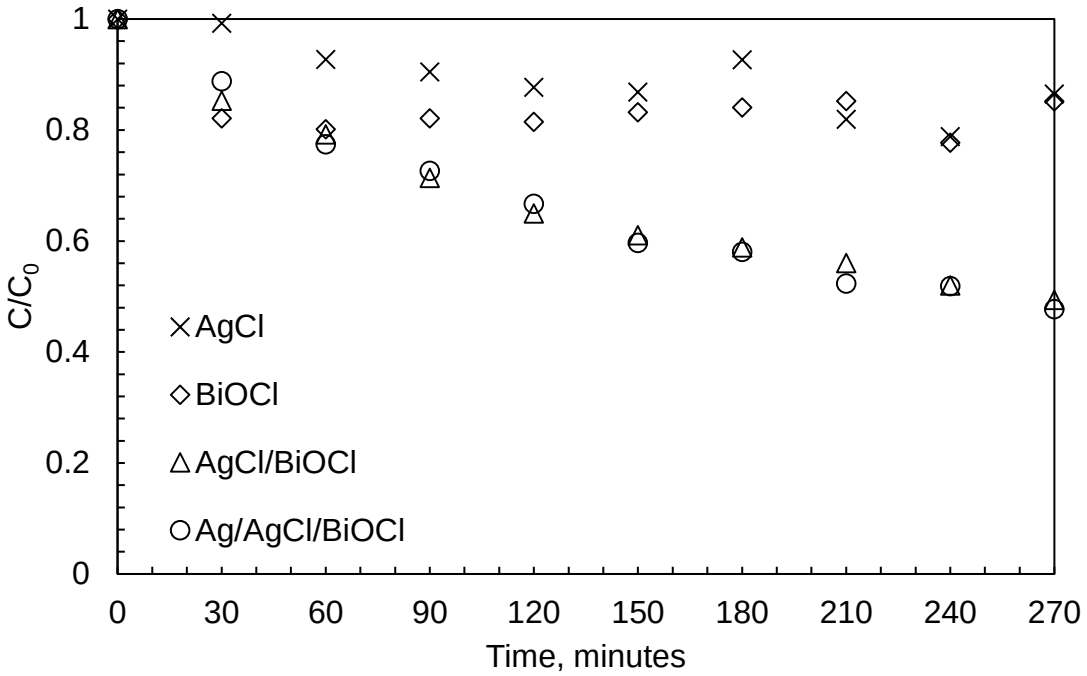

Figure 5.5: Effect of composite catalyst constituents on phenol degradation under visible light irradiation

Zhang et al. (2008) synthesised various BiOX (X =Cl, Br, I) particles and investigated their activity in the degradation of MO under both UV-vis and visible light irradiation. They measured the degradation under UV-vis irradiation using BiOCl to be 17% while 15% was measured under visible light irradiation in 3 h. AgCl/BiOCl and Ag/AgCl/BiOCl showed a similar degradation efficiency of 51% and 52% in the degradation of phenol under visible light irradiation. During the synthesis process, Ag^0 was photoreduced on the surface of AgCl/BiOCl using visible light irradiation for an hour. Therefore, Ag^0 was unavoidably generated during the phenol photocatalytic degradation reaction using AgCl/BiOCl as there was light irradiation. This means that both the binary and ternary catalyst had similar component and hence mechanism in the photodegradation of phenol.

5.2.3. Effect of initial phenol concentration

Experimental procedure to determine the effect of initial phenol concentration on photocatalytic degradation under visible light irradiation was investigated. 0.25 g of Ag/AgCl/BiOCl in 300 mL of phenol with initial phenol concentrations varied between 10 and 100 ppm were done in batch experiments carried out for 30 min adsorption in the dark followed by light irradiation for 4 h. The results are illustrated in Figure 5.6. Result shows maximum phenol degradation removal efficiency at 10 ppm phenol concentration of 52%. This value drastically reduces to 24% as the initial phenol concentration is increased to 20 ppm while a degradation efficiency of 26%, 26%, 20% and 25% is measured in 30 ppm, 50 ppm, 80 ppm and 100 ppm initial pollutant concentration. The degradation efficiencies show that Ag/AgCl/BiOCl is more effective at lower phenol concentrations. As the concentration of phenol increases, more phenolic molecules are present in the solution while the catalyst concentration remains constant. This causes less amount of phenol to be degraded.

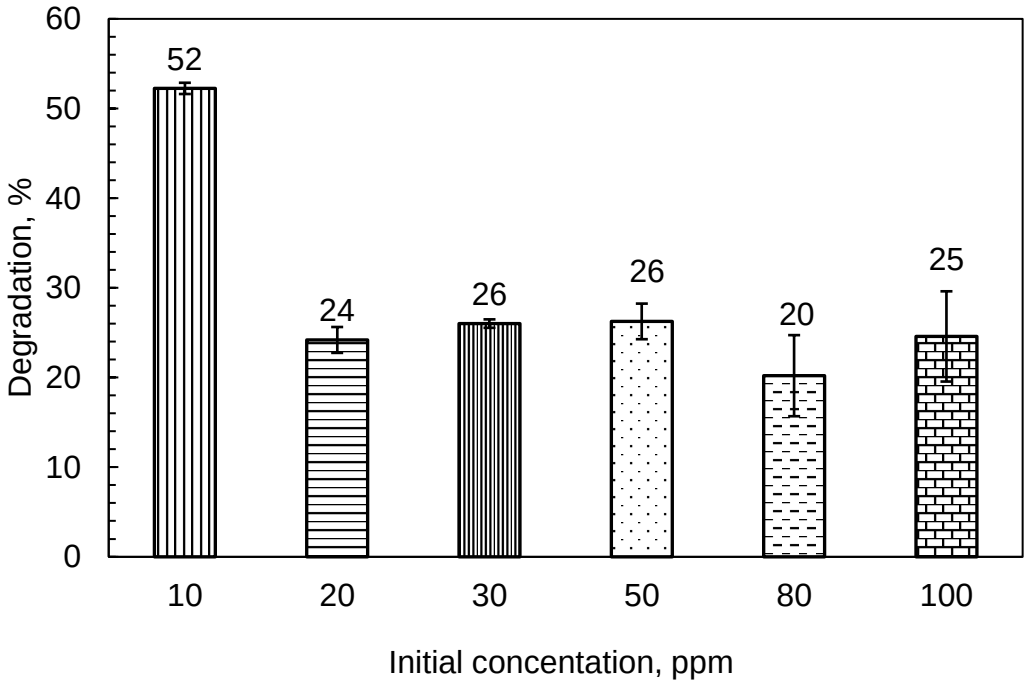

Figure 5.6: Effect of initial phenol concentration on the degradation of phenol under visible light irradiation using Ag/AgCl/BiOCl

Chiu et al. (2019) explains the phenomenon noticed as the adsorption on the surface of photocatalyst affecting its ability of photon absorption thereby affecting the generation of reactive radicals which subsequently pose a significant effect on the rate of the photodegradation. After the critical level has been reached which is 10 ppm in the case of this experiment, the reaction rate becomes constant because the surface of the catalysts has been fully utilised. Li et al. (2019a) explains that increasing the phenol concentration beyond 10 ppm results in the generation of more intermediates that competes with the organic contaminants for active sites on the surface of the catalysts resulting in lower contacts between the photocatalysts and the pollutants.

5.2.4. Effect of initial pH

Figure 5.7 shows the graph of phenol degradation as a function of time for varying initial solution pH. This was done to investigate the effect of initial solution pH on the degradation of phenol under visible light irradiation using Ag/AgCl/BiOCl. The initial pH of the phenol solution is an important factor that affects the rate of degradation. This is because pH of the contaminant solution governs the surface characteristics of particles, their agglomeration size, charge of organic pollutant, adsorption of organic molecules on the surface of photocatalysts and the concentration of the reactive radicals (Azeez et al., 2018). The pH was varied from 3 to 12. This was done using 0.1 M HCl for adjustment in the acidic region and 0.1 M NaOH in the basic region while keeping other factors constant i.e. 0.25 g/300 mL Ag/AgCl/BiOCl, 10 ppm phenol concentration. pH 5.5 is the unadjusted pH of the ultrapure water used throughout this study.

It can be seen from Figure 5.8 that the maximum phenol degradation was found at pH 5.5 at 52%, closely followed by pH 5 at 50% degradation. pH 8 recorded a degradation efficiency of 47%. At an alkaline pH of 12, there is no degradation noticed while acidic pH 3 has a 27% degradation. The degradation of organic molecules is said to be restrained at pH value12 because of competition between hydroxyl ions with organic molecules for adsorption on the catalysts surface (Gnanaprakasam et al., 2015). Also, at alkaline pH, negatively charged phenolate ions are repelled by the surface of the negatively charged particles resulting in the reduced rate of photodegradtion

(Mangrulkar et al., 2012). A decrease in the degradation of phenol at acidic pH is due to less adsorption.

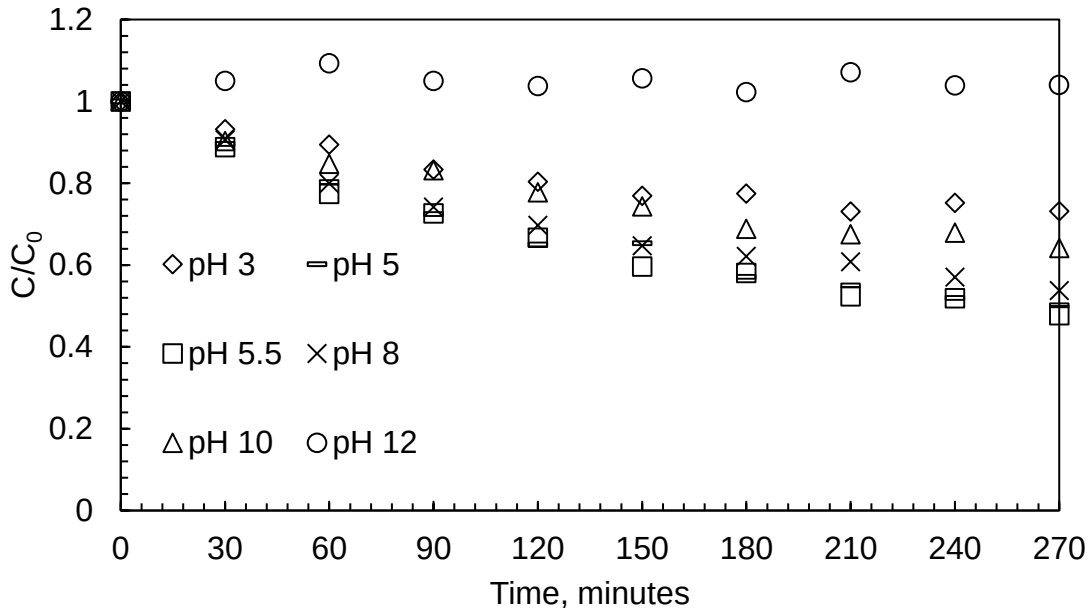

Figure 5.7: Concentration as a function of pH on degradation of phenol under visible light irradiation using Ag/AgCl/BiOCl

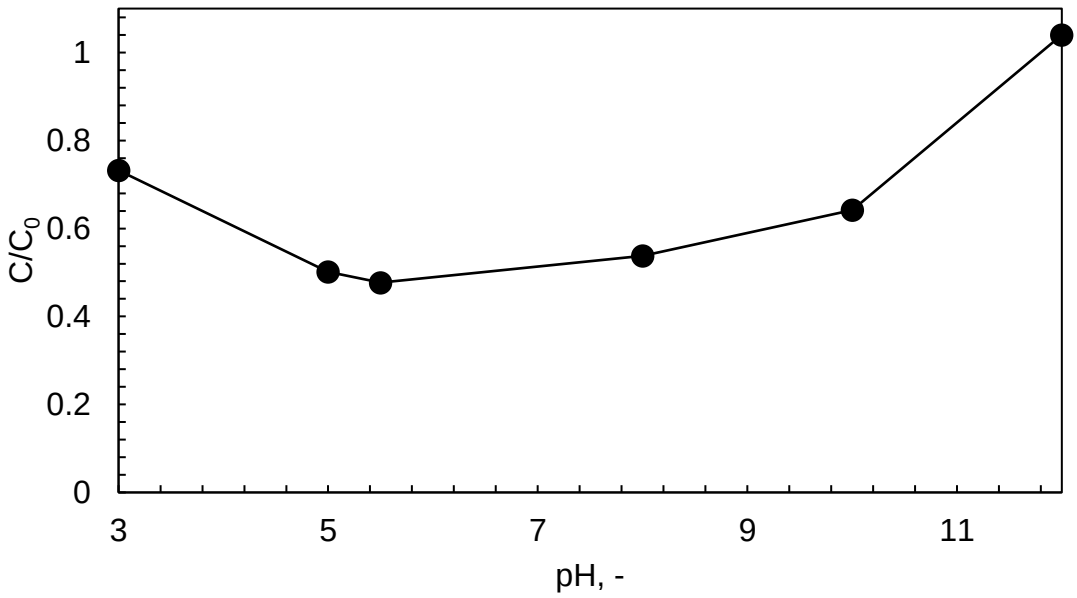

Figure 5.8: Graph of C/C_0 vs pH in the degradation of phenol under visible light irradiation using Ag/AgCl/BiOCl

From Figure 4.20, the point of zero charge of the synthesied Ag/AgCl/BiOCl was measured to be at pH 5. At this pH range, optimum photodegradation of phenol is measured under visible light irradiation. The photodegradation of phenol under visible light was favoured at the neutral state of the photocatalyst. Hu et al., (2010) explains that when the pH of the aqueous solution is close to the point of zero charge of the photocatalyst oxide, the surface hydroxyl groups will be in a neutral state. This means that Ag/AgCl/BiOCl favours the degradation of phenol at a neutral state.

5.3. Catalyst reuse

The chemical stability of the synthesised Ag/AgCl/BiOCl was examined by recycling the catalyst and conducting degradation experiment under the same conditions. After degradation of phenol in the first round, the particles were collected, washed with ethanol, then water before being dried at 80^0C for 8 h. Then the sample is used to degrade a fresh 10 ppm solution of phenol. After 24 h, while the first cycle had a 80% degradation, the second cycle had a phenol removal efficiency of 65% (Figure 5.9). This suggests a relatively very stable photocatalyst as the lost of reactivity is as a result of loss of particles, blocked sites by intermediates or products and leaching of a few catalyst into the solution during photocatalysis (Nguyen et al., 2018).

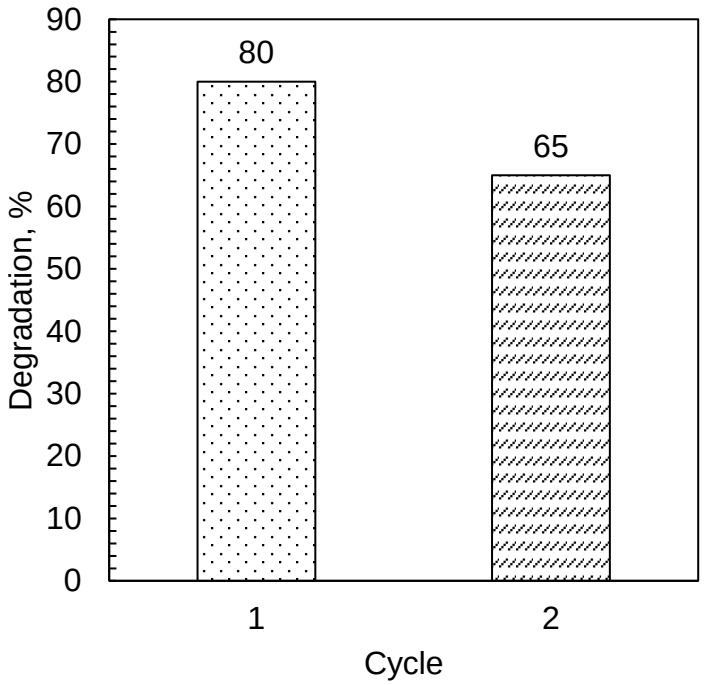

Figure 5.9: Recycle experiment of Ag/AgCl/BiOCl photocatalyst in visible light irradiation

The SEM image of the Ag/AgCl/BiOCl photocatalyst before use and after cycle two resuse in Figure 5.10. It takes the shape of a shrinken-flower-like structure in comparison to the synthesised Ag/AgCl/BiOCl which showed an open flower-like structure. It still contains many rod-like structures assembled together with particle-like AgCl materials.

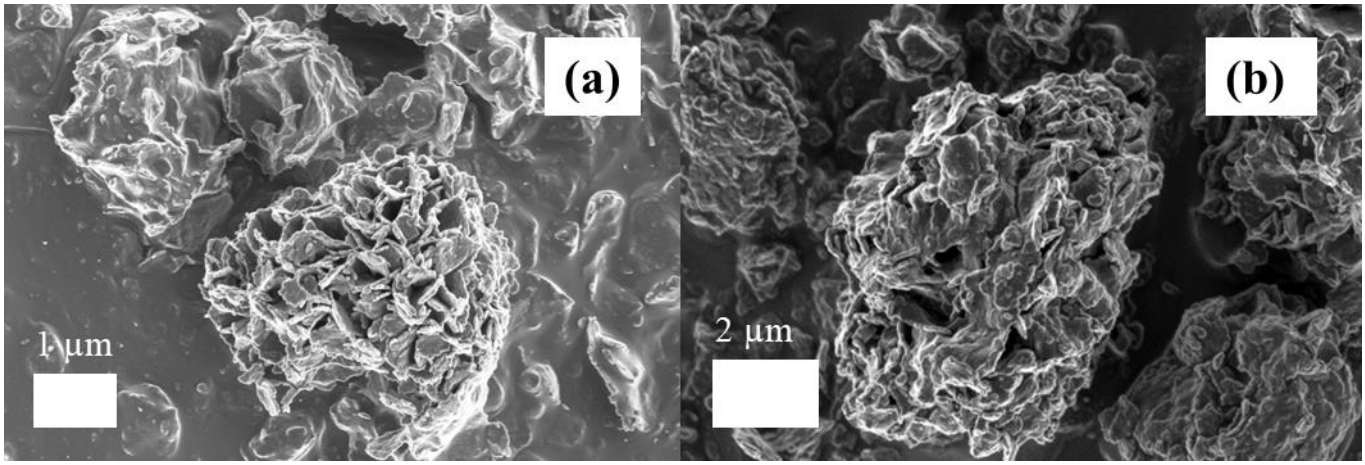

Figure 5.10: SEM images of Ag/AgCl/BiOCl (a) Before use (b) after cycle two

Figure 5.11 shows the elemental mapping of the reuse Ag/AgCl/BiOCl showing peaks for O, Ag, Cl and Bi as the only present elements. Figure 5.12 also illustrates the uniform distribution of these elements across the catalyst surface. These mapping shows that the elements are still present uniformly even after two cycles confirming the stability of the photocatalyst for potential reuse cycles.

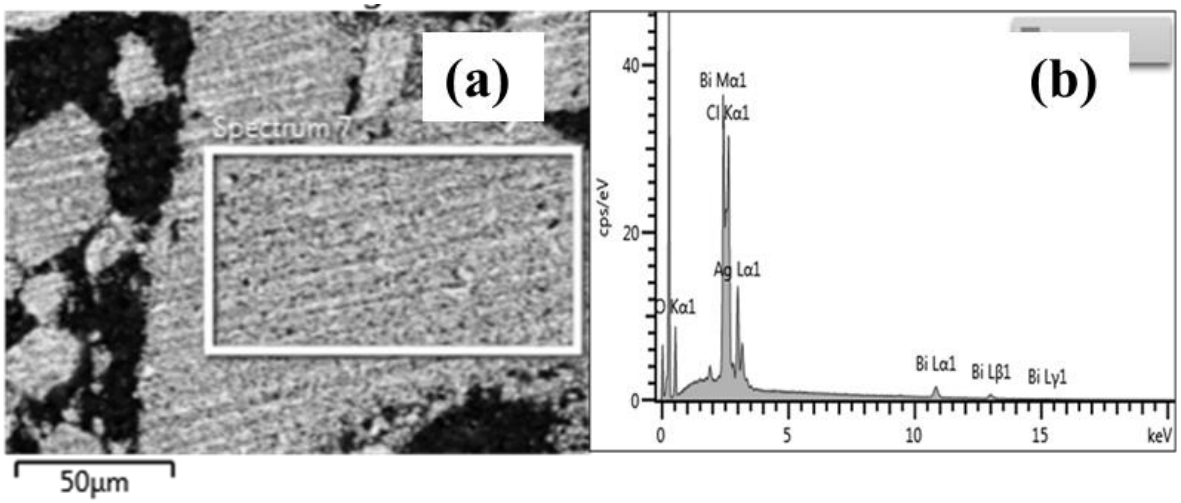

Figure 5.11: EDS mapping of Ag/AgCl/BiOCl cycle one

Table 5.1: Ag/AgCl/BiOCl cycle one atomic and weight composition

Element	Wt%	Wt% Sigma	Atomic %
O	17.25	0.24	56.22
Cl	14.53	0.13	21.38
Ag	22.98	0.22	11.11
Bi	45.24	0.29	11.29

The elemental composition illustrated in Table 5.1 shows the atomic and weight composition of the recycled Ag/AgCl/BiOCl. The elements are still in the correct stoichimetric ratio in Cl:Ag:Bi of 2:1:1 with O still in excess consistent with the other synthesis.

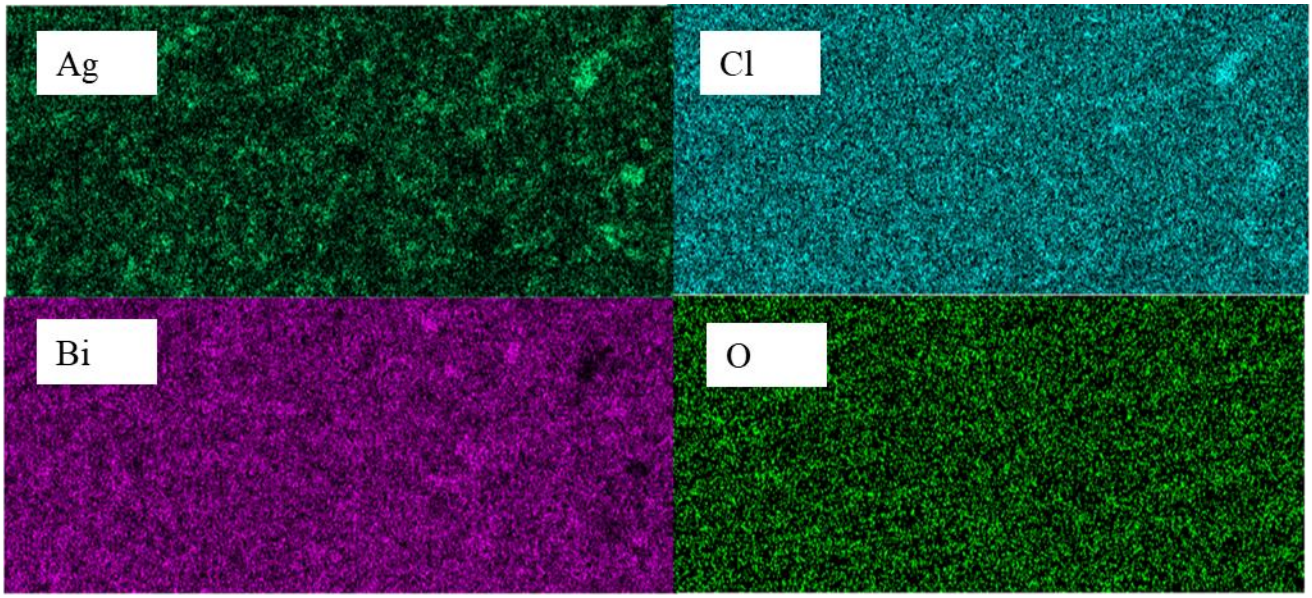

Figure 5.12: Elemental mapping of Ag/AgCl/BiOCl cycle one

5.4. Degradation kinetics

The kinetics for the photodegradation of a single pollutant, phenol, by photocatalysts were fitted to the commonly used modified Langmuir-Hinshelwood model which assumes the following according to Fox and Dulay (1993):

- The system is at equilibrium therefore it has a fixed number of adsorption sites
- One single substrate binds at a surface site
- The adsorption rates by substrates is identical at each site and independent of the surface coverage
- No interactions between adjacent adsorbed molecules
- No blocking of active sites by binding to products

The expression used is the first-order kinetic expression for a specific initial organic content during a photocatalytic process (Li et al., 2008) and this was used to depict the rates of reaction in this study. The equation is shown as Equation 15:

$$r = -\frac{dC}{dt} = K_{app}C \qquad (15)$$

where,

K_{app} is the apparent first-order rate constant where $C = C_0$ at $t = 0$ at initial conditions, r is the rate of reaction and t is the reaction time.

The Langmuir-Hinshelwood model describes the relationship between the apparent rate constant and the initial concentration of organic pollutant and is simplified to the form in Equation 16 to Equation 18.

$$\frac{dC}{dt} = \frac{kK_{phenol}C_0}{1+K_{phenol}C_0} \qquad (16)$$

$$\ln\left(\frac{C_0}{C_t}\right) = kK_{phenol}t \qquad (17)$$

$$\ln\left(\frac{C_0}{C_t}\right) = K_{app}t \qquad (18)$$

K_{phenol} is the absorption coefficient of phenol and K_{app} is the apparent rate constant. The K_{app} values for the phenol photodegradation experiments by Ag/AgCl/BiOCl under ultraviolet light irradiation at the various catalysts loading were determined from Figure 5.13 and shown in Figure 5.14. The curves in Figure 5.14 showed good linearity in the photodegradation experiments fitting pseudo-first-order kinetics.

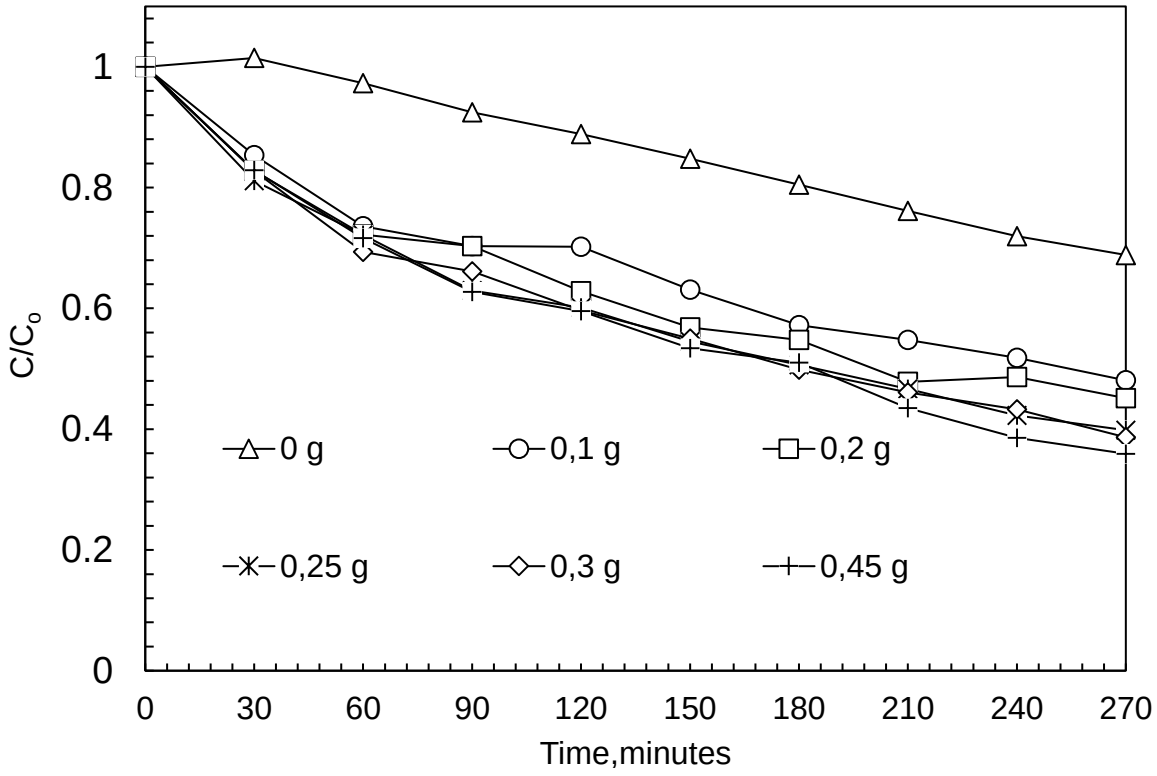

Figure 5.13: Photocatalytic degradation of phenol with varying mass of Ag/AgCl/BiOCl under ultraviolet light irradiation

It can be seen in Figure 5.15 that the K_{app} continues to increase as the mass of catalysts increased until 0.25 g and then beyond this concentration, a decline was noticed as the mass of catalyst increased, the rate of the reaction reduces. K_{App} values at 0.25 g and 0.3 g catalyst mass remains the same proving the assumption to take 0.25 g as the maximum catalyst mass correct. This is as a result of agglomeration and turbidity in the photocatalytic reaction after the optimum catalyst loading resulting in lower active sites and light scattering.

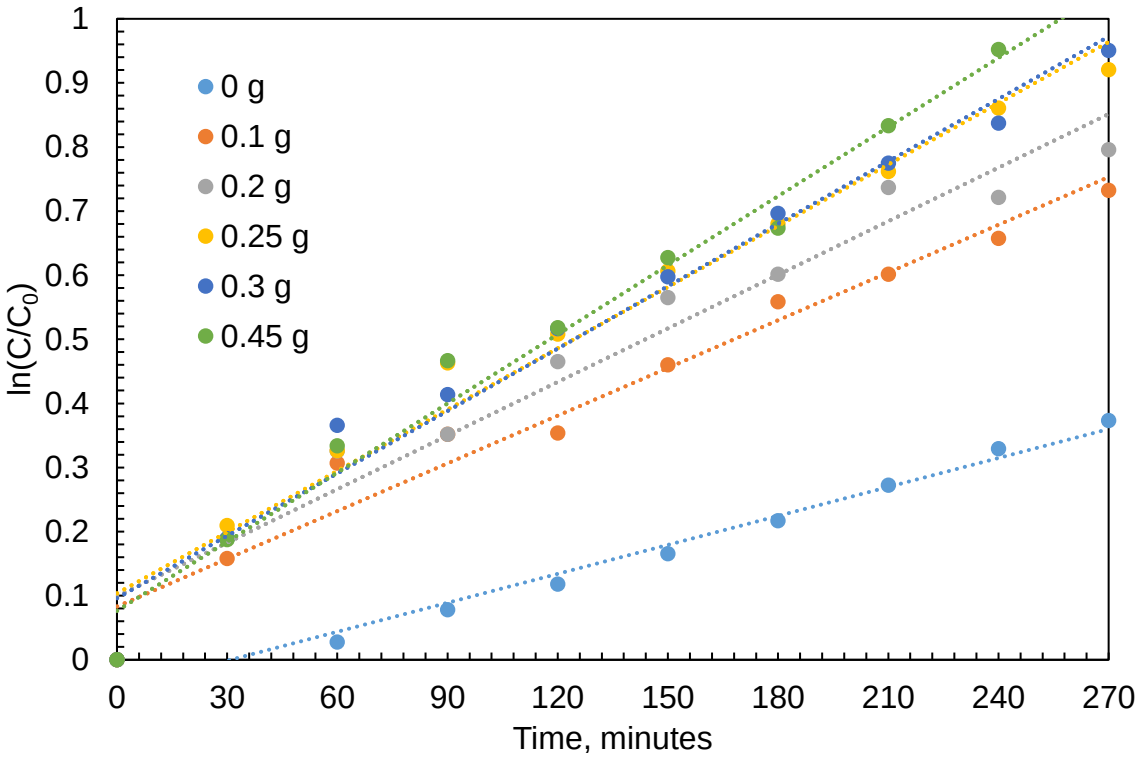

Figure 5.14: Pseudo-first-order reaction kinetics for phenol degradation under ultraviolet light irradiation using varying concentration of Ag/AgCl/BiOCl

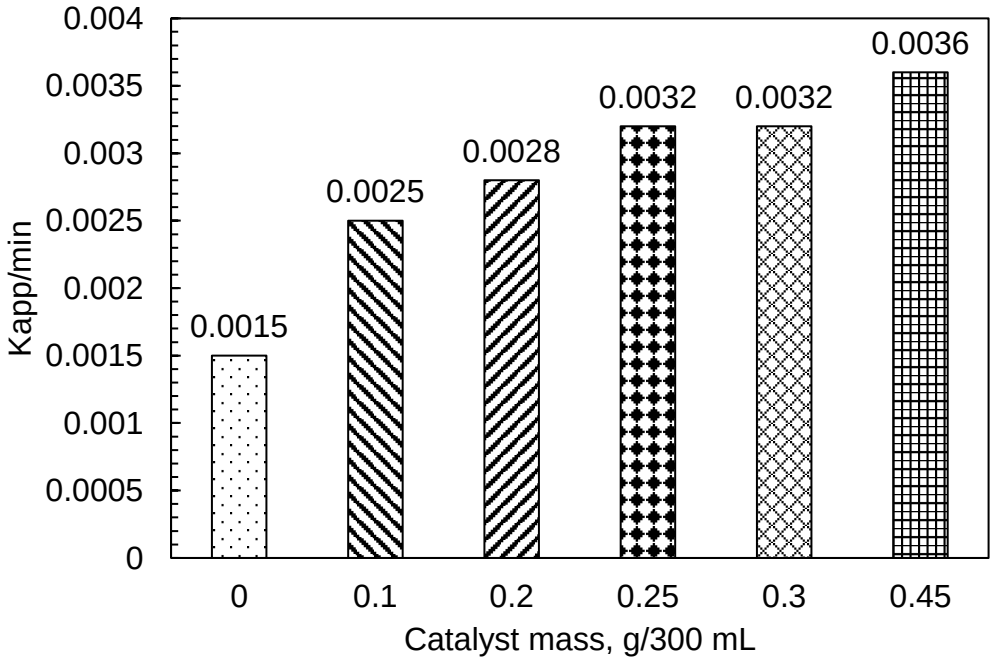

Figure 5.15: Kinetic constants for the photodegration of phenol under ultraviolet light irradiation

Table 5.2: Reaction kinetics parameters for phenol degradation under ultraviolet light irradiation at varying catalysts concentration.

Catalyst mass (g/300 mL)	K_{app}	R^2
0	0.0015	0.979
0.1	0.0025	0.9641
0.2	0.0028	0.9588
0.25	0.0032	0.9737
0.3	0.0032	0.9765
0.45	0.0036	0.9841

Table 5.2 shows that rate constant and regression parameters for the photocatalyst concentration variation. It can be seen that R^2 values are greater than 0.96 coinciding with pseudo-first –order kinetics.

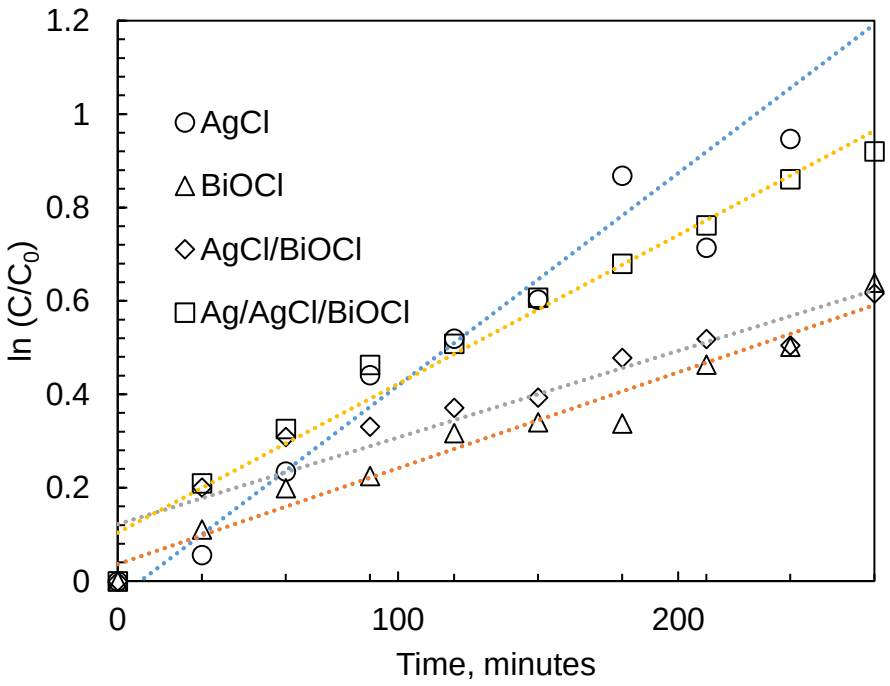

Figure 5.16: Pseudo-first-order reaction kinetics for phenol degradation under UV light irradiation by as-synthesised photocatalysts

Figure 5.16 and Table 5.3 shows the first order kinetics for the degradation of phenol under UV light irradiation by the as-synthesised photocatalysts under the same

conditions. AgCl has the highest rate constant as a result of its SPR abilities which enables excellent degradation of phenol under UV light irradiation.

Table 5.3: Pseudo first-order kinetics parameters for as-synthesised photocatalysts

Photocatalysts	K_{app} (min^{-1})	R^2
AgCl	0.0046	0.9325
BiOCl	0.0021	0.9631
AgCl/BiOCl	0.0019	0.9011
Ag/AgCl/BiOCl	0.0032	0.9737

Figure 5.17 and Table 5.4 demonstrates the kinetic parameters for the visible light degradation of phenol by AgCl/BiOCl and Ag/AgCl/BiOCl and while the ternary photocatalyst shows a higher rate constant of 0.0027 min^{-1}, they both suggest a pseudo-first-order reaction kinetics. AgCl and BiOCl do not fit the pseudo-first order kinetics under visible light due to their ineffectiveness under visible light irradiation.

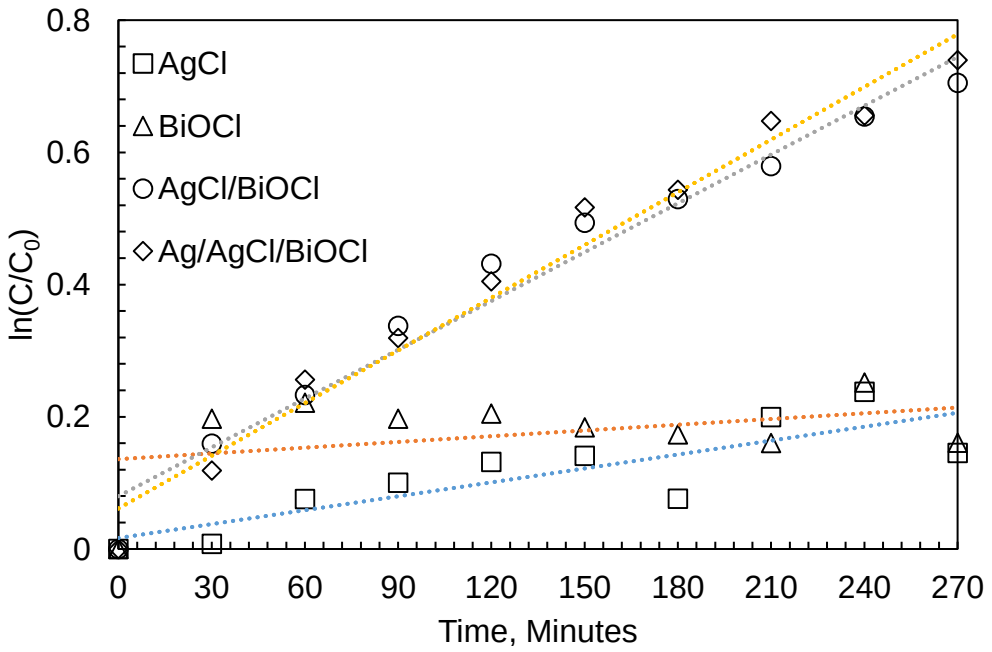

Figure 5.17: Pseudo-first-order reaction kinetics for AgCl/BiOCl and Ag/AgCl/BiOCl under visible light irradiation

Table 5.4: AgCl/BiOCl and Ag/AgCl/BiOCl kinetic equation and correlation coefficient

Photocatalyst	K_{app}	R^2
AgCl	0.0007	0.7039
BiOCl	0.0003	0.1514
AgCl/BiOCl	0.025	0.9678
Ag/AgCl/BiOCl	0.0027	0.9742

5.5. Total organic carbon (TOC) mineralisation analysis

A further investigation was carried out to measure the extent of phenol mineralisation under both visible and ultraviolet light irradiation. This was carried out by measuring the total organic carbon (TOC) after 24 h photodegradation experiments using Ag/AgCl/BiOCl as catalysts and comparing the result to the phenol degradation efficiency measured using the HPLC (Figure *5.18*).

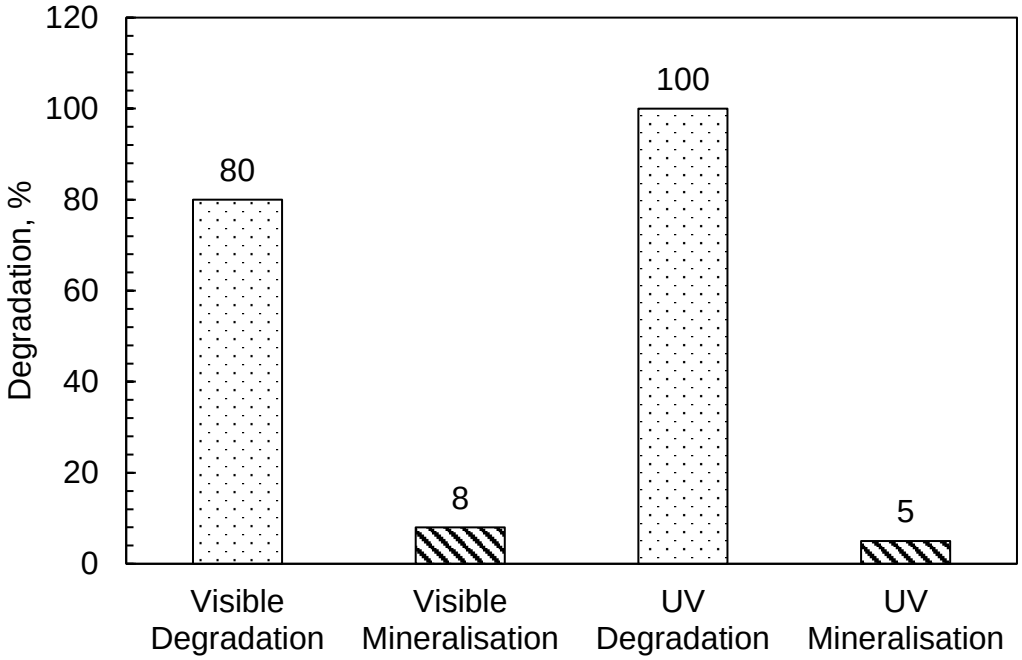

Figure 5.18: Degradation vs mineralisation results under UV and visible light irradiation after 24 h

The results show that while 80% removal in the phenol concentration is measured in 24 h under visible light irradiation while only 8% of the total carbon is mineralised. Under UV irradiation, there was complete removal of phenol in 24 h while 5% mineralisation of the TOC was measured. This phenomenon can be explained by the possible formation of intermediates whereby phenol is broken down into its organic intermediates. The degradation pathways of phenol are known to be complex. Ye et al. (2014) says that for photocatalytic activities involving BiOX/UV-vis systems, the·OH radical is very important for phenol degradation. In the work carried out by Chen et al. (2010), they found that benzoquinone, catechol and hydroquinone were the main intermediate products produced during the degradation of phenol and the structures are shown in Figure 5.19. It is therefore likely that while fairly high degradation of

phenol was observed, the main products were resorcinol, catechol, hydroquinone and benzoquinone with very little mineralisation taking place.

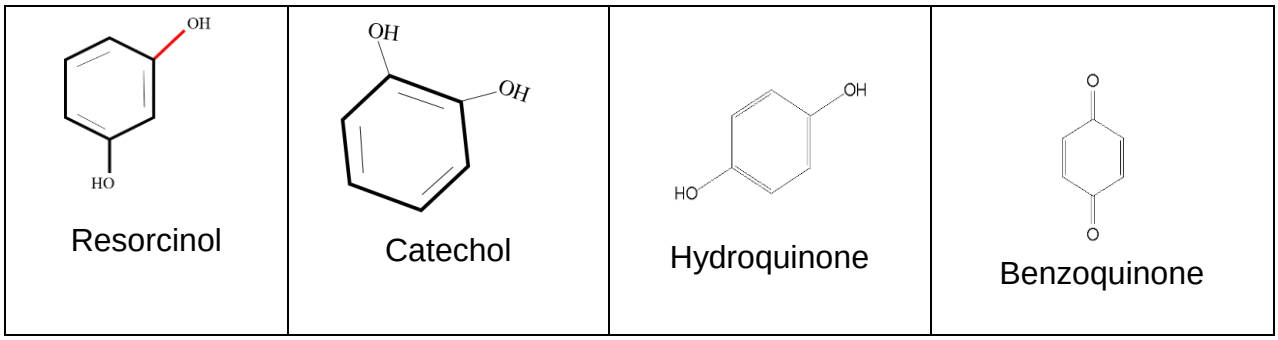

Figure 5.19: Structures of resorcinol, catechol, hydroquinone and benzoquinone

Devi and Rajashekhar (2011) proposed a mechanism for the degradation of phenol under experimental conditions and this is illustrated in Figure 5.20. The OH radical, reacts with the phenol and proceeds to the formation of dihydroxybenzene i.e. resorcinol or catechol and oxalic acid while in a parallel reaction path, benzoquinone and maleic acid are formed (Chowdhury et al., 2017).

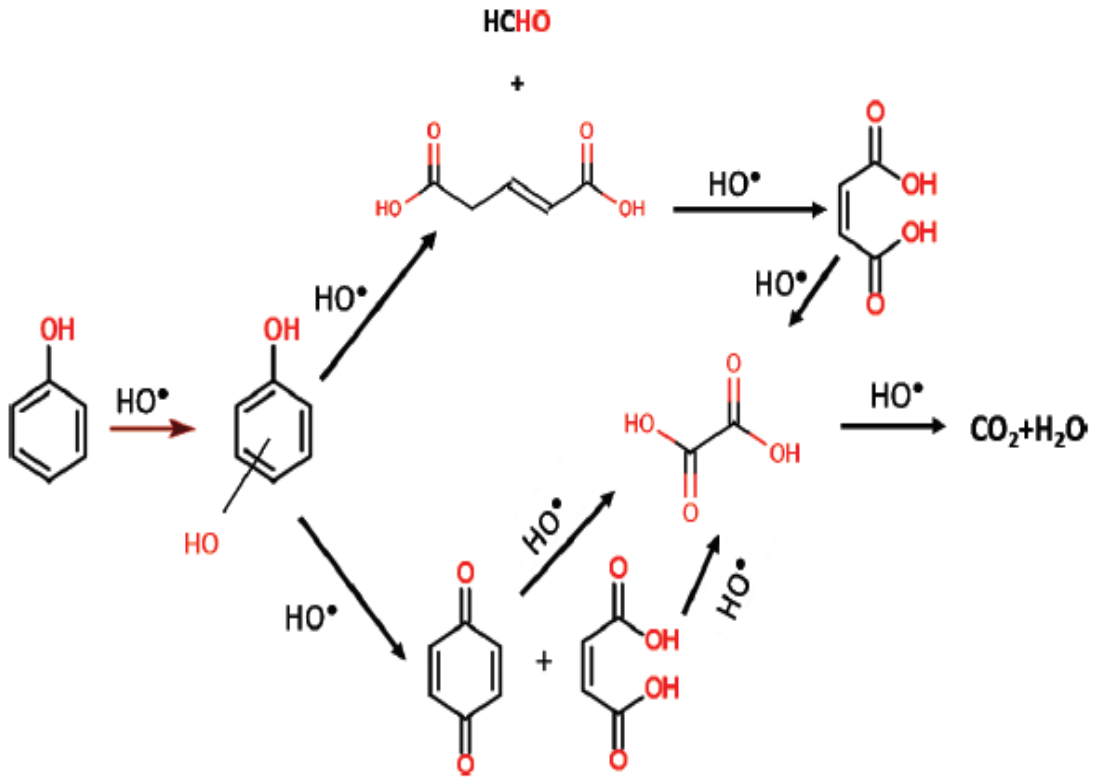

Figure 5.20: Phenol degradation mechanism (Chowdhury et al., 2017; Devi and Rajashekhar, 2011)

5.6. Photocatalytic mechanism

Various catalysts follow different mechanisms that aid the degradation of organic pollutants.

5.6.1. BiOCl

BiOX (Cl, Br, I) has been a widely used photocatalysts since 2008 of which BiOCl has showed higher degradation activity in dyes and phenol under UV irradiation (Ye et al., 2014). Ma et al. (2018) explains that the photocatalytic activity of BiOCl is highly limited due to its high rate of recombination and they proposed that for BiOCl, after excitation of the photocatalyst in simulated sunlight, electrons from the VB jump to the CB as illustrated in Figure 5.21 but are quickly recombined which results in low activity. It is considered that the photogenerated holes can be easily recombined with the surface electrons, resulting in an inhibitory effect of photocatalysis (Xu et al., 2014). Chen et al. (2010) attempts a possible reaction mechanism for BiOCl under UV irradiation. They explain that Cl ion on the surface of BiOCl occupy the photogenerated hole which results in the generation of·Cl radical which causes the weakening of bonds between the chlorine and bismuth ions.

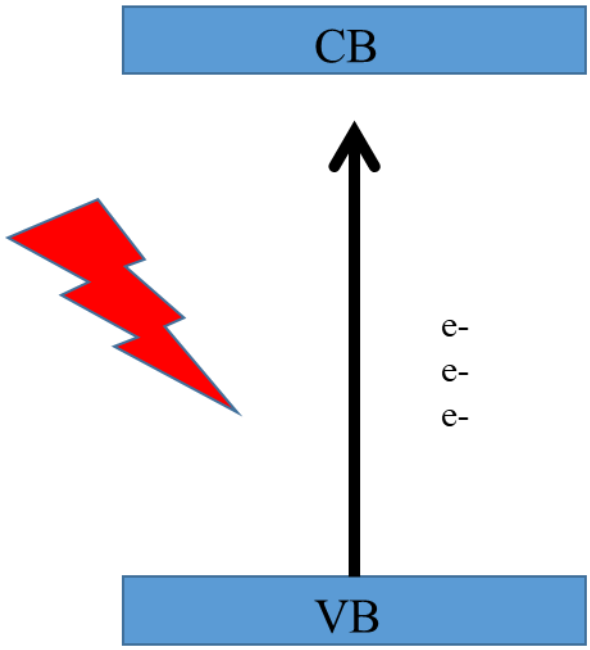

Figure 5.21: Electron excitation in BiOCl (Yang et al., 2018)

5.6.2. AgCl

Photocatalytic experimental procedure carried out in this work showed that while AgCl showed superior activity in the degradation of phenol under UV irradiation, it failed to be activated under visible light irradiation. An explanation for this occurrence could be accredited to the fact that during photodegration under UV irradiation using AgCl, substantial amount of Ag^0 was reduced on the surface of the AgCl forming a Ag/AgCl complex which then took part in the photodegradation of phenol.

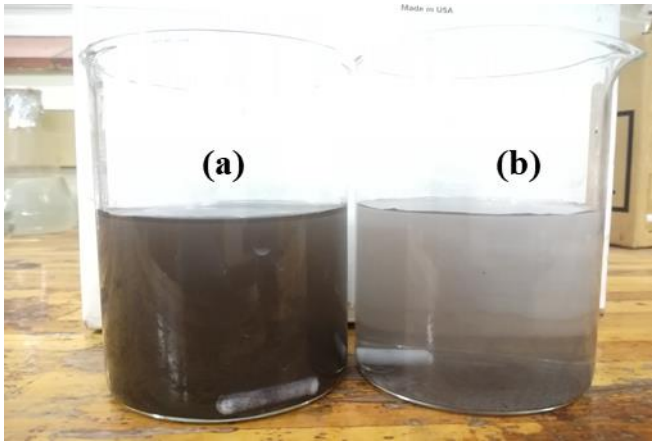

Figure 5.22: (a) AgCl UV light degradation, (b) AgCl visible light degradation

Figure 5.22 illustrates the colour change that was noticed during the photodegration experiments of phenol under UV and visible light irradition while other variables were kept constant. It is noticed that after four hours of light irradiation, a colour present in the UV photo experiment is absent in the visible light experiment. This dark purple colour change is attributed to the presence of metallic Ag in the experiment which aided the photocatalytic activity as a result of its SPR effect. Daupor and Wongnawa (2014) hypothesised a pathway for Ag/AgCl in the degradation of dyes in UV light which is illustrated in Figure 5.23. They propose that while electron-hole pairs are created in the AgCl particle, there could be recombination or seperation and trapping of the electron as Ag^0 or Cl atoms. Oxygen O_2 also traps photogenerated electrons froming O_2^-, which are active species that could degrade the organic molecules. Cl ion are oxidised to Cl atoms by holes in the AgCl while OH- is also oxidised to OH· radical which are all powerful reactive species.

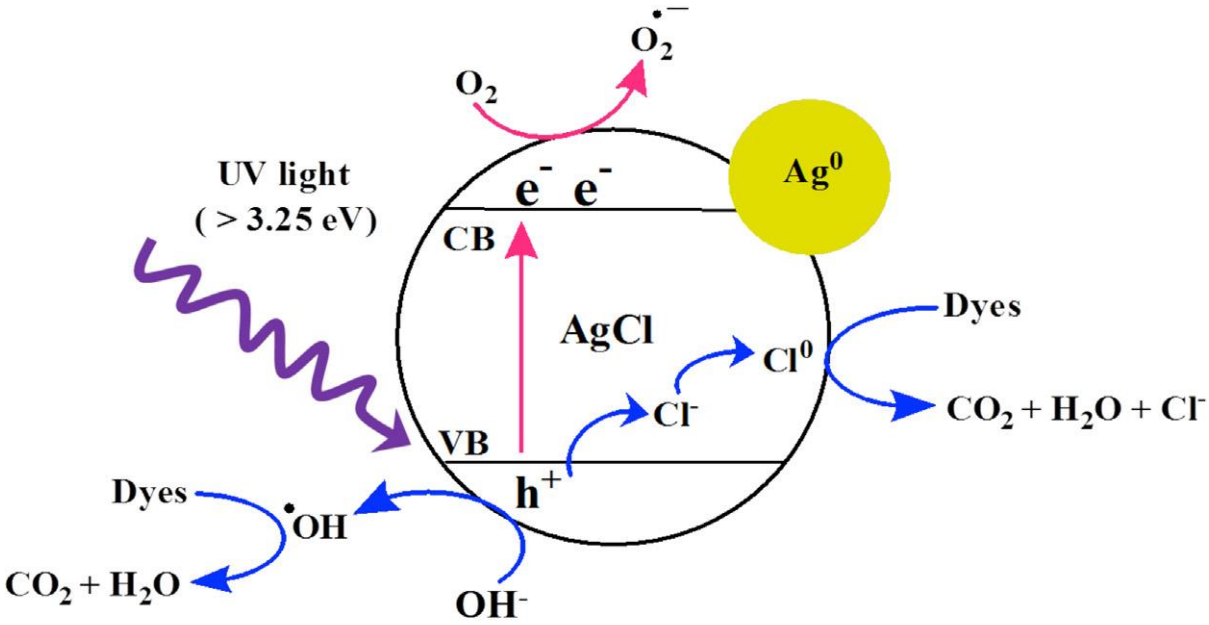

Figure 5.23: Photocatalytic degradation of pollutant under UV light using Ag/AgCl (Daupor and Wongnawa, 2014)

5.6.3. AgCl/BiOCl

Du et al. (2019) explains that under visible light irradiation, both BiOCl and AgCl are photo-excited to holes and electrons. This is done in such a way that the electrons are transferred from the CB of AgCl to the CB of BiOCl and holes are excited from the VB of the BiOCl to that of the AgCl. This ensures that the photogenerated electrons and holes are well separated and therefore recombination is inhibited (Zhou et al., 2014). This system called a heterogenous-type photocatalytic system is aptly illustrated in Figure 5.24 where photocatalyst 1 (PC 1) is AgCl and photocatalyst material 2 (PC 2) is BiOCl.

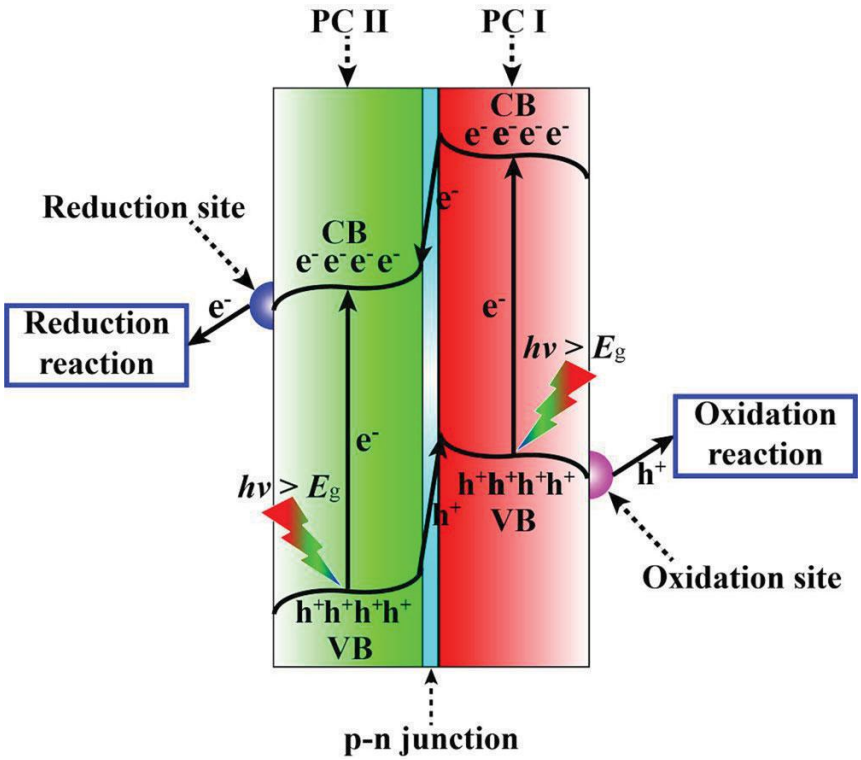

Figure 5.24: Charge transfer in a heterojunction-type photocatalytic system (Zhou et al., 2014)

5.6.4. Ag/AgCl/BiOCl

Based on the experimental procedure carried out in this work, while AgCl/BiOCl and Ag/AgCl/BiOCl both show similar photocatalytic activity under visible light irradiation, Ag/AgCl/BiOCl seems to be a more superior catalyst under UV irradiation. The Ag^0 makes a difference due to its SPR effects which is the photoninduced oscillation of electrons over noble metals (Ye et al., 2014). It was also noticed that AgCl and BiOCl on its own cannot be photo-excited in the photocatalytic degradation of phenol. This means that the Ag nanoparticle assumes the role of electron mediator for trapping of the incident visible light irradiation and generates electron which is transferred to the CB of AgCl (Zhou et al., 2014) and further transferred to the CB of BiOCl as depicted in Figure 5.25.

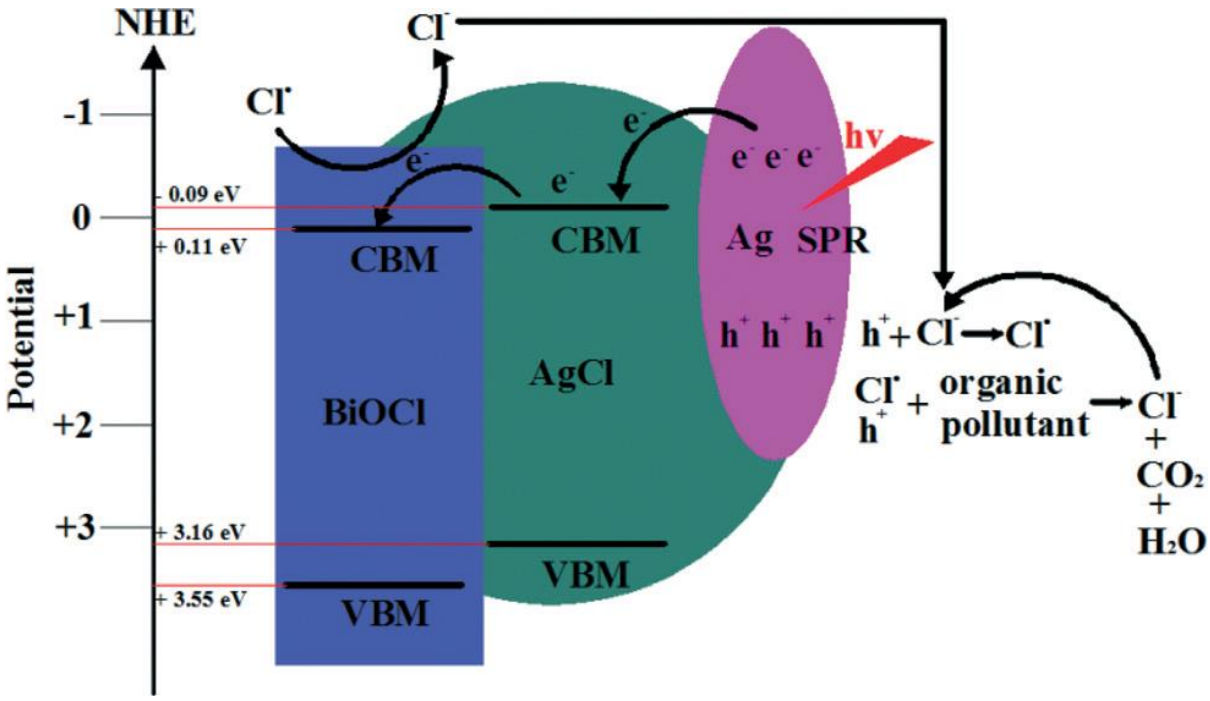

Figure 5.25: Ag/AgCl/BiOCl photocatalytic mechanism (Ye et al., 2014)

CHAPTER 6

CONCLUSIONS AND RECOMMENDATIONS

6.1. Degradation kinetics

This work succeeded in the synthesis of a visible light photocatalyst Ag/AgCl/BiOCl and its constituents AgCl, BiOCl and AgCl/BiOCl. The effectiveness of the synthesis process was validated using various characterisation methods to ascertain the purity, morphology and chemical states of the synthesised catalyst.

The photodegradation potential of the synthesised catalysts were investigated under both ultraviolet and visible light irradiation in the degradation of aromatic carbon, phenol. The batch experiments were designed in such a way that the individual effects of various factors such as light, catalysts, pH and constituents were investigated. The results shows that all the synthesised materials are activated under UV irradiation in the degradation of phenol and due to the stability and durability of the synthesised particles; they can be used in the place of commonly used TiO_2.

Both the binary AgCl/BiOCl and the ternary Ag/AgCl/BiOCl were activated in the photodegradation of phenol under visible light. This confirms the creation of a simple and efficient photocatalyst that utilises visible light (43% of solar spectrum) instead of UV light (4% of solar spectrum). This is attributed to the unique characteristics of the fabricated phototcatalysts such as the morphology, surface area, wide photoabsorption range and low recombination rates.

6.2. Engineering Significance

The heterogeneous photocatalytic field continues to grow as more researchers investigate ways of developing semiconductor materials for photocatalytic purposes. Moving away from commonly used TiO_2 which is only activated in UV light, more semiconductor materials have been engineered to harness solar energy by modifying their structures and coupling materials to reduce the band gap for visible light

activation. The feasibility of using this treatment strategy in large scale scenarios has always been called to question due to the high cost of energy consumption associated with simulated UV light irradiation. The development of semi-conductor materials that can be activated by visible light provides a sustainable alternative to the problem whereby solar energy can be harnessed. Visible light represents 45% of solar energy therefore making the process cheaper and more environmentally friendly. This study fabricated a material through coupling in a Z-scheme fashion to achieve the degradation of phenol under visible light irradiation.

6.3. Recommendations - Future Work

Improvement into the synthesis method should be investigated. This is because, both the binary and the ternary photocatalyst composites had a similar activity in the degradation of phenol. This brings into the question the essence of the irradiation step during the synthesis process as during the photocatalytic process, the synthesised particles will still be exposed to light.

Optimisation studies should be carried out to investigate the ratio of AgCl to BiOCl in the composite material that will be best for optimum degradation. Also, other oxyhalogens such as oxybromide and oxyiodide should be considered and compared to oxychloride for the photodegradation of organic pollutants in visible light.

For further studies, I recommend investigation into the intermediates formed in the degradation of phenol using bismuth and silver-based materials. This will potentially explain the mineralisation result and shed light on the mechanism of phenol degradation under the conditions of this study. Investigations should also be done into the degradation of other organic contaminants as phenol was only studied in this work. While this work proves that the simplest aromatic ring can be degraded, it could contribute into the simultaneous degradation of other contaminants such as pharmaceuticals using the synthesised photocatalyst.

For real-life application, cost analysis studies should be done for a low cost development of large scale and industrial scale production of the photocatalysts. Also,

while this experiment were optimised for laboratory scale under simulated visible light, future investigations should be done “outside” to tap natural solar light using a modified reactor set up.

REFERENCES

ADHIKARI, R., GYAWALI, G., SEKINO, T. & WOHN LEE, S. 2013. Microwave assisted hydrothermal synthesis of Ag/AgCl/WO3 photocatalyst and its photocatalytic activity under simulated solar light. *Journal of Solid State Chemistry,* 197**,** 560-565.

AL ABOODY, M. S. 2019. Silver/silver chloride (Ag/AgCl) nanoparticles synthesized from Azadirachta indica lalex and its antibiofilm activity against fluconazole resistant Candida tropicalis. *Artif Cells Nanomed Biotechnol,* 47**,** 2107-2113.

ALAPI, T. & DOMBI A. 2007. Comparative study of the UV and UV/VUV-induced photolysis of phenol in aqueous solution. *Journal of Photochemistry and Photobiology A: Chemistry*, 188, 409-418.

AO, Y., TANG, H., WANG, P. & WANG, C. 2014. Deposition of Ag@AgCl onto two dimensional square-like BiOCl nanoplates for high visible-light photocatalytic activity. *Materials Letters,* 131**,** 74-77.

AZEEZ, F., AL-HETLANI, E., ARAFA, M., ABDELMONEM, Y., NAZEER, A. A., AMIN, M. O. & MADKOUR, M. 2018. The effect of surface charge on photocatalytic degradation of methylene blue dye using chargeable titania nanoparticles. *Scientific reports,* 8**,** 7104-7104.

BETHI, B., SONAWANE, S. H., BHANVASE, B. A. & GUMFEKAR, S. P. 2016. Nanomaterials-based advanced oxidation processes for wastewater treatment: A review. *Chemical Engineering and Processing: Process Intensification,* 109**,** 178-189.

BHACHU, D. S., MONIZ, S. J. A., SATHASIVAM, S., SCANLON, D. O., WALSH, A., BAWAKED, S. M., MOKHTAR, M., OBAID, A. Y., PARKIN, I. P., TANG, J. & CARMALT, C. J. 2016. Bismuth oxyhalides: synthesis, structure and photoelectrochemical activity. *Chem Sci,* 7**,** 4832-4841.

BRANDI, R., MARTIN, C., & ALFANO, O., et al. (2016). A Laboratory Reactor for Photocatalytic Studies in Slurry Operation. *Journal of Advanced Oxidation Technologies*, 5(2), pp. 175-185.

BYRNE, C., SUBRAMANIAN, G. & PILLAI, S. C. 2018. Recent advances in photocatalysis for environmental applications. *Journal of Environmental Chemical Engineering,* 6**,** 3531-3555.

CAI, B., WANG, J., GAN, S., HAN, D., WU, Z. & NIU, L. 2014. A distinctive red Ag/AgCl photocatalyst with efficient photocatalytic oxidative and reductive activities. *J. Mater. Chem. A,* 2**,** 5280-5286.

CAI, L. 2015. Enhanced visible light photocatalytic activity of BiOCl by compositing with g-C3N4. *Materials Research Innovations*, 19, 392-396.

CHEN, C.-C., YANG, C.-T., CHUNG, W.-H., CHANG, J.-L. & LIN, W.-Y. 2017. Synthesis and characterization of Bi4Si3O12, Bi2SiO5, and Bi12SiO20 by controlled hydrothermal method and their photocatalytic activity. *Journal of the Taiwan Institute of Chemical Engineers,* 78**,** 157-167.

CHEN, D., SIVAKUMAR, M. & RAY, A. K. 2008. Heterogeneous Photocatalysis in Environmental Remediation. *Developments in Chemical Engineering and Mineral Processing,* 8**,** 505-550.

CHEN, F., LIU, H., BAGWASI, S., SHEN, X. & ZHANG, J. 2010. Photocatalytic study of BiOCl for degradation of organic pollutants under UV irradiation. *Journal of Photochemistry and Photobiology A: Chemistry,* 215**,** 76-80.

CHEN, X., HOU, J., YANG, H. & XU, Z.-L. 2016a. Facile preparation of NPs based on Ag–AgCl immobilized in porous PVA sphere with high visible light photoactivity and good photostability under Cl − condition. *Journal of Environmental Chemical Engineering,* 4**,** 1068-1075.

CHEN, Y., ZHU, G., LIU, Y., GAO, J., WANG, C., ZHU, R. & LIU, P. 2016b. Preparation of hollow Ag/AgCl/BiOCl microspheres with enhanced photocatalytic activity for methyl orange under LED light irradiation. *Journal of Materials Science: Materials in Electronics,* 28**,** 2859-2866.

CHENG, H., HUANG, B. & DAI, Y. 2014. Engineering BiOX (X = Cl, Br, I) nanostructures for highly efficient photocatalytic applications. *Nanoscale,* 6**,** 2009-26.

CHIU, Y.-H., CHANG, T.-F. M., CHEN, C.-Y., SONE, M. & HSU, Y.-J. 2019. Mechanistic Insights into Photodegradation of Organic Dyes Using Heterostructure Photocatalysts. *Catalysts,* 9.

CHOWDHURY, P., NAG, S. & RAY, A. K. 2017. Degradation of Phenolic Compounds Through UV and Visible- Light-Driven Photocatalysis: Technical and Economic Aspects. *Phenolic Compounds - Natural Sources, Importance and Applications.*

CUI, D., WANG, L., XU, K., REN, L., WANG, L., YU, Y., DU, Y. & HAO, W. 2018. Band-gap engineering of BiOCl with oxygen vacancies for efficient photooxidation properties under visible-light irradiation. *Journal of Materials Chemistry A,* 6**,** 2193-2199.

CUI, W., LI, X., GAO, C., DONG, F. & CHEN, X. 2017. Ternary Ag/AgCl-(BiO) 2 CO 3 composites as high-performance visible-light plasmonic photocatalysts. *Catalysis Today,* 284**,** 67-76.

CYCHOSZ, K. A. & THOMMES, M. 2018. Progress in the Physisorption Characterization of Nanoporous Gas Storage Materials. *Engineering,* 4**,** 559-566.
DAI, L., LIU, R., HU, L. Q. & SI, C. L. 2017. Simple and green fabrication of AgCl/Ag-cellulose paper with antibacterial and photocatalytic activity. *Carbohydr Polym,* 174**,** 450-455.

DAUPOR, H. & WONGNAWA, S. 2014. Urchinlike Ag/AgCl photocatalyst: Synthesis, characterization, and activity. *Applied Catalysis A: General,* 473**,** 59-69.

DENG, Y. & ZHAO, R. 2015. Advanced Oxidation Processes (AOPs) in Wastewater Treatment. *Current Pollution Reports,* 1**,** 167-176.

DEVI, L. G. & RAJASHEKHAR, K. E. 2011. A kinetic model based on non-linear regression analysis is proposed for the degradation of phenol under UV/solar light using nitrogen doped TiO2. *Journal of Molecular Catalysis A: Chemical,* 334**,** 65-76.

DU, M., ZHANG, S., XING, Z., LI, Z., YIN, J., ZOU, J., ZHU, Q. & ZHOU, W. 2019. All-Solid Z-Scheme Bi-BiOCl/AgCl Heterojunction Microspheres for Improved Electron-Hole Separation and Enhanced Visible Light-Driven Photocatalytic Performance. *Langmuir,* 35**,** 7887-7895.

DUAN, W., MENG, F., CUI, H., LIN, Y., WANG, G. & WU, J. 2018. Ecotoxicity of phenol and cresols to aquatic organisms: a review. *Ecotoxicology and environmental safety,* 157**,** 441-456.

EL HADDAD, M., REGTI, A., LAAMARI, M. R., MAMOUNI, R. & SAFFAJ, N. 2014. Use of Fenton reagent as advanced oxidative process for removing textile dyes from aqueous solutions. *J. MAter. Environ. Sci.,* 5**,** 667-674.

FENG, Z., YU, J., SUN, D. & WANG, T. 2016. Visible-light-driven photocatalysts Ag/AgCl dispersed on mesoporous Al2O3 with enhanced photocatalytic performance. *J Colloid Interface Sci,* 480**,** 184-190.

FOX, M. & DULAY, M. 1993. Heterogenous photocatalysis. *Chemical reviews,* 93**,** 341-357.

GANESHRAJA, A. S., ZHU, K., NOMURA, K. & WANG, J. 2018. Hierarchical assembly of AgCl@Sn-TiO2 microspheres with enhanced visible light photocatalytic performance. *Applied Surface Science,* 441**,** 678-687.

GNANAPRAKASAM, A., SIVAKUMAR, V. M. & THIRUMARIMURUGAN, M. 2015. Influencing Parameters in the Photocatalytic Degradation of Organic Effluent via Nanometal Oxide Catalyst: A Review. *Indian Journal of Materials Science,* 2015**,** 1-16.

GUO, J. F., MA, B., YIN, A., FAN, K. & DAI, W. L. 2012. Highly stable and efficient Ag/AgCl@TiO2 photocatalyst: preparation, characterization, and application in the treatment of aqueous hazardous pollutants. *J Hazard Mater,* 211-212**,** 77-82.

HE, R., XU, D., CHENG, B., YU, J. & HO, W. 2018. Review on nanoscale Bi-based photocatalysts. *Nanoscale Horizons,* 3**,** 464-504.

HOFFMANN, M. R., MARTIN, S. T., CHOI, W. & BAHNEMANN, D. 1995. Environmental Applications of Semiconductor Photocatalysis. *Chemical reviews*, 69-96.

HONG, S., RATPUKDI, T., SIVAGURU, J. & KHAN, E. 2017. Glutaraldehyde Removal from Produced Waters USing Visible Light Driven Photocatalysis *WEFTEC*.

HU, C., PENG, T., HU, X., NIE, Y., ZHOU, X., QU, J. & HE, H. 2010. Plasmon-Induced Photodegradation of Toxic Pollutants with Ag−AgI/Al2O3 under Visible-Light Irradiation. *Journal of the American Chemical Society,* 132**,** 857-862.

HUANG, S., CHEN, J., ZHONG, J., LI, J., HU, W., LI, M., HUANG, K. & DUAN, R. 2017. Enhanced photocatalytic performance of Ag/AgCl/SnO 2 originating from efficient formation of · O 2 −. *Materials Chemistry and Physics,* 201**,** 35-41.

IBHADON, A. & FITZPATRICK, P. 2013. Heterogeneous Photocatalysis: Recent Advances and Applications. *Catalysts,* 3**,** 189-218.

JI, P. L., KONG, X. Z., WANG, J. G. & ZHU, X. L. 2012. Characterization and photocatalytic properties of silver and silver chloride doped TiO2 hollow nanoparticles. *Chinese Chemical Letters,* 23**,** 1399-1402.

KUMAR, A., THAKUR, P. R., SHARMA, G., NAUSHAD, M., RANA, A., MOLA, G. T. & STADLER, F. J. 2018. Carbon nitride, metal nitrides, phosphides, chalcogenides, perovskites and carbides nanophotocatalysts for environmental applications. *Environmental Chemistry Letters*.

KUMAR, S., AHLAWAT, W., BHANJANA, G., HEYDARIFARD, S., NAZHAD, M. M. & DILBAGHI, N. 2014. Nanotechnology-based water treatment strategies. *J Nanosci Nanotechnol,* 14**,** 1838-58.

Khuzwayo Z., Chirwa E.M.N. (2016). Evaluation of flow-rate dynamics in the simultaneous photocatalytic treatment of multichlorinated substituted phenols in continuous-flow systems. *Water Science and Technology*, 74 (9), Pages 2211-2224

LI, B., LAI, C., XU, P., ZENG, G., HUANG, D., QIN, L., YI, H., CHENG, M., WANG, L., HUANG, F., LIU, S. & ZHANG, M. 2019a. Facile synthesis of bismuth oxyhalogen-based Z-scheme photocatalyst for visible-light-driven pollutant removal: Kinetics, degradation pathways and mechanism. *Journal of Cleaner Production,* 225**,** 898-912.

LI, H., LI, C., LI, N., ZHU, L., ZHUO, Y. & XIONG, D. 2019b. One-step synthesis of novel Ag/AgCl-glass with remarkably stable photocatalytic activity. *Journal of Non-Crystalline Solids,* 506**,** 21-27.

LI, J., MA, M. & WANG, Z. 2010. In vitro profiling of endocrine disrupting effects of phenols. *Toxicol In Vitro,* 24**,** 201-7.

LI, Q., DUAN, G., LUO, J. & LIU, X. 2018a. Ultrasonic-assisted synthesis of plasmonic Z-scheme Ag/AgCl/WO3-nanoflakes photocatalyst in geothermal water with enhanced visible-light photocatalytic performance. *Journal of Energy Chemistry,* 27**,** 826-835.

LI, S., HAO, X., DAI, X. & TAO, T. 2018b. Rapid Photocatalytic Degradation of Pollutant from Water under UV and Sunlight via Cellulose Nanofiber Aerogel Wrapped by TiO2. *Journal of Nanomaterials,* 2018**,** 1-12.

LI, X., WU, D., LUO, Q., YIN, R., AN, J., LIU, S. & WANG, D. 2017a. Fabrication of CPAN/Ag/AgCl composites and their efficient visible-light photocatalytic activity. *Journal of Alloys and Compounds,* 702**,** 585-593.

LI, X., ZHU, C., SONG, Y., DU, D. & LIN, Y. 2017b. Solvent co-mediated synthesis of ultrathin BiOCl nanosheets with highly efficient visible-light photocatalytic activity. *RSC Advances,* 7**,** 10235-10241.

LI, Y., SUN, S., MA, M., OUYANG, Y. & YAN, W. 2008. Kinetic study and model of the photocatalytic degradation of rhodamine B (RhB) by a TiO2-coated activated carbon catalyst: Effects of initial RhB content, light intensity and TiO2 content in the catalyst. *Chemical Engineering Journal,* 142**,** 147-155.

LIN, D., XIAO, M., ZHAO, J., LI, Z., XING, B., LI, X., KONG, M., LI, L., ZHANG, Q., LIU, Y., CHEN, H., QIN, W., WU, H. & CHEN, S. 2016. An Overview of Plant Phenolic Compounds and Their Importance in Human Nutrition and Management of Type 2 Diabetes. *Molecules,* 21.

LING, C. M., MOHAMED, A. R. & BHATIA, S. 2004. Performance of photocatalytic reactors using immobilized TiO2 film for the degradation of phenol and methylene blue dye present in water stream. *Chemosphere,* 57**,** 547-54.

LIN, W., YU, X., ZHU, Y. & ZHANG, Y. 2018. Graphene Oxide/BiOCl Nanocomposite Films as Efficient Visible Light Photocatalysts. *Front Chem,* 6**,** 274.

LIU, Y., XU, J., WANG, L., ZHANG, H., XU, P., DUAN, X., SUN, H. & WANG, S. 2017. Three-Dimensional BiOI/BiOX (X = Cl or Br) Nanohybrids for Enhanced Visible-Light Photocatalytic Activity. *Nanomaterials (Basel),* 7.

LIU, Y., ZHU, Y., XU, J., BAI, X., ZONG, R. & ZHU, Y. 2013. Degradation and mineralization mechanism of phenol by BiPO4 photocatalysis assisted with H2O2. *Applied Catalysis B: Environmental,* 142-143**,** 561-567.

LOU, S., WANG, W., WANG, L. & ZHOU, S. 2019. In-situ oxidation synthesis of Cu2O/Ag/AgCl microcubes with enhanced visible-light photocatalytic activity. *Journal of Alloys and Compounds,* 781**,** 508-514.

MA, D., ZHONG, J., LI, J., WANG, L. & PENG, R. 2018. Enhanced photocatalytic activity of BiOCl by C70 modification and mechanism insight. *Applied Surface Science,* 443**,** 497-505.

MAHLAMBI, M. M., NGILA, C. J. & MAMBA, B. B. 2015. Recent Developments in Environmental Photocatalytic Degradation of Organic Pollutants: The Case of Titanium Dioxide Nanoparticles—A Review. *Journal of Nanomaterials,* 2015**,** 1-29.

MAKGATO S.S., CHIRWA E.M.N. (2015). Photoassisted biodegradation of irradiated organics in simulated nuclear wastewater. *Water Environment Research*, 87 (5), 392-403.

MANASSERO, A., SATUF, M. L. & ALFANO, O. M. 2013. Evaluation of UV and visible light activity of TiO2 catalysts for water remediation. *Chemical Engineering Journal,* 225**,** 378-386.

MANGRULKAR, P. A., KAMBLE, S. P., JOSHI, M. M., MESHRAM, J. S., LABHSETWAR, N. K. & RAYALU, S. S. 2012. Photocatalytic Degradation of Phenolics by N-Doped Mesoporous Titania under Solar Radiation. *International Journal of Photoenergy,* 2012**,** 1-10.

MCCULLAGH, C., SKILLEN, N., ADAMS, M. & ROBERTSON, P. K. J. 2011. Photocatalytic reactors for environmental remediation: a review. *Journal of Chemical Technology & Biotechnology,* 86**,** 1002-1017.

MENG, X. & ZHANG, Z. 2016. Ag/AgCl Loaded Bi2WO6Composite: A Plasmonic Z-Scheme Visible Light-Responsive Photocatalyst. *International Journal of Photoenergy,* 2016**,** 1-11.

MIRANDA-GARCÍA, N., SUÁREZ, S., MALDONADO, M. I., MALATO, S. & SÁNCHEZ, B. 2014. Regeneration approaches for TiO2 immobilized photocatalyst used in the elimination of emerging contaminants in water. *Catalysis Today,* 230**,** 27-34.

MOHAMMED, A. A. 2007. Electrocoagulation of phenol for wastewater treatment. *Iraqi Journal of Chemical and Petroleum Engineering* 9(3)**,** 37-41.

MUKHERJEE, P. S. & RAY, A. K. 1999. Major Challenges in the Design of a Large-Scale Photocatalytic Reactor for Water Treatment. *Chemical Engineering & Technology,* 22**,** 253-260.

MYTYCH, P. & STASICKA, Z. 2004. Photochemical reduction of chromium(VI) by phenol and its halogen derivatives. *Applied Catalysis B-Environmental,* 52**,** 167-172.

NADDEO V.,CESARO A.,MANTZAVINOS D., FATTA-KASSINOS D. & BELGIORNO V. 2014. Water and Wastewater Disinfection by Ultrasound Irradiation – A Critical Review. *Global NEST Journal,*16,3,561-577.

NGUYEN, C. H., FU, C.-C. & JUANG, R.-S. 2018. Degradation of methylene blue and methyl orange by palladium-doped TiO2 photocatalysis for water reuse: Efficiency and degradation pathways. *Journal of Cleaner Production,* 202**,** 413-427.

NIU, H., WANG, Q., LIANG, H., CHEN, M., MAO, C., SONG, J., ZHANG, S., GAO, Y. & CHEN, C. 2014. Visible-Light Active and Magnetically Recyclable Nanocomposites for the Degradation of Organic Dye. *Materials (Basel),* 7**,** 4034-4044.

O'SHEA, K. E. & DIONYSIOU, D. D. 2012. Advanced oxidation processes for water treatment. ACS Publications.

RAN, Z., WANG, X., LI, Y., YANG, D., ZHAO, X.-G., BISWAS, K., SINGH, D. J. & ZHANG, L. 2018. Bismuth and antimony-based oxyhalides and chalcohalides as potential optoelectronic materials. *npj Computational Materials,* 4.

RAY, A. K. & BEENACKERS, A. A. 1998. Novel Photocatalytic reactor for water purification. *AIChE Journal,* 44**,** 477-483.

RIBEIRO, A. R., NUNES, O. C., PEREIRA, M. F. & SILVA, A. M. 2015. An overview on the advanced oxidation processes applied for the treatment of water pollutants defined in the recently launched Directive 2013/39/EU. *Environ Int,* 75**,** 33-51.

SARWAN, B., PARE, B., ACHARYA, A. D. & JONNALAGADDA, S. B. 2012. Mineralization and toxicity reduction of textile dye neutral red in aqueous phase using BiOCl photocatalysis. *J Photochem Photobiol B,* 116**,** 48-55.

SHEKHAR, S., SOOD, S., SHOWKAT, S., LITE, C., CHANDRASEKHAR, A., VAIRAMANI, M., BARATHI, S. & SANTOSH, W. 2017. Detection of phenolic endocrine disrupting chemicals (EDCs) from maternal blood plasma and amniotic fluid in Indian population. *Gen Comp Endocrinol,* 241**,** 100-107.

SING, K. & WILLIAMS, R. 2004. Physisorption Hysteresis loops and the characterisation of nanoporous materials. *Adsoprtion Science and Technology,* 22**,** 773-782.

SINGH, P., SONU, RAIZADA, P., SUDHAIK, A., SHANDILYA, P., THAKUR, P., AGARWAL, S. & GUPTA, V. K. 2018. Enhanced photocatalytic activity and stability of AgBr/BiOBr/graphene heterojunction for phenol degradation under visible light. *Journal of Saudi Chemical Society*.

SRIKANTH, B., GOUTHAM, R., NARAYAN R.B., RAMPRASATH, A. & SANKARANARAYANAN, A.R. 2017. Recent advancements in supporting materials for immobilised photocatalytic applications in waste water treatment. *Journal of Environmental Management,* 200, 60-78.

SUN, D., LI, J., FENG, Z., HE, L., ZHAO, B., WANG, T., LI, R., YIN, S. & SATO, T. 2014. Solvothermal synthesis of BiOCl flower-like hierarchical structures with high photocatalytic activity. *Catalysis Communications,* 51**,** 1-4.

TERASAKA, S., INOUE, A., TANJI, M. & KIYAMA, R. 2006. Expression profiling of estrogen-responsive genes in breast cancer cells treated with alkylphenols, chlorinated phenols, parabens, or bis- and benzoylphenols for evaluation of estrogenic activity. *Toxicol Lett,* 163**,** 130-41.

TIEN, L.-C., LIN, Y.-L. & CHEN, S.-Y. 2013. Synthesis and characterization of Bi12O17Cl2 nanowires obtained by chlorination of α-Bi2O3 nanowires. *Materials Letters,* 113**,** 30-33.

VAN GERVEN, T., MUL, G., MOULIJN, J. & STANKIEWICZ, A. 2007. A review of intensification of photocatalytic processes. *Chemical Engineering and Processing: Process Intensification,* 46**,** 781-789.

WAHAB, H. S. & HUSSAIN, A. A. 2016. Photocatalytic oxidation of phenol red onto nanocrystalline TiO2 particles. *Journal of Nanostructure in Chemistry,* 6**,** 261-274.

WANG, J. L. & XU, L. J. 2012. Advanced Oxidation Processes for Wastewater Treatment: Formation of Hydroxyl Radical and Application. *Critical Reviews in Environmental Science and Technology,* 42**,** 251-325.

WANG, L., SHI, Y., WANG, T. & ZHANG, L. 2017. Silver chloride enwrapped silver grafted on nitrogen-doped reduced graphene oxide as a highly efficient visible-light-driven photocatalyst. *J Colloid Interface Sci,* 505**,** 421-429.

WANG, P., HUANG, B., QIN, X., ZHANG, X., DAI, Y., WEI, J. & WHANGBO, M. H. 2008. Ag@AgCl: a highly efficient and stable photocatalyst active under visible light. *Angew Chem Int Ed Engl,* 47**,** 7931-3.

WANG, Q., HUI, J., HUANG, Y., DING, Y., CAI, Y., YIN, S., LI, Z. & SU, B. 2014. The preparation of BiOCl photocatalyst and its performance of photodegradation on dyes. *Materials Science in Semiconductor Processing,* 17**,** 87-93.

WANG, X., YAO, Z., WANG, J., GUO, W. & LI, G. 2008. Degradation of reactive brilliant red in aqueous solution by ultrasonic cavitation. *Ultrason Sonochem,* 15**,** 43-8.

WANG, Y., SUZUKI, H., XIE, J., TOMITA, O., MARTIN, D. J., HIGASHI, M., KONG, D., ABE, R. & TANG, J. 2018. Mimicking Natural Photosynthesis: Solar to Renewable H2 Fuel Synthesis by Z-Scheme Water Splitting Systems. *Chem Rev,* 118**,** 5201-5241.

WEI, D., TIAN, F., LU, Z., YANG, H. & CHEN, R. 2016. Facile synthesis of Ag/AgCl/BiOCl ternary nanocomposites for photocatalytic inactivation of S. aureus under visible light. *RSC Advances,* 6**,** 52264-52270.

WEI, C., ZHANG, F., HU, Y., FENG, C. & WU, H. 2017. Ozonation in water treatment: the generation, basic properties of ozone and its practical application. *Reviews in Chemical Engineering,* 33.

WEN, X.-J., NIU, C.-G., ZHANG, L., HUANG, D.-W. & ZENG, G.-M. 2017. In-situ synthesis of visible-light-driven plasmonic Ag/AgCl-CdWO4 photocatalyst. *Ceramics International,* 43**,** 1922-1929.

XIA, L., JIANG, X., CHENG, Z., LIAO, Y., WANG, Z., PU, Q. & DUAN, M. 2018. Synthesis of Pp-16@Ag/AgCl of high performance photocatalyst particles for decomposition of Rhodamine B and fast green dyes. *Materials Chemistry and Physics,* 218**,** 98-107.

XIAO, S., WAN, D., ZHANG, K., QU, H. & PENG, J. 2016. Enhanced photoelectrocatalytic degradation of ammonia by in situ photoelectrogenerated active chlorine on TiO2 nanotube electrodes. *J Environ Sci (China),* 50**,** 103-108.

XIE, J., CAO, Y., JIA, D., LI, Y., WANG, K. & XU, H. 2017. In situ solid-state fabrication of hybrid AgCl/AgI/AgIO3 with improved UV-to-visible photocatalytic performance. *Sci Rep,* 7**,** 12365.

XIONG, J., CHENG, G., QIN, F., WANG, R., SUN, H. & CHEN, R. 2013. Tunable BiOCl hierarchical nanostructures for high-efficient photocatalysis under visible light irradiation. *Chemical Engineering Journal,* 220**,** 228-236.

XU, Q., ZHANG, L., YU, J., WAGEH, S., AL-GHAMDI, A. A. & JARONIEC, M. 2018a. Direct Z-scheme photocatalysts: Principles, synthesis, and applications. *Materials Today,* 21**,** 1042-1063.

XU, W., ZHANG, Y. & CHEN, T. 2019. Single particle nanocatalysis : fundamentals and applications. Changchun: Wiley-VCH.

XU, Y., LIN, D., LIU, X., LUO, Y., XUE, H., HUANG, B., QIAN, Q. & CHEN, Q. 2018b. TiO 2 hollow nanofibers grafted Ag/AgCl with more AgCl {1 1 1} facet for enhanced photocatalytic activity. *Materials Letters,* 215**,** 250-253.

XU, Y., XU, S., WANG, S., ZHANG, Y. & LI, G. 2014. Citric acid modulated electrochemical synthesis and photocatalytic behavior of BiOCl nanoplates with exposed {001} facets. *Dalton Trans,* 43**,** 479-85.

YANG, J., XIE, T., LIU, C. & XU, L. 2018. Dy(III) Doped BiOCl Powder with Superior Highly Visible-Light-Driven Photocatalytic Activity for Rhodamine B Photodegradation. *Nanomaterials (Basel),* 8.

YE, L., LIU, J., GONG, C., TIAN, L., PENG, T. & ZAN, L. 2012. Two Different Roles of Metallic Ag on Ag/AgX/BiOX (X = Cl, Br) Visible Light Photocatalysts: Surface Plasmon Resonance and Z-Scheme Bridge. *ACS Catalysis,* 2**,** 1677-1683.

YE, L., SU, Y., JIN, X., XIE, H. & ZHANG, C. 2014. Recent advances in BiOX (X = Cl, Br and I) photocatalysts: synthesis, modification, facet effects and mechanisms. *Environmental Science: Nano,* 1.

ZHANG, L., DING, N., LOU, L., IWASAKI, K., WU, H., LUO, Y., LI, D., NAKATA, K., FUJISHIMA, A. & MENG, Q. 2019. Localized Surface Plasmon Resonance Enhanced Photocatalytic Hydrogen Evolution via Pt@Au NRs/C3 N4 Nanotubes under Visible-Light Irradiation. *Advanced Functional Materials,* 29.

ZHANG, L. S., LONG, T. F., YAN, C. Q., HE, X. C., CHENG, M. L. & ZHONG, S. 2013. Synthesis of AgCl/BiOCl Composite Photocatalyst and its Photocatalytic Activity under Visible-Light Irradiation. *Advanced Materials Research,* 662**,** 372-378.

ZHANG, W., DONG, X. A., JIA, B., ZHONG, J., SUN, Y. & DONG, F. 2018. 2D BiOCl/Bi 12 O 17 Cl 2 nanojunction: Enhanced visible light photocatalytic NO removal and in situ DRIFTS investigation. *Applied Surface Science,* 430**,** 571-577.

ZHANG, X., AI, Z., JIA, F. & ZHANG, L. 2008. Generalized One-Pot Synthesis, Characterization, and Photocatalytic Activity of Hierarchical BiOX (X = Cl, Br, I) Nanoplate Microspheres. *The Journal of Physical Chemistry C,* 112**,** 747-753.

ZHANG, X. F., LIU, Z. G., SHEN, W. & GURUNATHAN, S. 2016. Silver Nanoparticles: Synthesis, Characterization, Properties, Applications, and Therapeutic Approaches. *Int J Mol Sci,* 17.

ZHAO, M., ZHOU, W., LU, M., GUO, Z., LI, C. & WANG, W. 2019. Novel AgCl nanotubes/BiOCl nanosheets composite with improved adsorption capacity and photocatalytic performance. *Journal of Alloys and Compounds,* 773**,** 1146-1153.

ZHAO, Q., XING, Y., LIU, Z., OUYANG, J. & DU, C. 2018a. Synthesis and Characterization of Modified BiOCl and Their Application in Adsorption of Low-Concentration Dyes from Aqueous Solution. *Nanoscale Research Letters,* 13.

ZHAO, S., ZHANG, Y., ZHOU, Y., QIU, K., ZHANG, C., FANG, J. & SHENG, X. 2018b. Reactable polyelectrolyte-assisted preparation of flower-like Ag/AgCl/BiOCl composite with enhanced photocatalytic activity. *Journal of Photochemistry and Photobiology A: Chemistry,* 350**,** 94-102.

ZHOU, P., YU, J. & JARONIEC, M. 2014. All-solid-state Z-scheme photocatalytic systems. *Adv Mater,* 26**,** 4920-35.

ZHU, S. & WANG, D. 2017. Photocatalysis: Basic Principles, Diverse Forms of Implementations and Emerging Scientific Opportunities. *Advanced Energy Materials,* 7.

APPENDICES

Appendix A: Characterisations

TEM

Morphology and geometrical structure of BiOCl and Ag/AgCl/BiOCl were observed and shown in Figure A 1. The BiOCl TEM image confirms the sphere like structures consisting of thin plates. The Ag/AgCl/BiOCl TEM image also shows sphere-like flowers closely assembled.

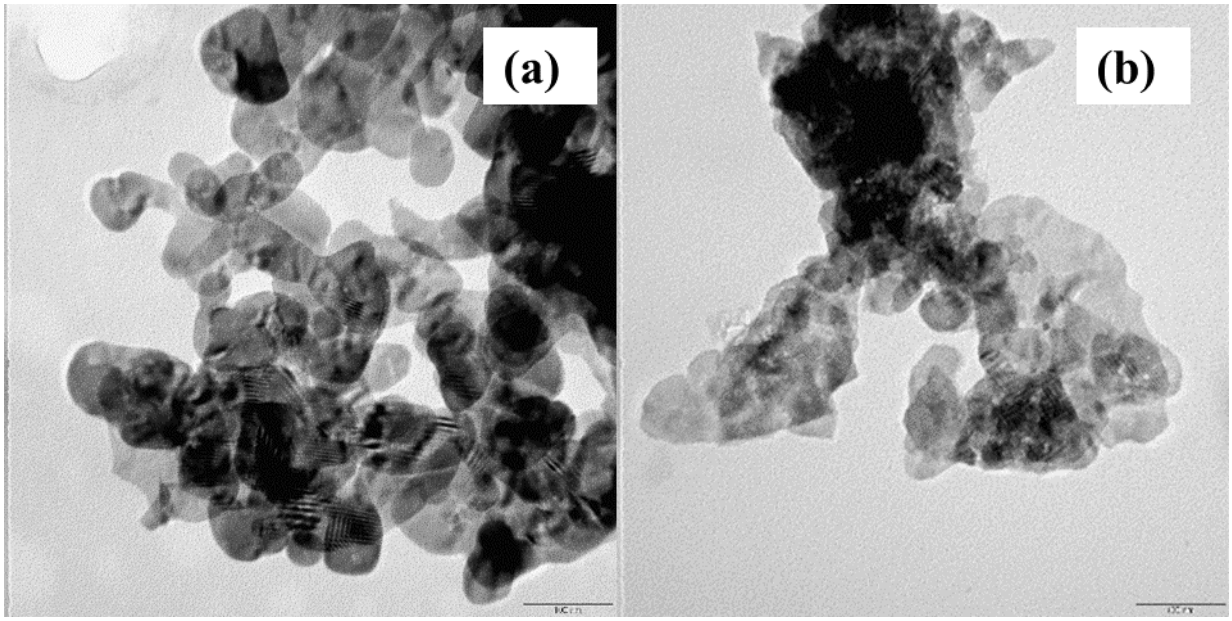

Figure A 1: TEM image of (a) BiOCl and (b) Ag/AgCl/BiOCl

SEM-EDS Elemental Mapping

AgCl

Figure A *2* shows the elemental mapping for AgCl which illustrates uniform distribution of Ag and Cl in the selected area.

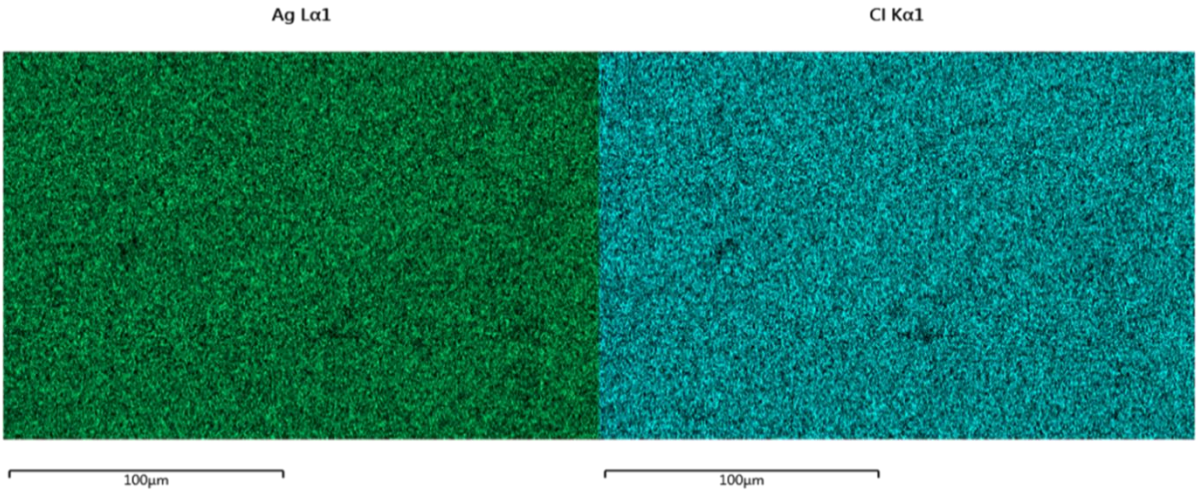

Figure A 2: AgCl elemental mapping

BiOCl

Figure A 3 shows the elemental mapping for BiOCl which illustrates uniform distribution of Bi, O and Cl in the selected area.

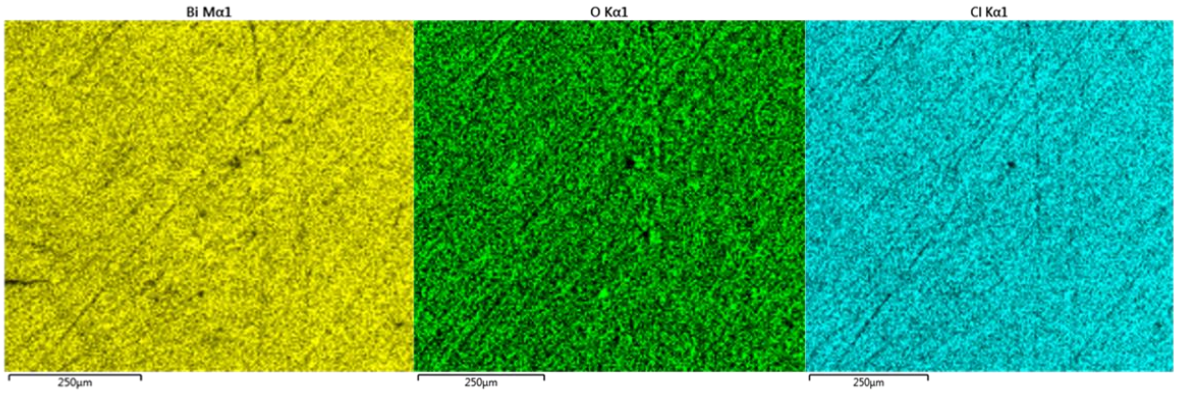

Figure A 3: BiOCl elemental mapping

AgCl/BiOCl

Figure A *4* shows the elemental mapping for AgCl/BiOCl which illustrates uniform distribution of Ag, Cl, Bi and O in the selected area.

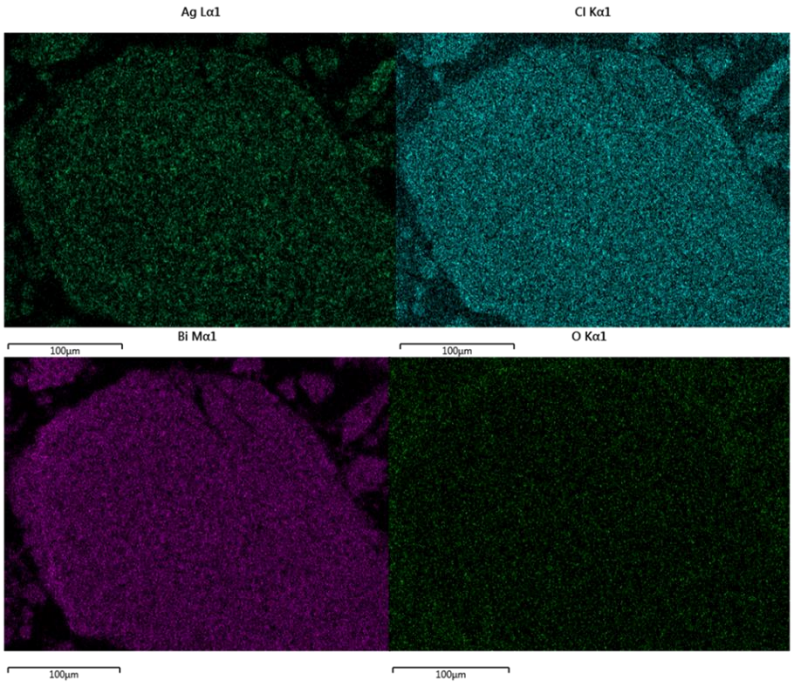

Figure A 4: AgCl/BiOCl elemental mapping

Ag/AgCl/BiOCl

Figure A 5 shows the elemental mapping for Ag/AgCl/BiOCl which illustrates uniform distribution of Ag, Bi, O and Cl in the selected area.

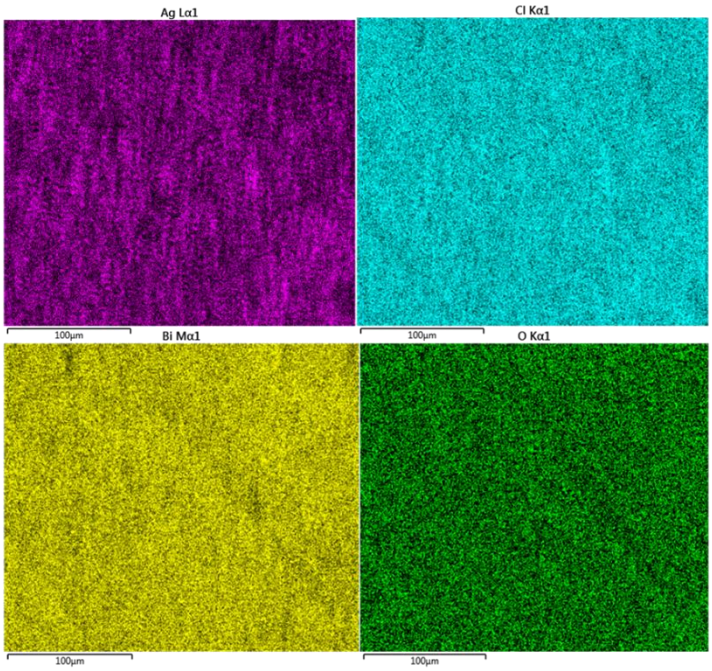

Figure A 5: Ag/AgCl/BiOCl elemental mapping

Appendix B: HPLC method development

Phenol was calibrated on the HPLC by preparing phenol standards of 2 ppm, 4 ppm, 6 ppm and 10 ppm solutions. The calibration curve is shown in Figure B1 with R^2 value of 0.999968.

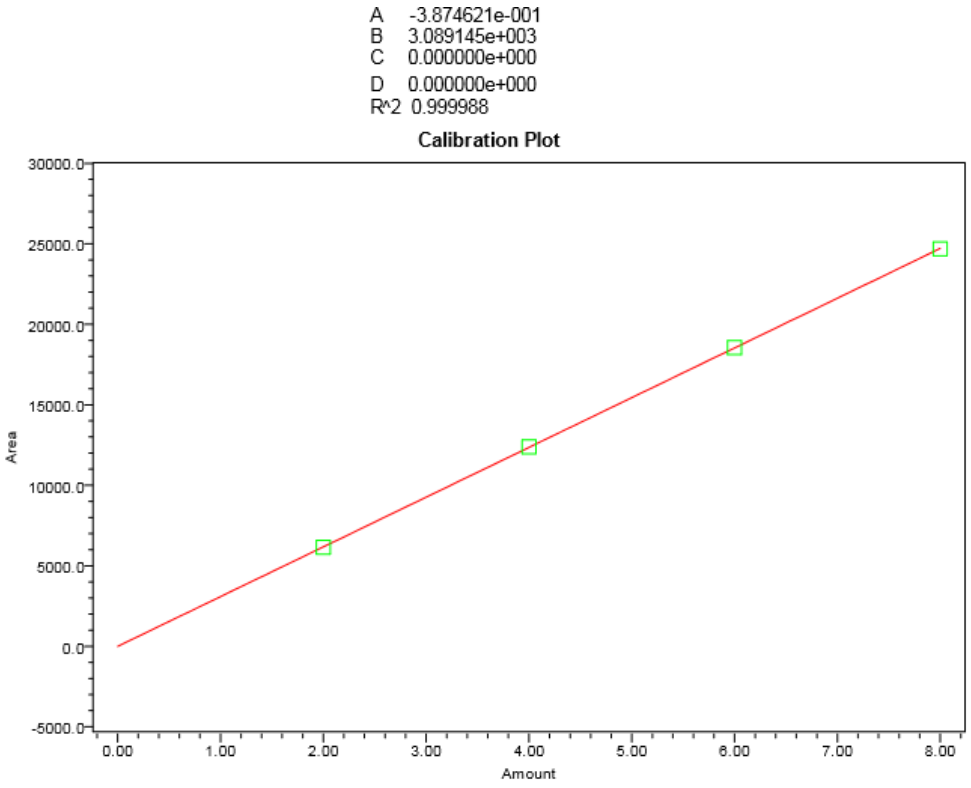

Peak: PHENOL

	Name	Level	X Value	Response	Calc. Value	% Deviation	Manual	Ignore
1	PHENOL	Level 1	2.000000	6152.152907	1.991665	-0.417	No	No
2	PHENOL	Level 2	4.000000	12388.563134	4.010479	0.262	No	No
3	PHENOL	Level 3	6.000000	18546.986579	6.004048	0.067	No	No
4	PHENOL	Level 4	8.000000	24693.643873	7.993808	-0.077	No	No

Figure B 1: Phenol HPLC calibration curve